SOLID-OXIDE FUEL CELLS FOR UNCONVENTIONAL OIL AND GAS PRODUCTION

by

Gladys A. Anyenya

A thesis submitted to the Faculty and the Board of Trustees of the Colorado School of Mines in partial fulfillment of the requirements for the degree of Doctor of Philosophy (Mechanical Engineering).

Golden, Colorado

Date _____

Signed: _____
Gladys A. Anyenya

Signed: _____
Dr. Neal P. Sullivan
Thesis Advisor

Signed: _____
Dr. Alexandra Newman
Thesis Advisor

Golden, Colorado

Date _____

Signed: _____
Dr. Gregory Jackson
Professor and Head
Department of Mechanical Engineering

ABSTRACT

This dissertation presents a novel, **cost − effective, environmentally sustainable** method for converting United States' vast oil shale reserves into crude oil. Geothermic Fuel Cells (GFC) are designed for in-situ oil-shale processing. When implemented, the GFC is placed underground within an oil-shale formation; the heat released by the high-temperature solid oxide fuel cells within the GFC during electricity generation is used to upgrade oil shale into sweet crude oil. The world's first Geothermic Fuel Cell prototypes were designed and built by Delphi Powertrain Systems; their performance was characterized at the Colorado Fuel Cell Center (Golden, CO, USA). Following indoor, laboratory operation and validation of two GFC modules, three multi-stack modules were assembled into a nine-stack GFC that was integrated with a natural gas fuel processor and ancillary components, and operated underground within the geology at the Colorado School of Mines campus.

Extensive experimental data collected during GFC testing was used to calibrate a steady-state system model in Aspen Plus^{TM} to predict the GFC stacks' electrochemical performance and the heat-rejection from the module. Following model validation, further simulations are performed for different values of current, fuel and air utilization to study their influence on system electrical and heating performance. The model is used to explore a wider range of operating conditions than can be experimentally tested, and provides insight into competing physical processes during Geothermic Fuel Cell operation. Results show that the operating conditions can be tuned to generate desired heat-flux conditions as needed across applications. A maximum combined-heat-and-power-efficiency of 90% is recorded in the parametric study. Using simulation data from the GFC model, a continuous, non-convex nonlinear multi-objective optimization model is developed in AMPL to optimize the design and dispatch of a single GFC heater well. The optimization model seeks to maximize the system heating and electrical efficiencies while minimizing costs. The optimal design and dispatch

strategy obtained using the KNITRO 12.2.0 solver yielded a well-head cost of 37 $/bbl for the oil and gas produced using the GFC technology and a maximum combined-heat-and-power-efficiency of 79%.

TABLE OF CONTENTS

LIST OF FIGURES

LIST OF TABLES

LIST OF ABBREVIATIONS

Precision Combustion Inc.	PCI
Autothermal Reforming	ATR
Steam Reforming	SR
Partial Oxidation	POX
Lower Heating Value (kJ kg^{-1})	LHV
Open Circuit Voltage (V)	OCV
Area Specific Resistance (Ω cm^2)	ASR
Heat Exchanger	HX
Steam-to-Carbon ratio	S/C
Standard Liters Per Minute	SLPM
Barrel of Oil Equivalent	BOE
Independent Energy Partners	IEP
Colorado School of Mines	CSM
Colorado Fuel Cell Center	CFCC
Geothermic Fuel Cell	GFC
The Oil Shale Corporation	TOSCO
Institute of Gas Technology	IGT
Combined Heat and Power	CHP
A Mathematical Programming Language	AMPL
In Situ Conversion Process	ICP

Conduction, Convection, Reflux . . . . . CCR

Solid Oxide Fuel Cell . . . . . SOFC

Gas Turbine . . . . . GT

Liquefied Petroleum Gas . . . . . LPG

Natural Gas . . . . . NG

Oxygen-to-Carbon ratio . . . . . O/C

LIST OF SYMBOLS

Nernst potential (V) . . . . . E_n

Standard electrode potential (V) . . . . . E^0

Fraday's constant (C mol^{-1}) . . . . . F

Stack electric current (A) . . . . . I_{stack}

current density (A cm^{-2}) i

Number of electrons per mol (-) . . . . . n

Number of fuel cells per stack (-) . . . . . N_{cells}

Molar flow rate (mol s^{-1}) . . . . . $\dot{n}$

Stack pressure (kpa) . . . . . P_{stack}

DC power generated by the stack (W) . . . . . P_{elec}

Universal gas constant (J mol^{-1} K^{-1}) . . . . . $\overline{R}$

Stack cassette temperature (K) . . . . . T_{stack}

Fuel utilization (-) . . . . . U_F

Cell voltage (V) . . . . . V_{cell}

Stack voltage (V) . . . . . V_{stack}

exchange current density (A cm^{-2}) . . . . . i_o

limiting current densities (A cm^{-2}) . . . . . i_L

molar enthalpy of each species j (kJ $kmol^{-1}$) . . . . . $\overline{h}_j$

pre-exponential term (A cm^{-2}) . . . . . P_o

activation energy (J mol^{-1}) . . . . . E_{act}

charge-transfer resistance (Ω cm^2) . . . . . $\mathbb{R}$

partial pressures (kPa) . . . . . P_L

binary diffusion coefficients (m^2 s^{-1}) . . . . . D_L

heat transfer coefficients (W m^{-2} K^{-1}) . . . . . $\overline{h}$

Nusselt number (-) . . . . . $\overline{\mathrm{Nu}}$

thermal conductivity of air (W m^{-1} K^{-1}) . . . . . k_{air}

component surface area (m^2) . . . . . A

heat transfer to geology (W) . . . . . $\dot{Q}_{\mathrm{geo}}$

heat convected out via exhaust gas (kW) . . . . . $\dot{Q}_{\mathrm{gas}}$

heat flux to geology (kW m^{-1}) . . . . . $\dot{Q}_{\mathrm{loss}}$

equivalent heat transfer resistance (K W^{-1}) . . . . . R_{total}

total flow of energy in air inlet (kW) . . . . . $\dot{E}_{\mathrm{air}}$

total flow of energy in fuel inlet (kW) . . . . . $\dot{E}_{\mathrm{fuel}}$

total flow of energy in annulus exhaust (kW) . . . . . $\dot{E}_{\mathrm{ann}}$

chemical energy flow in stream (kW) . . . . . $\dot{E}_{\mathrm{chem}}$

sensible energy flow in stream (kW) . . . . . $\dot{E}_{\mathrm{sens}}$

GFC module electric power output (kW) . . . . . $\dot{W}_{\mathrm{elec}}$

ohmic polarization (V) . . . . . η_{ohm}

activation polarization (V) . . . . . η_{act}

anode concentration polarization (V) . . . . . $\eta_{\mathrm{conc,a}}$

cathode concentration polarization (V) . . . . . $\eta_{\mathrm{conc,c}}$

leakage coefficient (-) . . . . . θ

symmetry factor (-) . . . . . α

component conductivities (S cm^{-1}) . . . . . σ_L

component emissivities (-) . . . . . ε

Stefan-Boltzmann constant (W m^{-2} K^{-4}) . . . . . σ

electrical efficiency (%) . . . . . $\mathcal{E}_{\text{elec}}$

heating efficiency (%) . . . . . $\mathcal{E}_{\text{heat}}$

combined heat and power efficiency (%) . . . . . $\mathcal{E}_{\text{CHP}}$

empirical fraction of net heat flux (-) . . . . . β

ACKNOWLEDGMENTS

I would like to begin by thanking all the people who contributed in some way to the work described in this dissertation. My sincere gratitude to my advisors Prof. Neal Sullivan, Prof. Robert Braun and Prof. Alexandra Newman for their patience, motivation, enthusiasm, and immense knowledge in support of my Ph.D study and research. I would like to thank the rest of my committee: Prof. Gregory Jackson and Prof. Peter Maniloff for their encouragement, insightful comments, and hard questions. I would like to show my gratitude to our industry partners (IEP) and Jahi Simbai for providing funding for this work. I would also like to acknowledge my colleagues at the Colorado Fuel Cell Center and the CSM ME Thermal Sciences division for their comradery and assistance that proved to be a milestone in the accomplishment of my end goal. Last but not least, I would like to thank my friends and family for their patience, love and support over the years. GRATIAS DOMINO BONORUM OMNIUM!

This dissertation is dedicated to my parents Ruth Oyugi and Vitalis Anyenya for the inspiration, drive, and support that you have given me to make me the person I am today.

CHAPTER 1
INTRODUCTION

IEP Technologies Inc., Delphi Powertrain Systems, and the Colorado School of Mines (CSM) have partnered to develop the world's first Geothermic Fuel Cells (GFCs). In the Geothermic Fuel Cell concept, the heat that is generated by high-temperature solid-oxide fuel cells is harnessed and utilized for the liberation of oil and gas from oil shale (Figure 1.1). When deployed, a network of Geothermic Fuel Cells is placed within oil-shale formations hundreds of meters below the earth's surface. The heat released during GFC operation is harnessed to heat oil shale to the temperatures required for conversion of kerogen fuel trapped within the shale into liquid oil. Once formed, the oil is withdrawn from the formation using collector wells. The electricity generated during GFC operation can be used to serve plant processes at the surface [1]. The GFC system requires higher heating demands, resulting in lower electrical efficiencies and higher thermal efficiencies [2, 3]. This new combined heat and power application of SOFC technology in unconventional oil and gas processing presents a potentially transformative technology for accessing the world's vast oil shale reserves, estimated at 4.8 trillion barrels worldwide, while offering a large, high-volume market opportunity for SOFCs.

The first complete GFC prototype, designed and built by Delphi Automotive, LLC. (Fenton, MI, USA) for IEP Technology, Inc. (Parker, CO, USA), is comprised of three 1.5-kW_e SOFC stack-and-combustor units packaged within a stainless-steel casing (Figure 3.1). The stacks are placed in a 0.3-m-diameter cylindrical housing for ease of installation within a circular bore hole drilled into the geological formation. The stacks are vertically distributed within the 1.8-m-tall housing to promote uniform surface temperatures and heat rejection. Reactive gases feed the three stacks in a parallel configuration. A portion of these reactants is electrochemically converted to electricity and products within the SOFC stacks. Anode

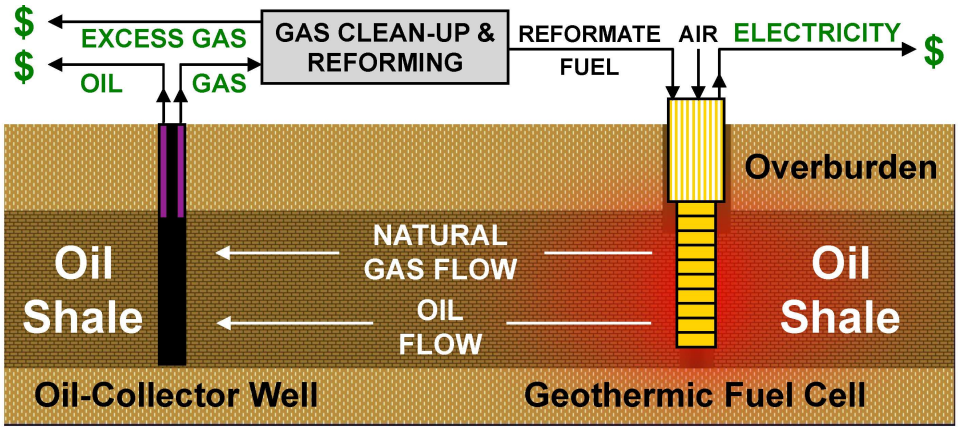

Figure 1.1: Illustration of the Geothermic Fuel Cell concept, solid-oxide fuel cells provide the thermal energy to heat the formation.

exhaust gases can vent to the atmosphere through anode-return plumbing (not shown) or mix with cathode exhaust and burn within combustors located below stacks. These hot exhaust gases from the combustors are then directed upwards through the annular space between the two stainless steel housings, rejecting heat to the surroundings before being exhausted above ground.

This dissertation describes a series of physical and computational experiments regarding the Geothermic Fuel Cell modules and its effectiveness for providing combined heat and power for unconventional oil and gas recovery.

1.1 Background Information on Oil Shale Processing

The U.S. Geological survey estimates that over four trillion barrels of oil are trapped in the Piceance Basin of northwestern Colorado, the Uinta Basin of northeastern Utah and the Greater Green River Basin of southwestern Wyoming [4, 5]. Total resources of a selected group of oil shale deposits in 33 countries are estimated at 409 billion tons of in-situ shale oil [6]. At this time, no cost-effective and environmentally sustainable method for accessing these vast oil reserves exists. In contrast to liquid shale oil (or "tight oil") trapped within porous geology [7], oil shale is a sedimentary rock that contains organic matter called kerogen [8]. When pyrolysed to approximately 350 °C [9], this kerogen decomposes into a mixture of

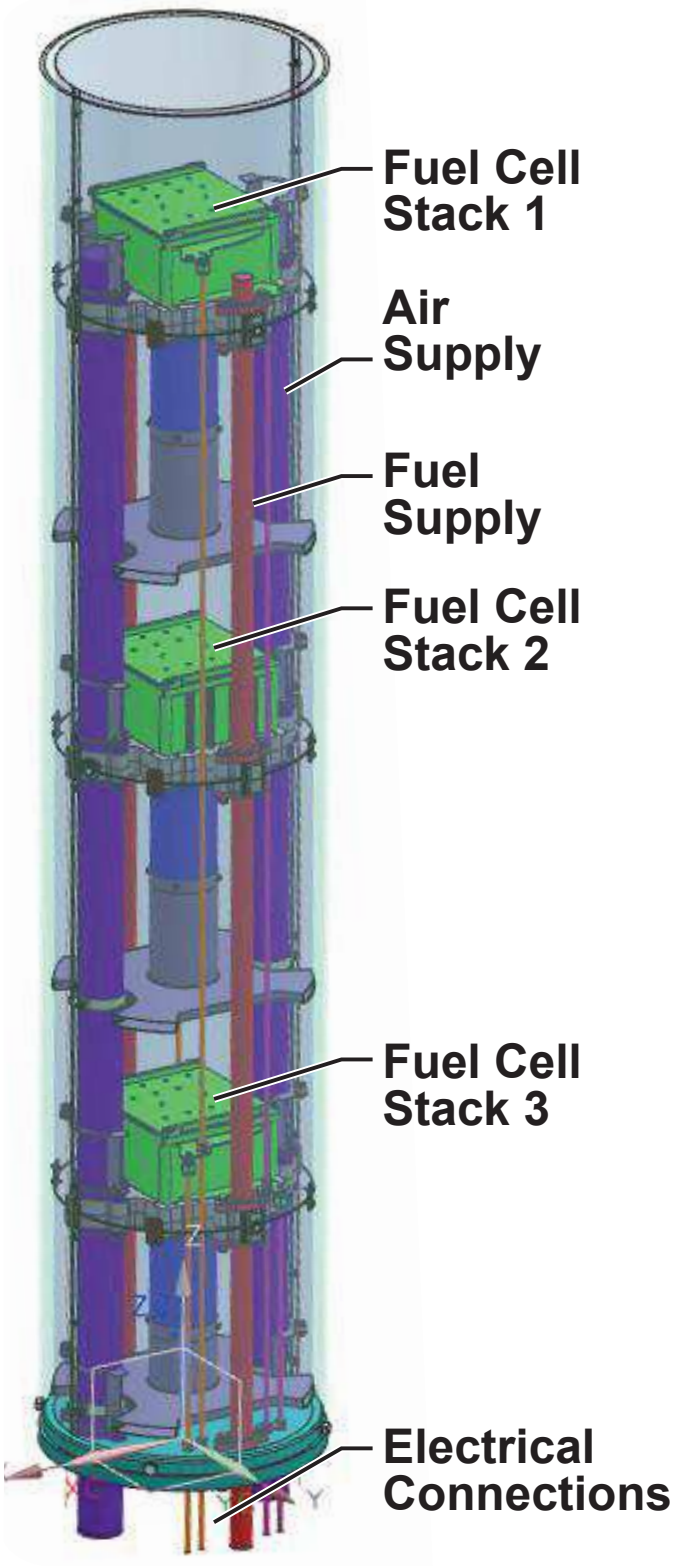

Figure 1.2: Delphi's design concept for the 3-stack Geothermic Fuel Cell assembly.

oil, hydrocarbon gas and carbon-rich shale coke [10]. These oil-rich kerogen beds are buried below 250-600 m (800-1900 ft) of overburden, and can extend over 900 m (3,000 ft) below the surface at the center of the basins. This study focuses on a novel in-situ oil shale processing method that utilizes the Combined Heat and Power (CHP) capabilities of Solid Oxide Fuel Cells (SOFC) for the liberation of oil and gas from oil shale.

Traditionally, extraction of oil from oil shale has been via ex situ methods whereby the shale rock is mined from the earth then processed above ground. These processes lead to significant environmental impacts including surface disturbance, large water requirements, and waste management of char and other unwanted materials [11]. In situ oil shale processing techniques are being developed in which the formation is heated to retort the oil shale without mining. These methods help alleviate the adverse environmental impacts of ex situ processing [12]. Studies also show that in situ processing leads to a significant increase in the energy yield, as greater volumes of shale can be processed at a time [13].

Significant oil-shale retorts have been in operation for decades in Estonia, China, Brazil, and other sites. An estimated 930,000 metric tonnes (17,700 barrels per day) of shale oil was produced from these operations in 2008 [14]. Figure 1.3 shows data from several countries that processed oil shale between the years 1880–2000. World oil shale production peaked at 47 million tons in 1980 when most of it was mined in Estonia as fuel for several large electric power plants [6]. However, the cost of oil from unconventional oil-shale processing is not competitive when compared to oil from Middle East sources that average about $25–$30 per barrel.

1.1.1 Overview of Ex-situ Oil Shale Processing Methods

Internal combustion: The heat required to pyrolyze the oil shale is supplied by burning materials (typically char and oil shale gas) within a vertical shaft. Raw oil shale particles are fed into the top of the retort and are heated by the rising hot gases, which pass through the descending oil shale, thereby causing decomposition of the kerogen [14].

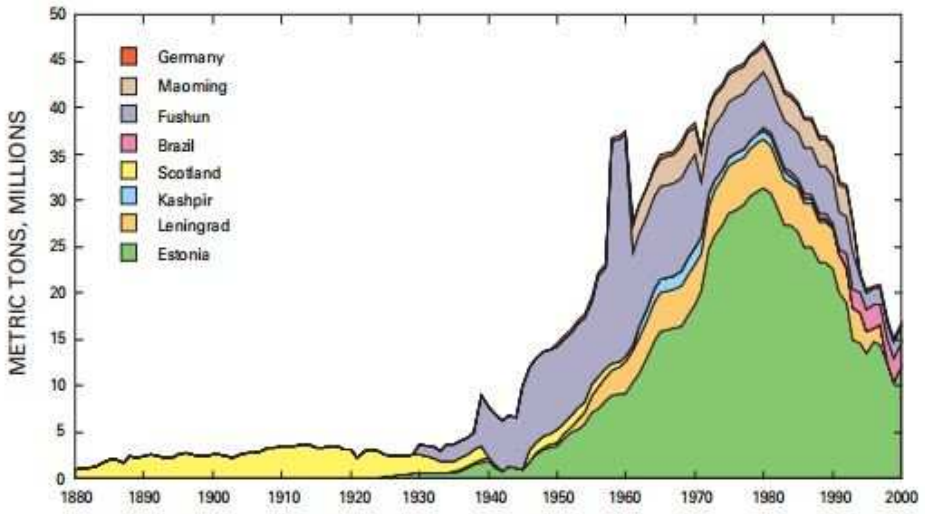

Figure 1.3: Production of oil shale in millions of metric tons from Estonia (Estonia deposit), Russia (Leningrad and Kashpir deposits), United Kingdom (Scotland, Lothians), Brazil (Irat Formation), China (Maoming and Fushun deposits), and Germany (Dotternhausen) from 1880 to 2000 [6].

Hot recycled solids: Heat is delivered to the oil shale by recycling hot solid particles (typically oil shale ash). The recycled particles are heated in a separate chamber and then mixed with the raw oil shale to cause the shale to decompose. The TOSCO II process uses ceramic balls instead of shale ash as the hot recycled solids [14].

Conduction through a wall: Heat is conducted through a retort wall to the oil shale. An example of this is the Combustion Resources Process whereby hot gas from a hydrogen-fired rotating kiln is circulated through an outer annulus [15]. The Red Leaf Resources EcoShale In-capsule Process combines surface mining with a lower-temperature heating method whereby the shale is partly mined then a hot gas is circulated through parallel pipes through the oil shale rubble [16].

Externally generated hot gas: The oil shale is heated by hot gases generated outside the retort vessel, thereby keeping the combustion exhaust and the retort vapors separate [14].

Reactive fluids: Extraction of oil from oil shale using reactive fluids has been tested [17]. The IGT Hytort process employs high pressure hydrogen as the donor solvent while the Chattanooga process uses a fluidized bed reactor and an associated hydrogen-fired heater for oil shale thermal cracking and hydrogenation [14].

1.1.2 Overview of In-situ Oil Shale Processing Methods

Conduction through a wall: Heat is supplied to the geology via heating elements or heating pipes placed within the oil shale formation. Shell Oil's "InSitu Conversion Process" (ICP) uses resistive heaters to supply heat to the shale. Each production well is surrounded by six heater wells forming a hexagonal pattern. To avoid groundwater contamination, coolants are circulated underground to form a freeze wall around the extraction zone [10]. This process was tested and 1700 barrels of shale oil was extracted at the Mahogany test site in the Piceance basin in 2004 [14]. The "Conduction, Convection, Reflux" process by American Shale Oil proposes flowing superheated steam through horizontal wells under the oil shale formation. The steam is expected to heat the oil shale from below, then rely on the hot shale to propagate the heat upwards to the rest of the formation through refluxing of the converted shale [11, 14].

Externally generated hot gas: This method involves injecting hot gases generated above-ground into the oil shale formation. Vertical wells are drilled to transport the gas to the oil shale formation where they are distributed throughout the geology via horizontal fractures. Mountain West Energy's "In-Situ Vapor Extraction Technology" uses high-temperature methane while Chevron's "CRUSH Process" uses heated carbon dioxide to heat the shale [14].

Volumetric heating: Illinois Institute of Technology's "Volumetric heating" method proposes the use of radio waves via electrode arrays to heat the formation [18]. Microwave

heating technology is also being studied as another option for volumetric oil shale processing, though it is believed that radio wave energy can penetrate much further into the formation. Electro-Petroleum proposes the application of joule resistive heating by passing current between anode and cathode rods in wells [14].

ExxonMobil Electrofrac: Hydraulic fractures are created in the formation, then filled with an electrically conductive material such as calcined petroleum coke [19] to form resistive heating elements. The electrical continuity of the fracture elements remains unaffected by the geological transformations that occur during kerogen conversion [20].

1.2 Overview of Solid Oxide Fuel Cell Technology

Fuel cells are galvanic cells, in which the free energy of a chemical reaction is converted into electrical energy by means of an electric current [21]. Solid oxide fuel cell technology entails the high-efficiency conversion of hydrocarbon fuels to electric energy. SOFCs are currently considered a viable power source for stationary or distributed power plants [22, 23]. During SOFC operation, oxygen ions (O_2^-) are formed from the oxidant (usually air) on the cathode side of the cell then these ions pass through the electrolyte to the anode-electrolyte interface where they react with the hydrogen and carbon monoxide contained in the fuel, generally derived from reformed hydrocarbons. This electrochemical reaction results in the production of carbon dioxide, water and electrons that flow through an external circuit to the cathode-electrolyte interface [24, 25]. The Colorado Fuel Cell Center does a lot of work on ceramic proton conductors. These are "solid oxide," but transport hydrogen ions (H^+) rather than oxygen ions. The fuel cells in the GFCs are based around ceramic oxygen-ion conductors, specifically yttria-stabilized zirconia.

The high operating temperatures required for SOFCs (700 –1000 °C), make them suitable for CHP applications when coupled with heat recovery systems. Studies show that a combined heat and electric work efficiency value greater than 85% is possible in SOFC–CHP

systems [26–31]. In the context of commercial and residential building design, optimized SOFC–CHP systems have been shown to result in an energy-efficient and low-CO_2-emitting alternative power and thermal energy co-generation technology [32–36]. In most SOFC system designs, a burner is added downstream of the SOFC exhaust to combust excess fuel for heat to drive endothermic fuel processing. To further increase the system efficiency, the hot burner exhaust can be expanded through a gas turbine (GT), then passed through heat exchangers to utilize as much of the remaining thermal energy as possible. These hybrid systems (SOFC–GT) containing SOFCs and GTs have been shown to produce tens to hundreds of electrical kilowatts (kW_e) at high efficiencies and low emissions [37–39].

Additionally, SOFC systems can to operate under a wide range of fuel compositions such as natural gas, LPG, methanol, or coal gasified gas that are internally reformed on the anode side of the cell [24]. Biogas' high levels of carbon dioxide make it undesirable for conventional power-generation systems, but SOFC's insensitivity to fuel composition present a potential solution. This increasing interest in utilizing carbon-based fuels for distributed power generation at low emissions have made SOFC–GT systems a promising technology in renewable energy research and development [32, 37, 40–42].

Unlike most SOFC-CHP applications, the GFC application places higher value on high-grade thermal-energy generation at the expense of electricity generation. The objective of the system is to reject high-grade heat from the GFC assembly at temperatures greater than 500 °C to the surrounding geology. This use of heat from SOFCs to make oil is novel.

1.3 Dissertation Outline

This dissertation is comprised of four chapters that study the design, testing, modeling and optimization of the Geothermic Fuel Cell technology as a novel combined heat and power application of solid-oxide fuel cells for in situ oil shale production. In chapter 2, we describe experimental testing and performance characteristics of two Geothermic Fuel Cell prototypes. Delphi Powertrain systems designed and built two GFC prototypes comprised of three 1.5-kW_e solid oxide fuel cell (SOFC) stack-and-combustor units packaged within a

0.3 m-diameter, 1.8 m-tall, stainless-steel housing. A test stand was built at the Colorado Fuel Cell Center to monitor operation and performance of the GFC modules in a controlled setting. Thermocouple and flow data was converted into thermodynamically meaningful metrics such as the system heating and electrical efficiency and the heat flux to the surroundings. We explored different operating state points and categorized them into energy flows into and out of the system, thereby obtaining a first-law analysis of GFC operation and the trade-offs between electricity generation and heating. We identified sensor data necessary for the calibration and validation of computational models developed to simulate GFC performance.

In Chapter 3, we describe experimental testing and performance characteristics of a Geothermic Fuel Cell assembly installed in the earth and continuously operated for ~ 600 hours. Three cylindrical GFC modules, each containing three 1.5 kWe solid-oxide fuel cell stacks, were mechanically and electrically coupled and joined to a gas-preheater/heat-exchanger assembly. The 9-m-long assembly was placed within the earth, integrated with extensive balance-of-plant components, controls, and diagnostics, then continuously operated over a period of approximately 600 hours. Experimental data was gathered, and the effectiveness of the GFCs in heating the surrounding geology while simultaneously generating electricity was demonstrated. We suggest ways to improve the system performance by studying the Geothermic Fuel Cell in these conditions and its interaction with the natural-gas fuel processor, reactive-gas preheater, and ancillary balance-of-plant and diagnostic components.

In Chapter 4, we describe a steady-state system model that simulates the electrochemical performance and thermal-energy generation of the GFC assembly. During its application, GFC modules will be buried under approximately 250-600 m (800-1900 ft) of overburden, making it challenging to monitor performance using sensors; hence, there is a need for a model to simulate GFC performance. We utilized user-defined subroutines in a steady-state Aspen Plus system model to predict the GFC-stack electrochemical performance and the heat-rejection from the module. The model is used to explore a wider range of operating conditions

than can be experimentally tested, and provides insight into the competing physical processes at play during Geothermic Fuel Cell operation.

In Chapter 5, we describe a nonlinear multi-objective optimization model for the design and dispatch of a single GFC heater well. The goal of the model is to appropriately size, configure and operate the GFC system and its auxiliary components at low costs and high thermo-electric efficiencies. A key result of the optimization study is calculation of the production cost per barrel of oil at the wellhead, for the crude oil produced using the Geothermic Fuel Cell technology. The model contains an extensive set of mathematical equations and expressions that represent the economic, physical and operational constraints on the system. The electrochemical and thermal performance of the GFC modules is based on previous modeling work presented in Chapter 4, while the performance of other balance of plant components that make up the system is based on literature sources. The geology heat requirements as well as oil and gas production rate data was obtained from a comprehensive simulation model of kerogen pyrolysis for the in-situ upgrading of oil shale developed by Dr. Kyung Jae Lee at Berkeley National laboratory [43–46]. Economic data is collected from component manufacturers and literature for use in the cost minimization objective and to arrive at an optimal $/barrel value. The objective of the design problem is to maximize the length and number of SOFC stacks for a single GFC heater well, while ensuring the electric power from the SOFCs is enough to power the compressor and pumps at maximum reactant flow rate conditions. Note that this objective function results in a thermally self-supporting GFC system. Once the GFC heater length and number of stacks per well is established, the dispatch model adjusts the system operating current, fuel and air utilizations to meet the geology heating requirements and compressor and pump electric power demands at lowest costs and highest efficiencies. The thermo-electrical portion of the dispatch model will generate component sizing information that includes; the required reactant flow rates, the compressor and pump power demands, the heat-exchanger size and effectiveness, and the fuel requirements for reformer sizing.

Chapter 6 summarizes our contributions and suggest ideas for future work.

CHAPTER 2

EXPERIMENTAL TESTING OF A NOVEL KILOWATT-SCALE MULTISTACK SOLID-OXIDE FUEL CELL ASSEMBLY FOR COMBINED HEAT AND POWER

This chapter describes experimental testing and performance characteristics of two "Geothermic Fuel Cell" module prototypes. The results of this demonstration were submitted and accepted for publication [47].

2.1 Introduction

The world's first Geothermic Fuel Cell prototypes were designed and built by Delphi Powertrain Systems (Fenton, MI, USA) [48–59]; their performance was characterized at the Colorado Fuel Cell Center (Golden, CO, USA). Following indoor, laboratory operation and validation of two GFC modules, three (3) three-stack modules were assembled into a single nine-stack GFC assembly. The assembly was integrated with a natural gas fuel processor and ancillary components, and operated underground within the geology at the Colorado School of Mines campus. A fairly narrow operating range was explored for these in-ground tests, as presented in Sullivan et al. [60].

This chapter focuses on indoor laboratory testing of the single three-stack Geothermic Fuel Cell module shown in Figure 2.1. Unlike the in-ground report, a more-detailed description of GFC module design is provided, while balancing the intellectual-property concerns of the GFC developers. In contrast with the outdoor testing, GFC operation is explored over a far-wider range of conditions within the indoor laboratory environment. Fuel composition is varied between hydrogen and reformed natural gas. Electric current draw spans 30 - 45 A (1.84 - 3.01 kW_e). While fuel utilization is held nearly constant at 63%, the effects of combusting the unspent fuel within the GFC assembly is explored. For all conditions tested, GFC performance is presented from the perspectives of electricity generation and heat liberation to the surrounding environment. Control strategies and potential failure modes are

discussed.

2.2 Experimental

Two Geothermic Fuel Cell module prototypes were tested at the Colorado Fuel Cell Center laboratory. GFC operation was explored over a wide range of conditions within the indoor laboratory environment. In this section the GFC laboratory experimental setup is described.

2.2.1 Geothermic Fuel Cell module

The Geothermic Fuel Cell module is comprised of three 1.5-kW$_e$ SOFC stack-and-combustor assemblies packaged within a 0.3-m-diameter stainless-steel housing (Figure 2.1). This 2.5-m-tall housing promotes ease of installation within a circular bore hole drilled into a geological formation. The stacks are vertically distributed to promote uniform housing surface temperatures and balanced heat rejection to the geology.

Delphi's "Gen3" SOFC stacks are used within the GFC module. The membrane-electrode assembly within each stack repeat unit consists of a nickel-yttria-stabilized zirconia (Ni-YSZ) "cermet" anode support, a YSZ electrolyte, and a lanthanum strontium cobalt ferrite (LSCF) cathode. Each cell has an active area of 105 cm^2, and a total thickness of 550 μm. Stacks utilize stamped metallic interconnects and laser-welded repeat units. Additional cell and stack details are presented in Mukerjee et al. [61, 62].

The Gen3 stack technology was originally developed with support from the U.S. Department of Energy Solid State Energy Conversion Alliance (SECA). Target applications included use as auxiliary power units (APU) for long-haul, diesel-fueled tractor tailors. Challenges for the APU application include high-performance operation on diesel reformate under significant vibration over hundreds of thermal cycles. The Geothermic Fuel Cell application presents a potentially less-challenging environment, where steady, stationary operation on reformed natural gas is required.

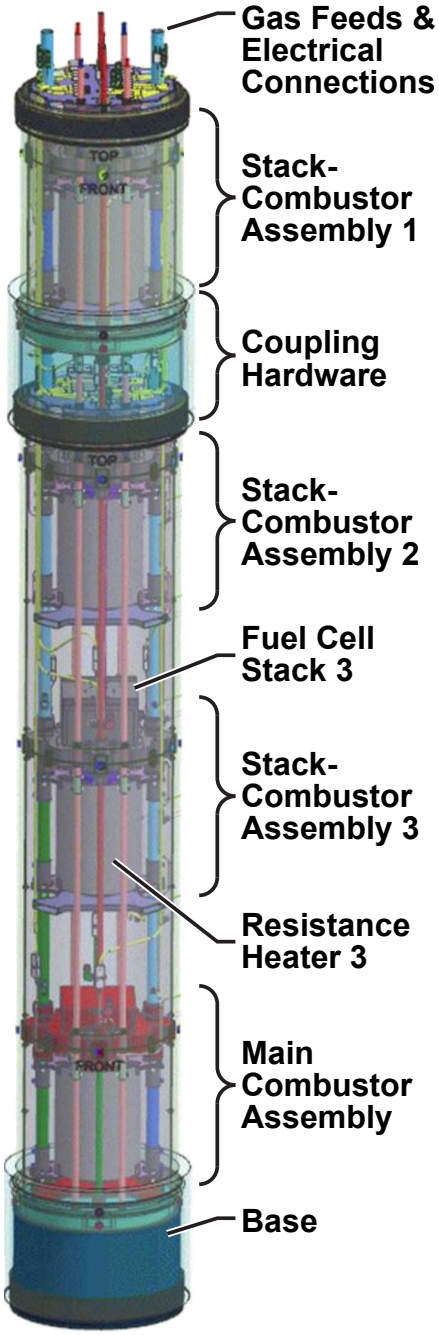

Figure 2.1: Schematic of the Geothermic Fuel Cell module.

As shown in Figure 2.1, reactive gases are supplied to the GFC module through the top of the housing, and feed three stack-and-combustor assemblies in a parallel configuration. A portion of the reactants fed to each assembly is electrochemically converted to electricity and products within the SOFC stack. Following electrochemical oxidation, anode and cathode exhaust gases can mix and burn within a combustor located below the stack. Alternately, the anode exhaust can vent to the atmosphere through "anode-return" plumbing (not shown). The flow of unconverted fuel between the combustors and the anode return is regulated with mechanical valving. The return of unreacted fuel to module exhaust provides operational flexibility, enabling alteration in heat release without overly impacting electricity generation. Hot product gases exit the combustors and flow upwards through an annular space between two stainless steel housings, rejecting heat to the surroundings before being exhausted above ground. While gas plumbing utilizes a parallel architecture, the three SOFC stacks are connected in electrical series, with connections at the top of the module.

The Geothermic Fuel Cell module includes a fourth main combustor located in the base of the unit. This combuster is fed with reactants supplied in parallel with the three stack-combustor assemblies. As with the stack-combustor assemblies, hot exhaust products from the main combustor are vented to the GFC annulus, providing a high-temperature jacket around the module that promotes thermal uniformity. The GFC module shown in Figure 2.1 includes a coupling unit to mechanically and electrically connect the first stack-combustor assembly to the assemblies below it. This hardware enables joining of a string of GFC modules as desired for the application. Four electric-resistance heaters are distributed within the assembly for use in startup. The module base is sealed to prevent convective air flow into the module interior. Further detail of the GFC design can be found in Delphi's GFC patent portfolio [48–59].

2.2.2 GFC test stand and experimentation

A Geothermic Fuel Cell test stand was designed and built at the Colorado Fuel Cell Center to characterize GFC operation and performance, and provide insight on potential

design improvements. A process-flow diagram of the Geothermic Fuel Cell test bench is shown in Figure 2.2. The GFC module is fueled from either of two sources. One stream is comprised of a H_2-N_2 mixture that can be widely varied using mass flow controllers (MFC). This fuel stream is humidified using precision water pumps.

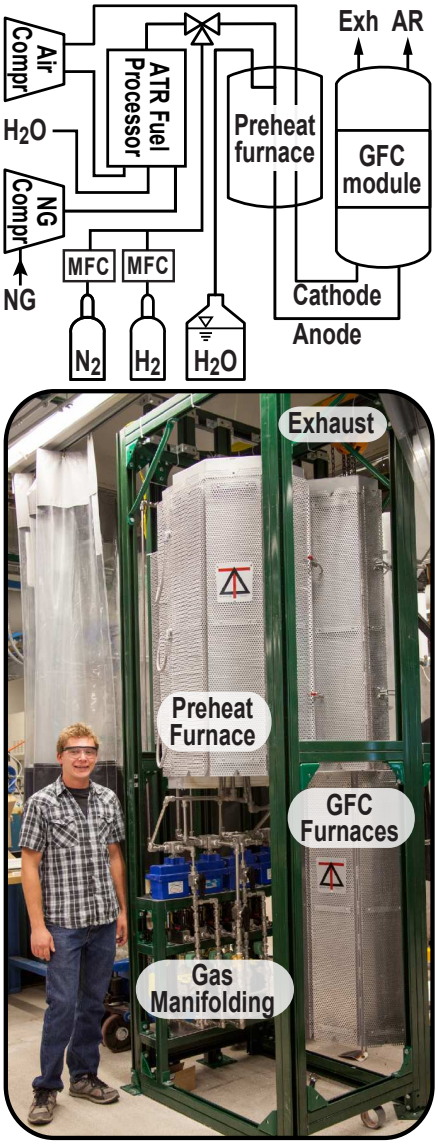

Figure 2.2: Process flow diagram of Geothermic Fuel Cell test bench (top) and test stand image (bottom).

Alternately, the GFC module can be fueled from reformate produced by a natural gas fuel processor designed and built by Precision Combustion, Inc. (Northaven, Connecticut, USA)

[63]. The fuel processor generates reformate by desulfurizing municipal natural gas (NG), mixing with steam and air, and flowing the mixture over a proprietary catalyst held at high temperature. A compressor is used to pressurize the natural gas to 310 kPa upstream of the fuel processor. A wide range of steam-to-carbon (S/C) and oxygen-to-carbon (O/C) ratios can be fed to this "authothermal" (ATR) fuel reformer to modify reformate composition for meeting GFC operational needs. The reformer can continuously generate between 9 and 35 kW_{th} of hydrogen, based on H_2 lower heating value (LHV). Reformate composition matches chemical-equilibrium predictions, as confirmed using gas chromatography.

Reactant gases are preheated by routing through alumina-coated inconel tubing housed within a 25-kW electric furnace. The GFC is housed within two 25-kW electrical furnaces to maintain a temperature-controlled environment. Following initial experimentation, the GFC modules demonstrated thermally self-sustained operation. Following these initial tests, the heating elements for the electric furnaces were not, in fact, powered. Exhaust gases exiting the GFC are directed upwards into a fume hood.

The experiment is controlled and diagnostics collected using National Instruments compactRIO hardware and LabView software. GFC electricity generation is regulated using Kikusui electronic load banks. The Geothermic Fuel Cell assembly has extensive instrumentation for monitoring GFC operation and performance, with 123 parameters that are periodically logged during operation.

The Geothermic Fuel Cell module operates within a set of fixed constraints; these include:

1. Minimum stack temperature: 700 °C;
2. Inlet gas temperature: 600 - 750 °C;
3. Maximum temperature difference between the cathode and anode inlet streams: 100 °C;
4. Maximum temperature difference between cathode inlet and outlet streams: 125 °C;

5. Fuel utilization: 40 - 70 %;

6. Fuel composition: 30 % $< H_2 <$ 50%; S/C > 2;

The GFC module is gradually brought to operating temperature by flowing a H_2-N_2 mixture to the assembly, and then igniting the combustors. This releases significant heat within the GFC interior that gradually increases the stack temperatures to the minimum level for electricity generation. This heat can be supplemented by the electric-resistance heaters housed within the GFC module. Approximately 12 hours is required to heat the module to operating temperature. Following startup, the fuel source can be switched from H_2-N_2 to reformate using mechanical valving.

2.3 Thermodynamic model

The performance of the Geothermic Fuel Cell module is analyzed using Engineering Equation Solver (EES). EES is used to capture the gross transport of chemical, thermal and electrical energy to and from the GFC. The model converts experimental data regarding gas flow rates and temperatures into thermodynamic system metrics. Gross system performance, including heat loss to the surroundings $\dot{Q}_{\text{loss}}$, is quantified using mass and energy balances, chemical equilibrium, and reaction kinetics [29]:

$$\dot{E}_{\text{total}} = \dot{E}_{\text{fuel}} + \dot{E}_{\text{air}} = \dot{Q}_{\text{loss}} + \dot{E}_{\text{ann}} + \dot{E}_{\text{ar}} + \dot{W}_{\text{elec}}. \tag{2.1}$$

In this energy balance, the fuel and air streams bring energy $\dot{E}_{\text{total}}$ into the GFC module:

$$\dot{E}_{\text{fuel}} = \dot{E}_{\text{fuel,sens}} + \dot{E}_{\text{fuel,chem}} \tag{2.2}$$

where $\dot{E}_{\text{fuel}}$ is the sum of the sensible and chemical energy of the preheated fuel stream $\dot{E}_{\text{fuel,sens}}$ and $E_{\text{fuel,chem}}$ flowing at temperature T_{fuel} and molar flow rate $\dot{n}_{\text{fuel}}$:

$$\dot{E}_{\text{fuel,sens}} = \dot{n}_{\text{fuel}} \sum_j X_j \cdot \left[\bar{h}_j(T_{\text{fuel}}) - \bar{h}_j(T_0)\right] \tag{2.3}$$

$$\dot{E}_{\text{fuel,chem}} = \dot{n}_{\text{fuel}} \sum_j X_j \cdot LHV_j \tag{2.4}$$

$\dot{E}_{\text{air}}$ is the sensible energy of the preheated air stream entering at temperature T_{air} and molar flow rate $\dot{n}_{\text{air}}$:

$$\dot{E}_{\text{air}} = \dot{n}_{\text{air}} \sum_j X_j \cdot \left[\bar{h}_j(T_{\text{air}}) - \bar{h}_j(T_0)\right]. \tag{2.5}$$

Energy outputs include the sensible energy in the exhaust products exiting the GFC annulus $\dot{E}_{\text{ann}}$ at temperature T_{ann}:

$$\dot{E}_{\text{ann}} = \dot{n}_{\text{ann}} \sum_j X_j \cdot \left[\bar{h}_j(T_{\text{ann}}) - \bar{h}_j(T_0)\right]. \tag{2.6}$$

$\dot{E}_{\text{ar}}$ is the sum of the sensible and chemical energy in the anode return $\dot{E}_{\text{ar,sens}}$ and $E_{\text{ar,chem}}$ exiting at temperature T_{ar}, molar flow rate $\dot{n}_{\text{ar}}$, and mole fractions $X_{j,\text{ar}}$:

$$\dot{E}_{\text{ar}} = \dot{E}_{\text{ar,sens}} + \dot{E}_{\text{ar,chem}} \tag{2.7}$$

$$\dot{E}_{\text{ar,sens}} = \dot{n}_{\text{ar}} \sum_j X_{j,\text{ar}} \cdot \left[\bar{h}_j(T_{\text{ar}}) - \bar{h}_j(T_0)\right] \tag{2.8}$$

$$\dot{E}_{\text{ar,chem}} = \dot{n}_{\text{ar}} \sum_j X_{j,\text{ar}} \cdot LHV_j \tag{2.9}$$

The total sensible energy leaving the GFC module is $\dot{E}_{\text{sens,out}}$:

$$\dot{E}_{\text{sens,out}} = \dot{E}_{\text{ann}} + \dot{E}_{\text{ar,sens}} \tag{2.10}$$

The electric power output is $\dot{W}_{\text{elec}}$, and the heat loss to the surroundings is $\dot{Q}_{\text{loss}}$. Note that $\dot{Q}_{\text{loss}}$ is a heat flow due to the temperature difference between the GFC outer casing and the surroundings. This heat loss to the surroundings is not explicitly measured. Rather, it is inferred from the differences in chemical and sensible energy entering and exiting the module (Eq. 2.1).

The mole fractions, molar enthalpy and lower heating values of each species j in the fuel and air streams are given by X_j, $\bar{h}_j$ and LHV_j, respectively. The sensible energy is defined as the amount of energy that can be harnessed by cooling the hot inlet and outlet gases back to ambient temperature (298 K). This is represented by the difference in species enthalpy at the respective stream temperature (T) and the ambient temperature (T_0), i.e., $[\bar{h}_j(T) - \bar{h}_j(T_0)]$. The inclusion of LHV_j in the $\dot{E}_{\text{ar}}$ calculation reflects the presence of unconsumed H_2 in the

anode return stream. The quantity of H_2 remaining following electrochemical conversion is determined based on the current being generated by the stacks, assuming 100% faradaic efficiency:

$$\dot{n}_{\mathrm{H_2,utilized}} = \frac{I}{n\ F} \cdot n_{\mathrm{cells}} \tag{2.11}$$

$$\dot{n}_{\mathrm{H_2,unutilized}} = \dot{n}_{\mathrm{H_2,fuel}} - \dot{n}_{\mathrm{H_2,utilized}}. \tag{2.12}$$

The values are used to determine the mole fractions in the anode exhaust stream following electrochemical oxidation $X_{j,\mathrm{ar}}$.

The molar flow rates into the fuel and air feed streams are regulated using mass flow controllers (Figure 2.2). Fuel flow rates are set to meet fuel utilization (U_{fuel}) constraints:

$$U_{\mathrm{fuel}} = \frac{\dot{n}_{\mathrm{H_2,utlized}}}{\dot{n}_{\mathrm{H_2,fuel}}} \tag{2.13}$$

This results in a total anode flow rate of

$$\dot{n}_{\mathrm{fuel}} = \frac{\dot{n}_{\mathrm{H_2,fuel}}}{X_{\mathrm{H_2}}} \tag{2.14}$$

where $X_{\mathrm{H_2}}$ is the mole fraction of H_2 in the fuel feed stream. Similarly, cathode flow rate is set to achieve the desired stoics of excess air (λ) as given by the ratio of moles of O_2 supplied to the moles of O_2 consumed by the stacks during electrochemical oxidation of H_2:

$$\lambda = \frac{\dot{n}_{\mathrm{O_2,air}}}{\dot{n}_{\mathrm{O_2,utilized}}}. \tag{2.15}$$

This results in a total cathode flow rate of:

$$\dot{n}_{\mathrm{air}} = \frac{\dot{n}_{\mathrm{O_2,air}}}{X_{\mathrm{O_2}}}. \tag{2.16}$$

As described earlier, gas flow out the anode return can be shut off using mechanical valving. This directs unburned fuel to the stack combustors. As such, molar flow rate through the anode return is either $\dot{n}_{ar} = \dot{n}_{fuel}$ or 0 with the anode return valve open or closed, respectively.

The GFC electrical efficiency ϵ_{elec} is calculated as the ratio of electric power output to the chemical energy in the fuel feed [64–68]:

$$\epsilon_{\text{elec}} = \frac{\dot{W}_{\text{elec}}}{\dot{n}_{\text{H}_2} \cdot LHV_{\text{H}_2}} \tag{2.17}$$

The system heating efficiency is based on the chemical and sensible energy contained in the fuel and air inlet streams ($\dot{E}_{\text{fuel}}$ and $\dot{E}_{\text{air}}$).

$$\epsilon_{\text{heat}} = \frac{\dot{Q}_{\text{loss}}}{\dot{E}_{\text{fuel}} + \dot{E}_{\text{air}}}. \tag{2.18}$$

The net combined heat-and-power efficiency ϵ_{CHP} is given by the sum of the heating and electrical efficiencies:

$$\epsilon_{\text{CHP}} = \epsilon_{\text{elec}} + \epsilon_{\text{heat}} \tag{2.19}$$

The linear heat flux is the rate of heat transferred to the surrounding geology ($\dot{Q}_{\text{loss}}$) per unit length of the GFC module:

$$\dot{Q}'_{\text{loss}} = \frac{\dot{Q}_{\text{loss}}}{\text{GFC length}} \tag{2.20}$$

2.4 Results and discussion

Geothermic Fuel Cell module performance is described at seven operational state points listed in Table 2.1. Key inputs and observables include reactant-gas compositions, flow rates and inlet temperatures, product-gas outlet temperatures, anode return state (open or closed), and electronic load. The values shown represent conditions after a minimum of four hours of steady-state operation at each condition. These raw data are converted to chemical, sensible, and electrical energy entering and exiting the Geothermic Fuel Cell, and overall GFC efficiencies.

Statepoint 2 serves as an example. For this condition, the fuel feed is the H_2-N_2 mixture, the anode return is open, and 35 A of current are drawn from the GFC module. There is $\dot{E}_{\text{total}} = 15.5$ kW of chemical and sensible energy delivered to the GFC through the hot reactant gas streams. The reactant-gas inlet temperatures T_{fuel} and T_{air} differ by 67 °C,

Table 2.1: Operational state points and performance of the Geothermic Fuel Cell module.

Parameter	Unit	State Point						
		1	2	3	4	5	6	7
Fuel type		H_2/N_2	H_2/N_2	H_2/N_2	H_2/N_2	H_2/N_2	H_2/N_2	NG
Current	A	30	35	45	30	35	45	30
Voltage	V	68.3	69.1	66.0	70.0	70.0	66.9	61.3
Anode return		Open	Open	Open	Closed	Closed	Closed	Closed
Fuel flow rate	SLPM	88.4	103.2	132.6	88.4	103.2	132.6	122.0
Air flow rate	SLPM	360	360	375	350	315	550	350
U_{fuel}	%	63.3	63.1	62.7	63.0	63.0	62.7	62.5
T_{fuel}	°C	676	692	611	640	662	575	600
T_{air}	°C	762	759	611	678	697	524	633
T_{stack}	°C	769	784	801	768	785	801	744
T_{ar}	°C	647	668	654	652	669	662	N/A
T_{ann}	°C	571	600	610	634	648	664	561
T_{housing}	°C	562	593	605	628	642	662	547
$\dot{W}_{\text{elec}}$	kW	2.05	2.42	2.97	2.10	2.45	3.01	1.84
$\dot{E}_{\text{fuel,chem}}$	kW	7.27	8.50	10.93	7.30	8.51	10.93	7.32
$\dot{E}_{\text{fuel,sens}}$	kW	1.22	1.46	1.64	1.14	1.39	1.53	1.55
$\dot{E}_{\text{fuel}}$	kW	8.49	9.96	12.57	8.44	9.90	12.46	8.87
$\dot{E}_{\text{air}}$	kW	5.61	5.59	4.59	4.80	4.46	5.68	4.44
$\dot{E}_{\text{total}}$	kW	14.1	15.55	17.16	13.24	14.36	18.14	13.31
$\dot{E}_{\text{ar,chem}}$	kW	1.91	2.25	2.92	0.00	0.00	0.00	0.00
$\dot{E}_{\text{ar,sens}}$	kW	0.95	1.15	1.44	0.00	0.00	0.00	0.00
$\dot{E}_{\text{ar}}$	kW	2.86	3.40	4.36	0.00	0.00	0.00	0.00
$\dot{E}_{\text{ann}}$	kW	4.25	4.51	4.84	5.52	5.39	9.06	6.21
$\dot{E}_{\text{sens,out}}$	kW	5.20	5.66	6.28	5.52	5.39	9.06	6.21
$\dot{Q}_{\text{loss}}$	kW	4.94	5.21	4.98	5.61	6.52	6.07	5.26
ϵ_{elec}	%	28.2	28.5	27.2	28.8	28.8	27.5	25.2
ϵ_{heat}	%	35.0	33.5	29.0	42.4	45.4	33.5	39.5
ϵ_{CHP}	%	63.2	62.0	56.2	71.2	74.2	61.0	64.7
$\dot{Q}'_{\text{loss}}$	kW m^{-1}	2.02	2.14	2.04	2.30	2.67	2.49	2.16

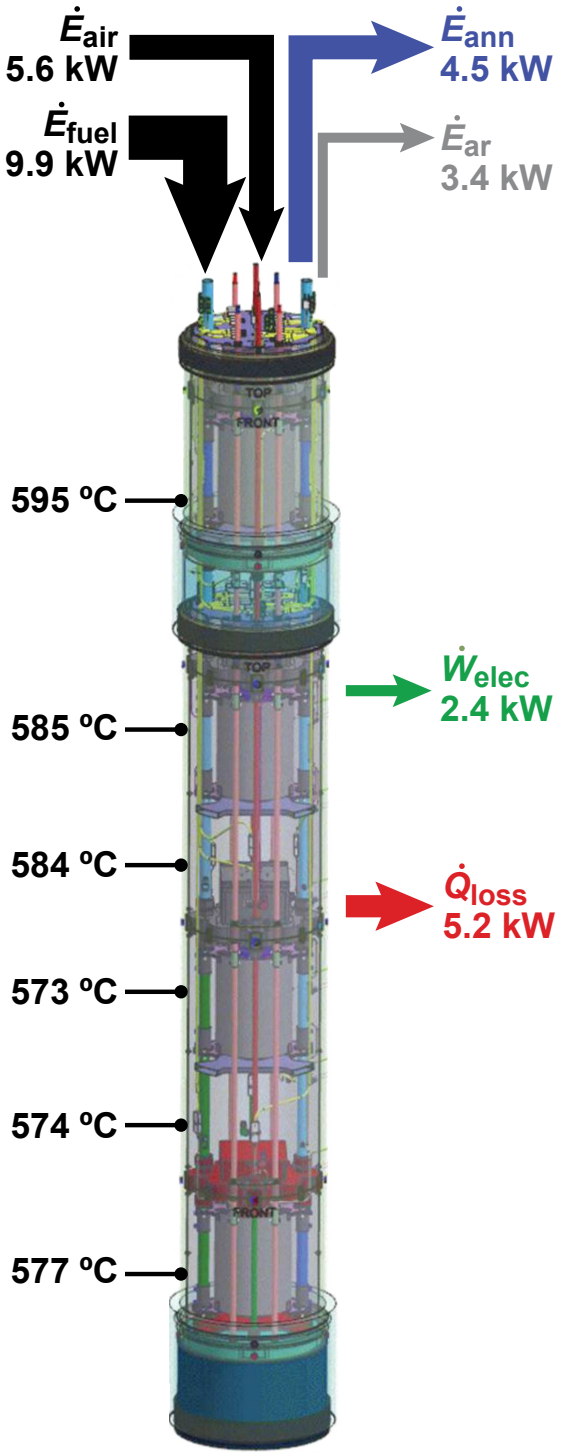

Figure 2.3: Surface temperatures and energy flows into and out of the Geothermic Fuel Cell module. Values are shown for the 35-A quasi-steady-state condition. Arrows are scaled to reflect the relative magnitude of energy flow entering and exiting the GFC module.

revealing a limitation in the experimental test bench. While uniform, well-controlled inlet temperatures are desired, some variability is found due to dissimilar heat transfer within the preheat furnace.

Module surface temperatures at State Point 2 are shown in Figure 2.3, ranging from 573 to 595 °C, a difference of only 22 °C. These temperatures are near the 600 °C target for in-ground GFC operation and in-situ oil-shale processing [60]. The average housing temperatures T_{housing} are listed in Table 2.1. The bulk flows of energy entering and exiting the module are also shown in this figure; the arrows are scaled to represent the relative magnitudes of these energy flows. GFC electric power output reaches $\dot{W}_{\text{elec}} = 2.42$ kW$_e$, well below the rated output of 4.5 kW$_e$. This is in keeping with the unique GFC application; as the primary objective is to heat the surroundings, lower levels of electricity are generally desired. This is also reflected in the fairly low fuel utilization of 63.1%, resulting in a modest electric efficiency of $\epsilon_{\text{elec}} = 28.5\%$.

With $\dot{Q}_{\text{loss}} = 5.21$ kW of thermal energy released to the GFC surroundings, the combined heat-and-power efficiency reaches $\epsilon_{\text{CHP}} = 62\%$. This fairly low value is attributed to the considerable unconverted chemical energy exiting the GFC through the anode return ($\dot{E}_{\text{ar,chem}}$ = 2.25 kW). At this condition, the GFC linear heat flux reaches 2.1 kW m^{-1}. This value exceeds initial targets of 1.6 kW m^{-1} [60].

The distribution of energy outputs from the GFC is shown in Figure 2.4. Heat loss to the surroundings is a large fraction of the total, while again, electric power output is comparatively modest. The pie chart highlights the large fraction of thermal energy exiting in hot exhaust gases ($\dot{E}_{\text{sens,out}} = 5.66$ kW), and the significant chemical energy remaining in the unreacted fuel flowing out of the anode return ($\dot{E}_{\text{ar,chem}}$). Indeed, the effect of the anode return on GFC performance is pronounced.

Referring back to Table 2.1, State Points 1-6 explore the effects of current draw and anode return on operational performance under H_2-N_2 fuel. In general, higher current draws lead to overall higher module temperatures. This is a result of the increase in irreversible

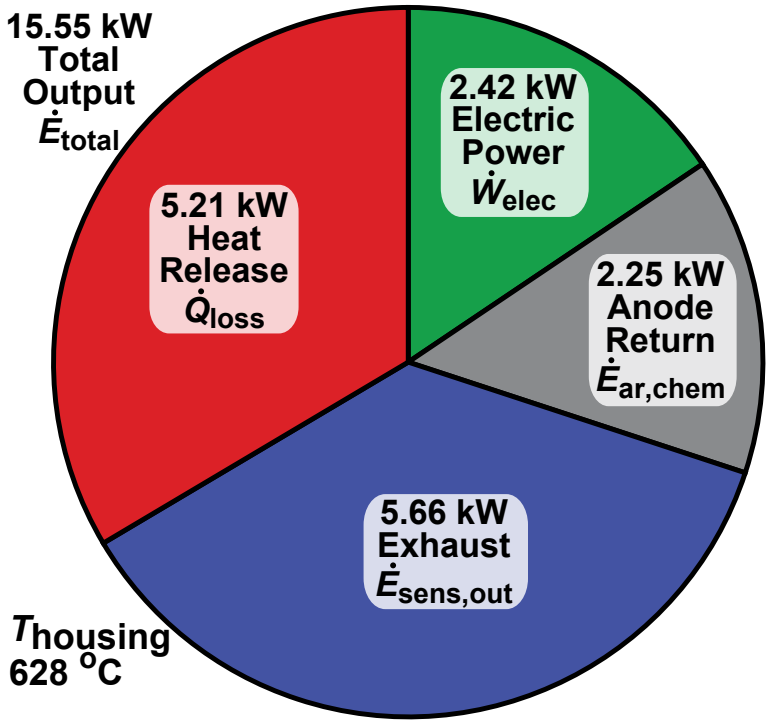

Figure 2.4: Distribution of energy outputs from the Geothermic Fuel Cell module at State Point 2 (35 A).

heat generation within SOFCs at higher currents.

Heating efficiencies ϵ_{heat} are found to drop at the highest electric-power conditions (45 A). These unexpected results can be traced to limitations of the test stand. Specifically, the higher-power condition necessitates increased reactant flow rates. These, in turn, put strain on the gas-preheat equipment that results in lower reactant-gas inlet temperatures. Thus, a larger fraction of the heat generated by the GFC module is transferred to the cooler reactant gas streams within the GFC interior. Indeed, the energy carried away in the exhaust gases ($\dot{E}_{sens,out}$) is maximized at these high-power, high-flow-rate, low-residence-time conditions.

The closed anode return at State Points 4, 5, and 6 activates the stack combustors, leading to much higher heat release, heating efficiency, and CHP efficiency. Linear heat flux is increased by over 30% from the low-power, open-anode-return conditions, demonstrating the flexibility of the GFC module for meeting operational requirements.

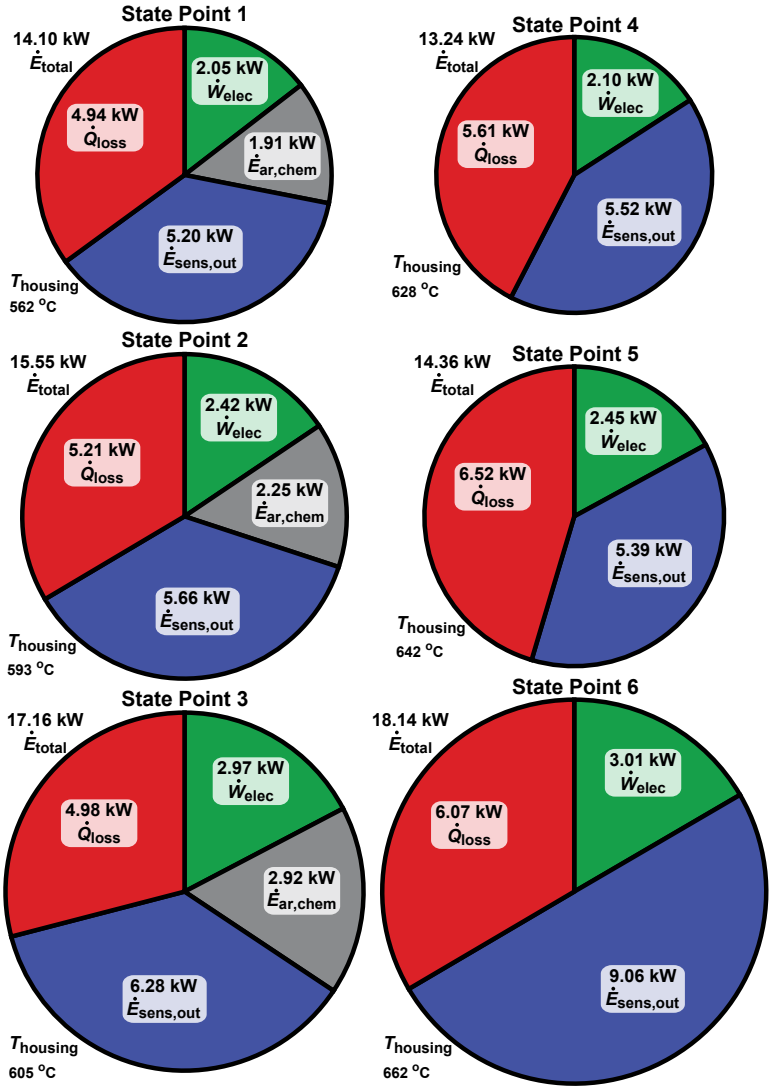

Figure 2.5: Distribution of energy outputs from the Geothermic Fuel Cell module under H_2-N_2 fuel. The size of each pie is scaled to reflect the total energy output at each state point.

Close inspection of the data in Table 2.1 yields insight on the coupled nature of the GFC components and test stand. For example, the current draw increases from 30 to 35 A between State Points 4 and 5, respectively. However, the module voltage (70 V) is identical for the two conditions. This counter-intuitive result is traced to the slight increase in average stack temperature T_{stack} for the two conditions. The higher stack temperature of State Point 5 reduces overpotentials and improves electrochemical performance, albeit at potentially higher degradation rates than those found at lower operating temperatures. The increase in T_{stack} is due to the higher electrochemical output, and the higher inlet gas temperatures caused by increasing heat-transfer coefficients found at higher flow rates. Many additional examples of such thermal-electrochemical coupling could be presented.

The gross distributions of energy outputs for the six H_2-N_2 State Points are shown in Figure 2.5. For the lower electric current conditions (30 and 35 A), heat transfer to the surroundings $\dot{Q}_{\text{loss}}$ is found to increase substantially with the anode return closed, while the heat loss to the exhaust $\dot{E}_{\text{sens,out}}$ increases only slightly. Increased heat loss is also found at the high-current condition (45 A), but a much-larger fraction of the heat generated by the stack combustors is carried out in the exhaust stream in comparison to the lower-current conditions.

State Point 7 reflects performance under natural-gas reformate fuel at the 30-A condition. Reformer operation was held at a steam-to-carbon ratio of 1.0 and a oxygen-to-carbon ratio of 1.2, producing a reformate composition of 23.7% H_2, 10.4% CO, 2.4% CO_2, 0.2% CH_4, and 29% H_2O and 33.7% N_2. Noticably lower terminal voltage and module power is observed, reflecting the significantly higher steam content and lower hydrogen partial pressure found in the reformate in comparison to the H_2-N_2 fuel (3% steam). Generally lower module temperatures (T_{stack}, T_{ann}, T_{housing}) are observed in comparison to the two other 30-A State Points (1 and 4), though the anode return is closed, and all reformate is converted to products within the GFC. Despite some compromises in electrochemical performance, overall module performance under reformate remains comparable to the H_2-N_2 conditions, with the

combined heat-and-power efficiency reaching $\epsilon_{\mathrm{CHP}} = 64.7\%$. Linear heating remains strong at 2.16 kW m^{-1}.

This modest CHP efficiency can be improved through GFC system-design changes. For example, the hot exhaust gases exiting the GFC can be used to preheat the cool reactants, decreasing the sensible energy load. In practice, the reactant and exhaust plumbing will be co-located within a single bore hole, as performed in Sullivan et al. [60]. This makes for efficient transfer of heat between these fluid streams. Additionally, there is significant chemical energy in the unreacted fuel of the anode return. This energy can also be harnessed through combustion to preheat reactants, further decreasing the sensible energy load. Such measures were beyond the experimental scope of the present work.

It is important to note that the Geothermic Fuel Cell reported in this work was placed within a furnace containing refractory insulation. While the furnace elements were never activated and the GFC was not subjected to external heating, the furnace insulation served to keep heat within the GFC. During down-hole GFC operation within the geology, significant heat would be transported into the surrounding oil shale, decreasing GFC temperature, as found in Sullivan et al. [60]. As such, the measured GFC temperatures reported here are likely higher than those found during operation within the geology. Operating conditions that result in higher heat output would likely be necessary during down-hole operation.

2.5 Conclusions

This paper describes laboratory testing of a "Geothermic Fuel Cell," a novel application of solid-oxide fuel cells for combined heat and power. The Geothermic Fuel Cell is designed for operation within an underground oil-shale deposit, where it transfers heat into the geology to process oil shale into crude oil while generating electricity. The GFC module presented here is comprised of three 1.5-kW_e SOFC stack-and-combustor assemblies packaged within a stainless-steel housing that is 0.3 m in diameter and 2.5 m tall. A fourth, larger combustor is placed in the base of the module to promote thermal uniformity across the assembly. The module is fueled by either a humidified hydrogen-nitrogen mixture, or the products

of a natural-gas autothermal reformer. Exhaust products flow through an outer annulus, transferring heat to the surroundings. A number of operating conditions are explored and presented. One 35-A quasi steady-state condition resulted in 2.42 kW of electric power, a heat flux of 2.14 kW m^{-1} and a combined heat-and-power (CHP) efficiency of 62.0%. This operating point favors heat generation over electric power. Other operating conditions are presented; significant variations in efficiency and heat release are observed, with peak CHP efficiency reaching 74.2%.

The results of this experimental study of a single GFC module lead to the following inferences:

1. The GFC module can provide a substantial range of heat and electric-power outputs for meeting the requirements of in-situ oil-shale processing;

2. The GFC module design results in fairly uniform GFC surface temperatures, and consequently uniform geology heating;

3. GFC module heating can be regulated through variations of operating current and anode-return exhaust flow;

4. The anode-return plumbing enables a substantial turn down in GFC heat output while maintaining relatively high electric-power output;

5. In comparison to operation under enriched hydrogen fuel, CHP efficiency decreases by 8% under reformate fuel.

The experimental data set collected through this study is used to validate a computational model that simulates GFC performance and provides insight on the underlying physics behind GFC operation.

CHAPTER 3
IN-GROUND OPERATION OF GEOTHERMIC FUEL CELLS FOR UNCONVENTIONAL OIL AND GAS RECOVERY

This chapter describes the operating and performance characteristics of a Geothermic Fuel Cell assembly installed in the earth and continuously operated for $\sim$ 600 hours. The results of this demonstration were submitted and accepted for publication [60].

3.1 Introduction

The demonstration presented in this chapter involves a near-surface installation of nine (9) 1.5-kW$_e$ fuel cell stacks into a clay formation at the Colorado School of Mines campus. Fueled by municipal natural gas, this Geothermic Fuel Cell is integrated with a natural-gas fuel processor, a reactive-gas preheater, and ancillary balance-of-plant and diagnostic components at an outdoor test site. The Geothermic Fuel Cell was continuously operated within the earth for a period of 25 days. This chapter presents the results of this demonstration.

The U.S. Geological Survey estimates that over four trillion barrels of oil are trapped in the Piceance Basin of northwestern Colorado, the Uinta Basin of northeastern Utah, and the Greater Green River Basin of southwestern Wyoming [4, 5]. In contrast to liquid shale oil (or "tight oil") trapped within porous geology [7], oil shale is a sedimentary rock that contains organic matter called kerogen [8]. When pyrolysed to $\sim$ 350 °C [9], this kerogen decomposes into a mixture of oil, hydrocarbon gas and carbon-rich shale coke [10]. These oil-rich kerogen beds are buried below 250-600 m (800-1900 ft) of overburden, and can extend over 900 m (3,000 ft) below the surface at the center of the basins.

The processing of oil shale into oil is well established [6]. Traditionally, the shale rock is mined from the earth and then retorted above ground. Significant oil-shale retorts have been in operation for decades in Estonia, China, Russia, and other sites. Conventional oil-shale processing is not cost competitive with Middle East sources. Environmental impacts - surface

disturbance, water requirements, waste management - also present significant concerns [11]. Despite the enormity of this resource, its impact on the world energy portfolio remains modest [6].

Developers are turning to in-situ oil-shale processing to address these cost and environmental challenges. During in-situ processing, the oil-shale resource is retorted directly within the formation; this eliminates mining processes and minimizes surface operations [12]. Studies also show that in-situ processing leads to a significant increase in the energy yield, as greater volumes of oil shale can be processed at a time [13].

In-situ oil-shale processing is being pursued through a number of novel technologies, including:

- The "In-Situ Conversion Process" (ICP) led by Royal Dutch Shell; resistive heaters are inserted within the formation and driven with electric current to supply heat to the oil shale [10];
- The "Electrofrac Process" led by Exxon-Mobil; hydraulic fractures created in the formation are filled with an electrically conductive material to form resistive heating elements that are then driven with electric current to heat the oil shale [20];
- The "Volumetric Heating" method developed by Illinois Institute of Technology; radio waves generated by electrode arrays heat the formation [18];
- The "In-Situ Vapor Extraction Technology" pursued by Mountain West Energy; methane gas is heated above ground and injected into the oil-shale formation. A similar process is being developed by Chevron with carbon dioxide serving as the working fluid [14].

Geothermic Fuel Cells differ from these approaches in that electricity is generated throughout in-situ processing. This presents a unique Combined Heat and Power (CHP) application. In previous work, SOFC systems achieved CHP efficiencies approaching 85%

[2, 26–29, 69]. Unlike most CHP applications, in-situ oil-shale processing places higher value on down-hole thermal-energy release, at the expense of electricity generation. Addressing such operational tradeoffs and learning of the engineering challenges associated with underground SOFC operation motivate the current study.

3.2 Experiment

In this demonstration, a Geothermic Fuel Cell assembly was installed in the earth and continuously operated for ~ 600 hours. The GFC was fueled with natural gas that was passed through a fuel processor and converted into syngas. An extensive data set was acquired and used to quantify important performance metrics.

3.2.1 Geothermic Fuel Cell modules

A schematic of a single Geothermic Fuel Cell module is shown in Figure 3.1 This assembly is centered on three 1.5-kW$_e$ solid-oxide fuel cell stacks that are packaged and distributed within a cylindrical stainless steel housing. The housing is approximately 0.3 m (1 ft.) in diameter and 1.8 m (6 ft.) in height. Reactants are fed to the stacks in a parallel arrangement, while the stacks are connected in electrical series.

During operation, the fuel and air reactants fed to the stacks are electrochemically converted to products and electricity. Electrochemical oxidation occurs at ~ 750 °C ($\pm$ 70 °C) resulting in significant heat generation. This heat is liberated to the surrounding environment.

Prior to in-ground installation, Geothermic Fuel Cell prototypes were first tested in the Colorado Fuel Cell Center laboratory. These GFC modules included extensive instrumentation for monitoring GFC operation and performance. Indoor testing provided important insight to the unique operating characteristics of the GFC modules, and led to design modifications to improve performance and robustness.

For the in-ground demonstration, three GFC modules are joined using mechanical coupling. While the stacks within each module are connected in electrical series, the three

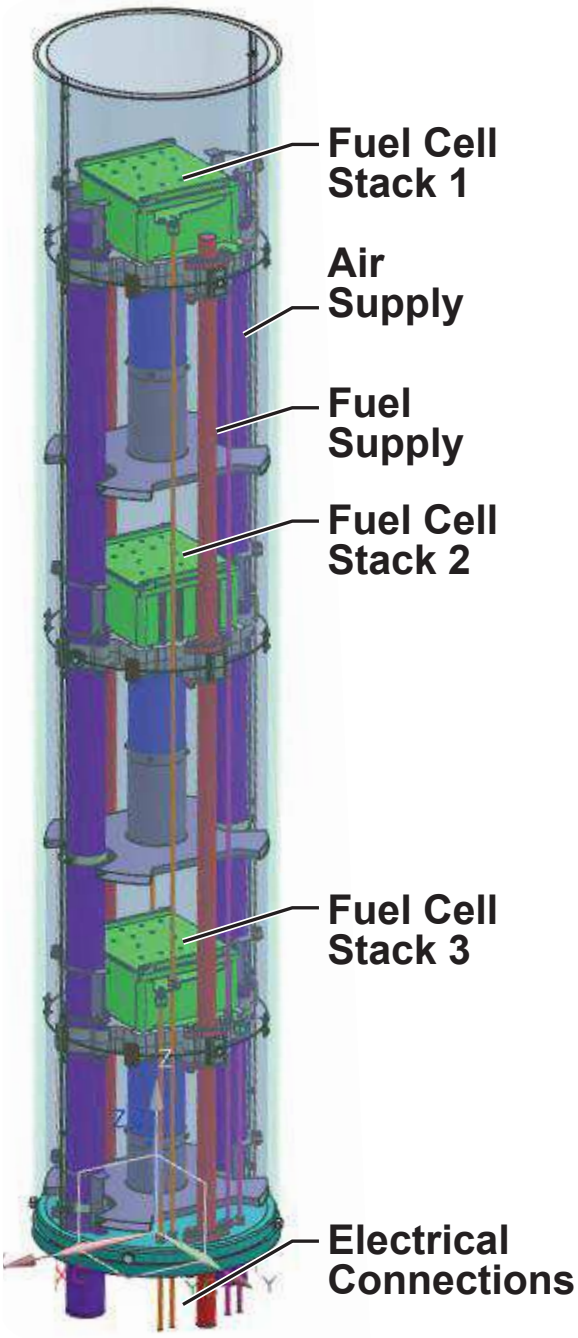

Figure 3.1: Schematic of a single Geothermic Fuel Cell module. Three such modules were joined and placed within the earth as part of this demonstration.

modules are connected in electrical parallel. The assembly contains a total of nine fuel cell stacks, extends 6 m in length, and has an electric power rating of 13.5 kW_e.

3.2.2 Outdoor test site description

The in-ground Geothermic Fuel Cell architecture is shown in Figure 5.1 Key elements include:

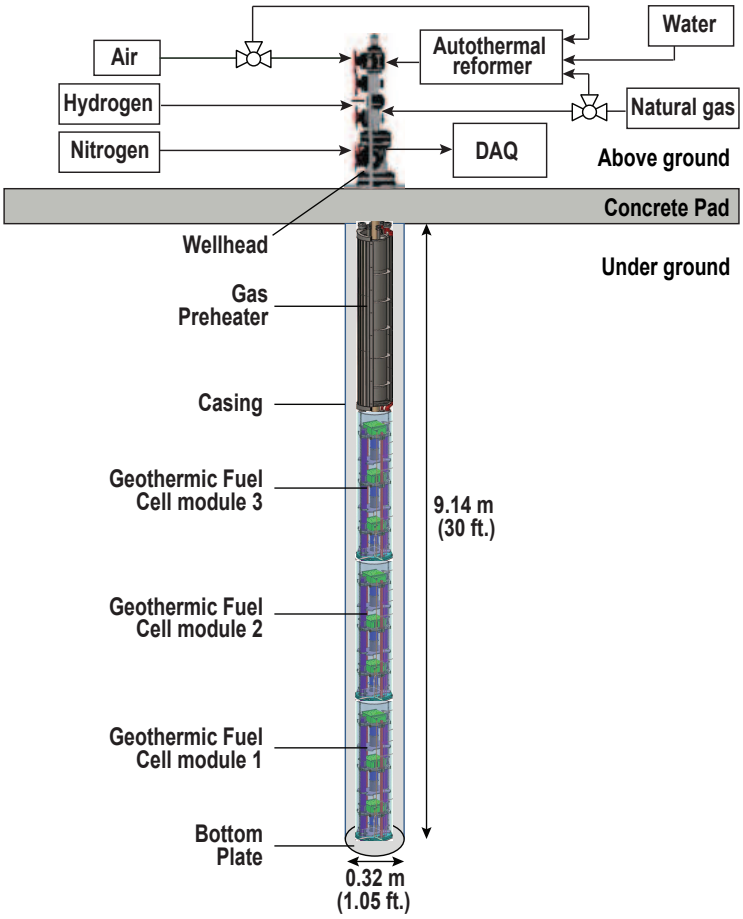

Figure 3.2: Geothermic Fuel Cell system architecture.

1. Three mechanically and electrically coupled Geothermic Fuel Cell modules;

2. A reactive-gas preheater attached to the top of the GFCs to heat the reactant gases that feed the GFC assembly;

3. A fuel reformer that converts natural gas supplied from the local municipality into syngas;

4. Control systems and diagnostics.

The GFC modules and preheat assembly are placed within a 0.76 m-diameter (2.5 ft.) steel casing that separates the assembly from the surrounding geology. The casing sits within a 9.14 m-deep (30 ft.) bore hole. The in-ground assembly hangs nine meters into the ground and is secured from above at the wellhead. A 1.2 m-tall (4 ft.) wellhead module secures the entire assembly to a 0.1 m-thick concrete pad from which the GFC-preheater assembly is suspended. The wellhead also serves as the interface for gas plumbing, the extensive diagnostic sensors, and electric power. As in the laboratory setting, the in-ground Geothermic Fuel Cell is fueled using a natural gas fuel reformer, with optional fueling using compressed hydrogen and nitrogen.

An illustration of the outdoor test site is provided in Figure 3.3 along with a photograph taken during GFC installation. The site consists of extensive materials and equipment for in-ground GFC operation and characterization including:

- Equipment trailer for housing of control and diagnostics hardware;
- Nearly 400 m^3 (14,000 scf) of compressed hydrogen for use in startup operations;
- Liquid nitrogen dewar (1500-L);
- Air compressor, backup air compressor, and air-storage tank;
- 20-kW backup electric generator;
- 480-V, 208-V, and 120-V electrical circuits.

3.2.3 Natural gas fuel reformer

An autothermal fuel reformer supplied by Precision Combustion, Inc. (PCI, North Haven, CT, USA) is used to convert the natural gas supplied from the municipality into a hydrogen

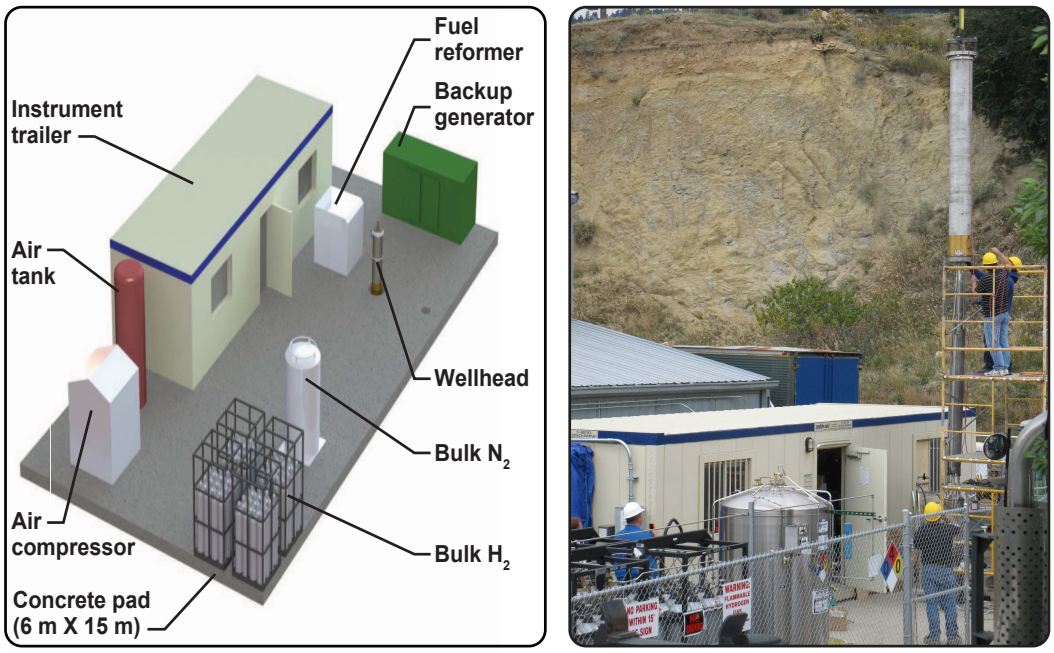

Figure 3.3: Layout of in-ground Geothermic Fuel Cell outdoor test site (left); photograph taken during GFC installation (right).

and carbon-monoxide syngas mixture. In addition to H_2 and CO, the reformate contains water vapor, carbon dioxide, nitrogen, and trace amounts of methane. The syngas generated by the reformer is used to fuel the GFCs.

Autothermal (ATR) reforming combines endothermic steam reforming (SR) and exothermic partial oxidation (POX) to create a near-thermoneutral chemical reaction. The natural gas is combined with air and water vapor oxidizers and passed over a catalyst at elevated temperature (800 °C); the oxygen-to-carbon and steam-to-carbon ratios can be altered to vary the reformate composition [70, 71]. Autothermal reforming reduces the need for an external heat source to drive the chemical reaction. Additionally, the reformer offers favorable start-up and response characteristics [72]. The range of operation for the PCI reformer is:

- 8-36 kW_{th} input energy based on the Lower Heating Value (LHV) and flow rate of natural gas;

- Variable oxygen-to-carbon (O/C) molar ratio: $0.8 \leq \mathrm{O/C} \leq 1.2$ based on oxygen present in air supplied to the reformer;
- Constant steam-to-carbon (S/C) molar ratio: $\mathrm{S/C} = 1.0$;
- Supplemental steam addition downstream of the reactor.

The supplemental steam addition enables modification of the reformate steam-to-carbon ratio and lower heating value. Measurement of reformate composition over a range of reformer operating conditions indicates that reformer chemistry is quite close to equilibrium predictions.

3.2.4 Reactive gas preheater

An integrated reactive-gas preheater and heat exchanger is used to heat the reactants upstream of the Geothermic Fuel Cell. An illustration of this preheater is shown in Figure 3.4 A counter-flow tube-in-shell architecture is utilized. This preheater/heat exchanger was designed by Saridea Inspired Engineering, LLC (Denver, CO, USA), and assembled by Deltech, Inc. (Denver, CO, USA).

Cool anode and cathode feed gases entering at the top of the preheat assembly are manifolded to a series of narrow, oval-shaped stainless-steel tubes that form an outer annulus. Heat is transferred to these cool reactants from hot exhaust gases exiting the preheat combustor and the GFC from the bottom. The natural-gas-fueled preheat combustor provides the bulk of the thermal power. A stainless steel inner shield forms the inner annulus of the preheat assembly. Fuel-cell electric power, sensor diagnostics, and combustor gas feeds are plumbed through this inner shield. The shield has fins welded to its outer diameter that extend into the exhaust channel. These fins induce mixing and promote heat transfer from the hot exhaust gases to the heat-exchanger tubing and cool reactant gases.

The burner operating conditions span:

- 8.3-16 kW_{th} input energy based on the LHV and flow rate of natural gas;

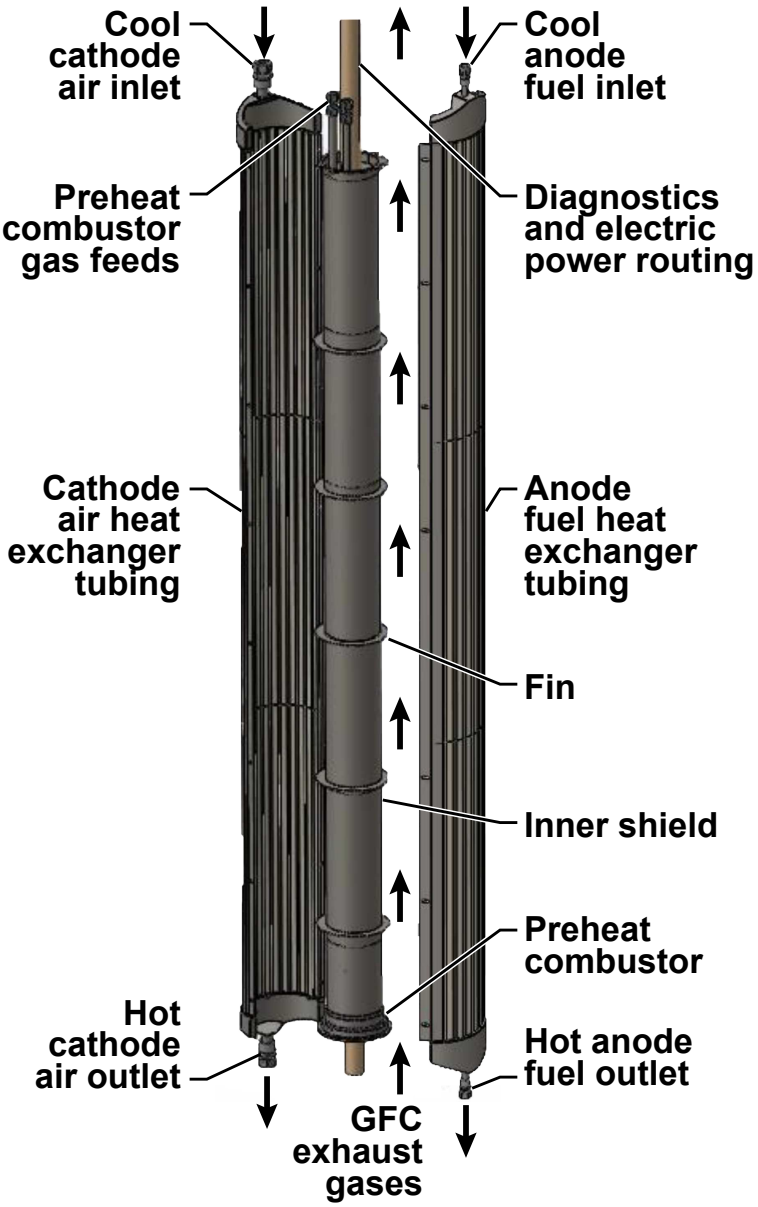

Figure 3.4: Saridea preheater/heat-exchanger assembly.

- Fuel flow rate 0.20-0.68 g s^{-1};
- Air flow rate 5.5-17.6 g s^{-1}.

The preheater assembly is packaged within a stainless-steel housing (not shown) that is coupled to the top of the GFC modules within the bore-hole. The preheater is 3 m (10 ft) in length.

3.2.5 Testing description

The Geothermic Fuel Cell system was operated during November and December of 2014. The average air temperature during the $\sim$ 600 hours of operation was 1.1 °C (34 °F), with highs and lows of 17.8 and -7.2 °C (64 and 19 °C), respectively.

During startup, the SOFC stacks are brought to operating temperature using electric-resistance heaters contained within the Geothermic Fuel Cell modules. The electric heaters continuously provided 20 kW of thermal energy into the GFC during this start-up period. During heat up, a non-explosive hydrogen-nitrogen mixture (5% H_2 and 95% N_2) was fed to the nine GFC stacks.

After reaching a minimum stack operating temperature, the fuel composition was switched from the hydrogen-nitrogen mixture to reformate. Reformer performance was confirmed through measurement of reformate composition using a gas chromatograph. The reformate composition was: 23.7% H_2, 10.4% CO, 29% H_2O, 2.4% CO_2, 33.7% N_2, and 0.19% CH_4. This reformate composition was continuously monitored and found to remain constant for the duration of testing.

The Geothermic Fuel Cell was continuously operated under natural gas reformate for $\sim$ 190 hours. During the first 90 hours of reformate operation, the electric current drawn from the GFC was varied between 0 and 90 A. Following this series of intermittent tests, the current draw set to a constant value of 65 A for the remaining 100 hours of operation under reformate. While "steady-state," time-invariant conditions were never achieved, quasi-steady operation was observed over 24 hours of reformate operation at the 65-A condition.

The following section summarizes in-ground GFC system performance over this 24-hour period.

3.3 Results and discussion

A number of state points were explored over the 600 hours of in-ground Geothermic Fuel Cell operation. While this represents an important demonstration for the GFC technology, this time period is relatively brief, comprising less than 2% of the four-year operating duration for which the GFC is designed.

3.3.1 System performance

As expected, the high temperature of the solid-oxide fuel cell stacks and low temperature of the surrounding geology led to high transfer of heat from the GFC to its surroundings. This places higher demands on the GFC for production of heat, rather than generation of electricity. As will be shown, the in-ground GFC was operated under conditions that maximize heat output in order to meet these thermal demands. While this led to considerable geological heating during the 600 hours of operation, the corresponding electricity generation and the resulting electrical efficiency were comparatively modest.

The in-ground GFC was operated at the 65-A condition for 100 hours. The 24 hours of quasi-steady operation at the 65-A condition provide a baseline operating point for GFC performance analysis.

Because of the series/parallel interconnection of the in-ground GFC stacks and modules, the 65 A of current is distributed across the three GFC modules, resulting in an average of 21.7 A per module, and 21.7 A per stack. It is important to note that the electrical architecture of the in-ground GFC is designed for higher-current operation, perhaps as high as 150 A. Therefore, far-higher electricity generation is possible with the in-ground GFC than was demonstrated during this 600-hour test.

Figure 3.5 presents a performance summary for the in-ground Geothermic Fuel Cell at the 65-A condition. The values shown in this table are calculated using 24-hour averages of

the temperatures and mass flow rates measured during operation. The sensible and chemical energies of the gas streams are calculated from the measured temperatures (T) and mass flow rates ($\dot{m}$):

$$\text{Sensible :} \qquad \dot{Q}_s = \sum_i (\dot{m}_i c_{p,i}) \cdot T \tag{3.1}$$

$$\text{Chemical :} \qquad \dot{Q}_{ch} = \sum_i \dot{m}_i \cdot LHV_i \tag{3.2}$$

where i denotes the individual gaseous species contained in each stream and $c_{p,i}$ is the specific heat capacity for species i.

The heat loss from the in-ground assembly to the surroundings ($\dot{Q}_{heat}$) is determined by evaluating the energy balance for a control volume around the components:

$$\left[\dot{Q}_s + \dot{Q}_{ch}\right]_{in} - \left[\dot{Q}_s + \dot{Q}_{ch}\right]_{out} - \dot{W}_{elec} = \dot{Q}_{heat} \tag{3.3}$$

where $\dot{W}_{elec}$ is the electric power generated by the solid-oxide fuel cell stacks.

At the 65-A condition, the complete GFC system was fed with 60.8 kW of chemical power. This chemical power comes from three inputs:

1. Natural gas fed to the fuel reformer;
2. Natural gas fed to the preheater combustor;
3. Supplemental hydrogen added to the reformate stream.

The chemical power was supplemented by 10.8 kW of heat supplied by the GFC's internal electrical-resistance heaters. This supplemental electric heating serves to maintain the target stack temperatures (680 - 820 °C) during operation. An additional 1.7 kW of thermal power is used to preheat the air that feeds the autothermal reformer. The total energy input to the in-ground Geothermic Fuel Cell system is 73.3 kW.

At the 65-A condition, 4.4 kW of electric power was continuously generated by the solid-oxide fuel cell stacks. As stated previously, this power draw is less than one third of the rated capacity of the GFC stacks. Operating conditions yielding higher electric power

Total chemical power into system (kW)	60.8	(Power in NG to reformer) + (Power in NG into preheat combustor) + (Power in supplemental H_2 to GFC)
Total heat into system (kW)	12.5	(Preheating of reactants at ATR) + (GFC internal electric heaters)
Stack electric power (kW)	4.4	(Electric current) * (GFC terminal voltage)
System electrical efficiency (%)	7.2	(Stack electric power) / (Total chemical power into system)
Fuel utilization (%)	25.8	(Moles of H_2 consumed to produce electric current) / (Moles of fuel [H_2 + CO + 3*CH_4] fed to GFC)
GFC heat loss to geology (kW)	18.8	[Total chemical and sensible energy in GFC inlet gases - Total energy in GFC exhaust gases] - GFC electric power
Preheater heat loss to geology (kW)	10.4	[Total (chemical and sensible) energy in the preheater inlet gas streams] - [Total energy in preheater outlet gas streams]
Total heat loss to geology (kW)	29.1	(Heat loss from GFC) + (Heat loss from pre-heat unit)
System heating efficiency (%)	47.8	(Total heat loss to surroundings) / (Total chemical power into system)
Combined heat and power efficiency (%)	55.0	(System electrical efficiency) + (System heating efficiency)
Heat loss per unit length of GFC (kW/m)	3.2	(Heat loss to geology) / (6 m GFC length + 3 m of Pre-Heater length)
Reformer efficiency (%)	75.1	(Chemical power in reformate) / (Chemical power in NG fuel)
Heat exchanger efficiency (%)	65.1	(Heat gained by GFC inlet gases) / [(Heat from NG combustion) + (Heat loss from GFC exhaust streams)]

Figure 3.5: Performance of the in-ground Geothermic Fuel Cell system at the 65-A operating condition.

will be explored as our experience with GFC system operation grows. This results in a modest electrical efficiency of 7.2%. The low efficiency is primarily attributed to the low fuel utilization (25.9%) used for this series of tests.

Thermodynamic analyses reveal that the three Geothermic Fuel Cell modules liberated 18.8 kW of thermal power into the surrounding geology. In addition, the preheat unit drove 10.2 kW into the geology, increasing the total thermal power entering the geology to 29.1 kW. This resulted in a heat flux to the geology of 3.2 kW m^{-1} across the 9-m length of GFC-preheater assembly. This is clearly well above the electric power generated by the stacks, as needed during initial startup conditions. The thermal efficiency for providing heat to the geology was 47.8%; the combined heat-and-power efficiency reached 55.0%.

Figure 3.6 depicts the relative distribution of energy across system outputs. The fraction of energy that represents the electrical power harnessed (4.4 kW) is small relative to the heat lost to the geology (29.1 kW). This is due to the high heating demands placed on the GFC, as opposed to electricity generation, during initial operation. It is expected that as the geology grows warmer, more energy conversion can be directed towards electricity generation rather than heat liberation.

Significant thermal energy is also lost in the hot exhaust gases exiting the GFC-preheat assembly (8.4 kW). Such losses are signficant in this near-surface demonstration, but will decrease as the Geothermic Fuel Cells are installed in deeper geological locations. Inefficiency in the autothermal reformer is also considerable (9.2 kW).

The energy lost due to unreacted reformate gases exiting the GFC is most significant (22.3 kW). While this unused fuel negatively impacts efficiency, the ability to pass reformate through the GFC without conversion is an important design feature, as it provides a measure of turndown in device operation. This enables a decrease in thermal and/or electrical output from the GFCs as the geology grows warmer, preventing overheating.

For this demonstration, the unreacted reformate was simply flared above ground. It is reasonable to consider that the unreacted fuel could be used in a number of ways to improve

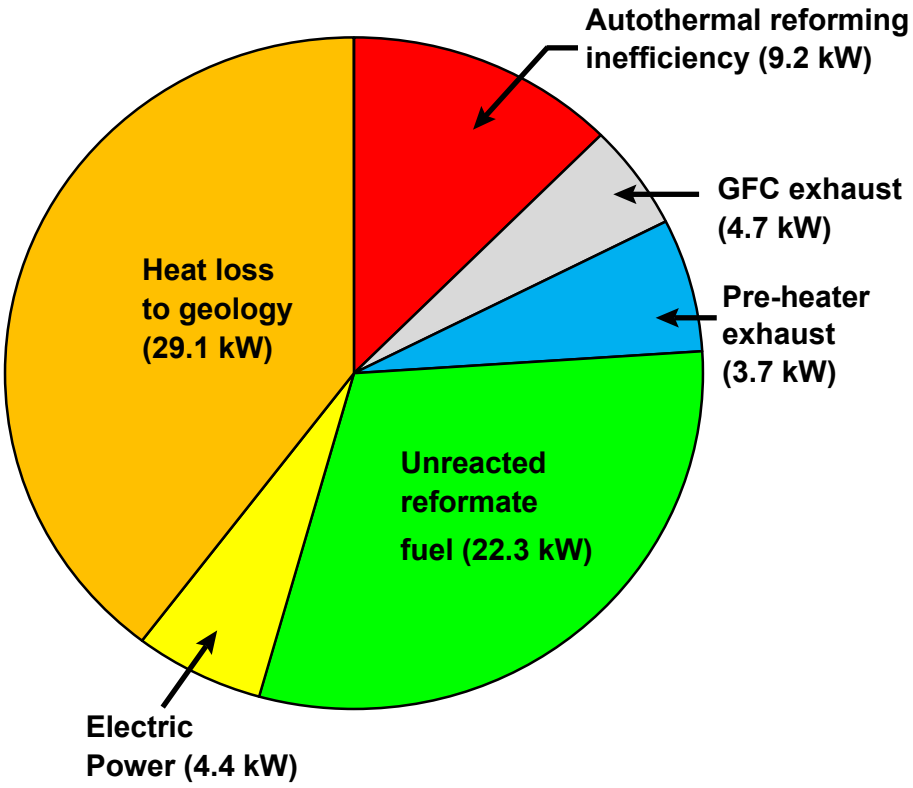

Figure 3.6: Distribution of energy across the Geothermic Fuel Cell system at the 65-A operating point.

system performance. Unreacted reformate gases could be routed to the preheat combustor, reducing (perhaps even eliminating) the consumption of natural gas in this combustor. Thermodynamic calculations indicate that such a change would increase the CHP efficiency from 55.0% to 66.0% for the same conditions tested.

Alternatively, the anode exhaust could be "recycled" into the reformate fuel that feeds the GFC. Anode recycle has been shown to markedly improve system performance [73–75]. This change would necessitate use of a high-temperature anode-recycle blower. Such a blower would need to withstand the high temperatures of the anode exhaust gases (> 200 °C), and require power and control hardware for proper operation [76, 77]. However, these unreacted reformate gases exit the GFC at temperatures that are lower than those found in typical SOFC systems, perhaps reducing the cost of this balance-of-plant component.

3.3.2 Component performance

This section presents the performance of the key components that comprise the Geothermic Fuel Cell System: the fuel reformer, the reactant preheater, and the Geothermic Fuel Cell modules.

The reformer is equipped with an air heater upstream of the reactor, and two "supplemental" steam generators that provide superheated steam to the reformate downstream of the reactor. The supplemental steam is provided in addition to the water that is injected with the air and natural gas into the catalytic reactor body. Operating conditions for the autothermal reformer were held constant throughout the 100 hours of operation at the 65-A condition:

- 36 kW_{th} chemical energy input;
- 1.0×10^{-3} m^3 s^{-1} (60 slpm) natural gas flow rate;
- 3.1×10^{-3} m^3 s^{-1} (183 slpm) air flow rate (1.16 O/C ratio);
- 8.1×10^{-1} g s^{-1} steam flow rate (1.0 S/C ratio);

- 7.1×10^{-1} g s^{-1} supplemental steam flow rate.

As listed previously, the measured reformate composition was very close to chemical-equilibrium predictions, with very little methane slip. The reformer efficiency (Eq.3.4) is evaluated based on the LHVs of the natural gas supply and the hydrogen product [70]:

$$\eta_{ATR} = \frac{(\dot{n}_{H_2} + \dot{n}_{CO}) \cdot LHV_{H_2}}{\dot{n}_{CH_4} \cdot LHV_{CH_4}} = 75.1\% \tag{3.4}$$

This definition assumes complete shifting of the carbon monoxide into CO_2 through the water-gas shift reaction, yielding one mole of H_2 for every mole of CO in the reformate:

$$CO + H_2O \rightarrow H_2 + CO_2.$$

Before the reformed natural gas is fed to the GFC, additional hydrogen (20 slpm) is injected to the fuel stream to increase its chemical power. This supplemental hydrogen is not included in the ATR efficiency calculation.

The flow of energy through the preheater is shown pictorially in Figure 3.7. The preheater is quite effective in increasing reactant-gas temperatures to SOFC-stack operating conditions. The air and reformate gases exit the preheater at 697 and 748 °C, respectively. These temperatures are quite well matched, and near the stack temperatures.

When operating at the 65-A condition, the reactant gases pick up 19.0 kW of thermal power when passing through the preheater. There are two sources of this thermal energy: the high-temperature gases exiting the natural gas combustor, and the hot exhaust gases exiting the GFC modules. The combustor serves the primary heating role: 16.8 kW of thermal power are released through combustion, while 12.6 kW are liberated by the hot exhaust (8.0 kW from the air, 4.6 kW from the anode exhaust).

Much of the heat generated by the combustor and liberated by the GFC exhaust is transferred to the cool reactants (65%). However, heat transferred from the preheater to the surrounding geology is also substantial (10.4 kW).

A similar thermodynamic analysis of the three Geothermic Fuel Cell modules reveals that the GFCs drive 18.7 kW of thermal energy into the surrounding geology. The reactants bring

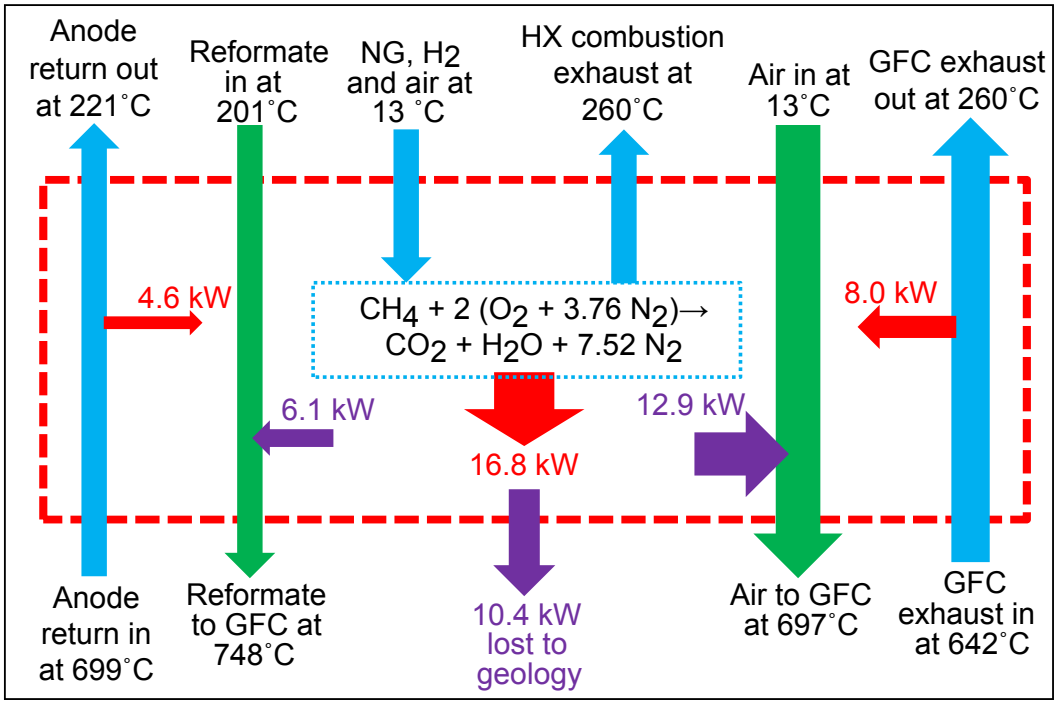

Figure 3.7: Illustration of the heat and gas flows through the preheat assembly. The dashed red line represents the physical boundaries of the preheater. Line thicknesses reflect the magnitude of the heat and gas flows into and out of the preheater.

nearly 52 kW of sensible and chemical energy into the GFC assemblies. The internal electric heaters generate 10.8 kW of heat within the GFC modules. The SOFCs electrochemically convert the chemical energy within the reactants into 4.4 kW of electricity, while 39.6 kW of sensible and chemical energy exit the GFCs through the exhaust. The remainder (18.7 kW) is released to the surrounding geology.

3.3.3 Geology heating

Temperatures in the surrounding geology were periodically measured over the course of the in-ground Geothermic Fuel Cell testing. Figure 3.8a depicts the geology temperature as a function of depth from the surface on two consecutive days of 65-A operation. These measurements were taken within a bore hole located 1.2 m (3.9 ft.) from the GFC casing. A substantial temperature difference is observed with depth below the surface; the highest temperatures are observed at 3.7 m from the surface, nearly adjacent to the top-most stack. The lowest temperatures and highest temperature gradients are found close to the surface.

At depths greater than 4 m, geology temperature gradually decreases with increasing depth into the earth. This reflects the higher volume of geology that must be heated at the bottom of the GFC. Heat transfer in the radial direction is dominant near the middle of the GFC-preheater assembly (depth of 4.5 m); axial heat transfer is also significant at the ends of the assembly. These fairly pronounced end effects result in the lower temperatures at the extreme positions. Overall, the geology temperature is found to increase by over 3 °C in the 24-hour period between the two series of measurements.

Geology temperature as a function of radial position from the GFC casing is shown in Figure 3.8b. This logarithmic temperature profile is consistent with the general solution for one-dimensional radial heat conduction into an infinite homogeneous medium [78]. Such a result may prove valuable for future modeling of the geology-heating process.

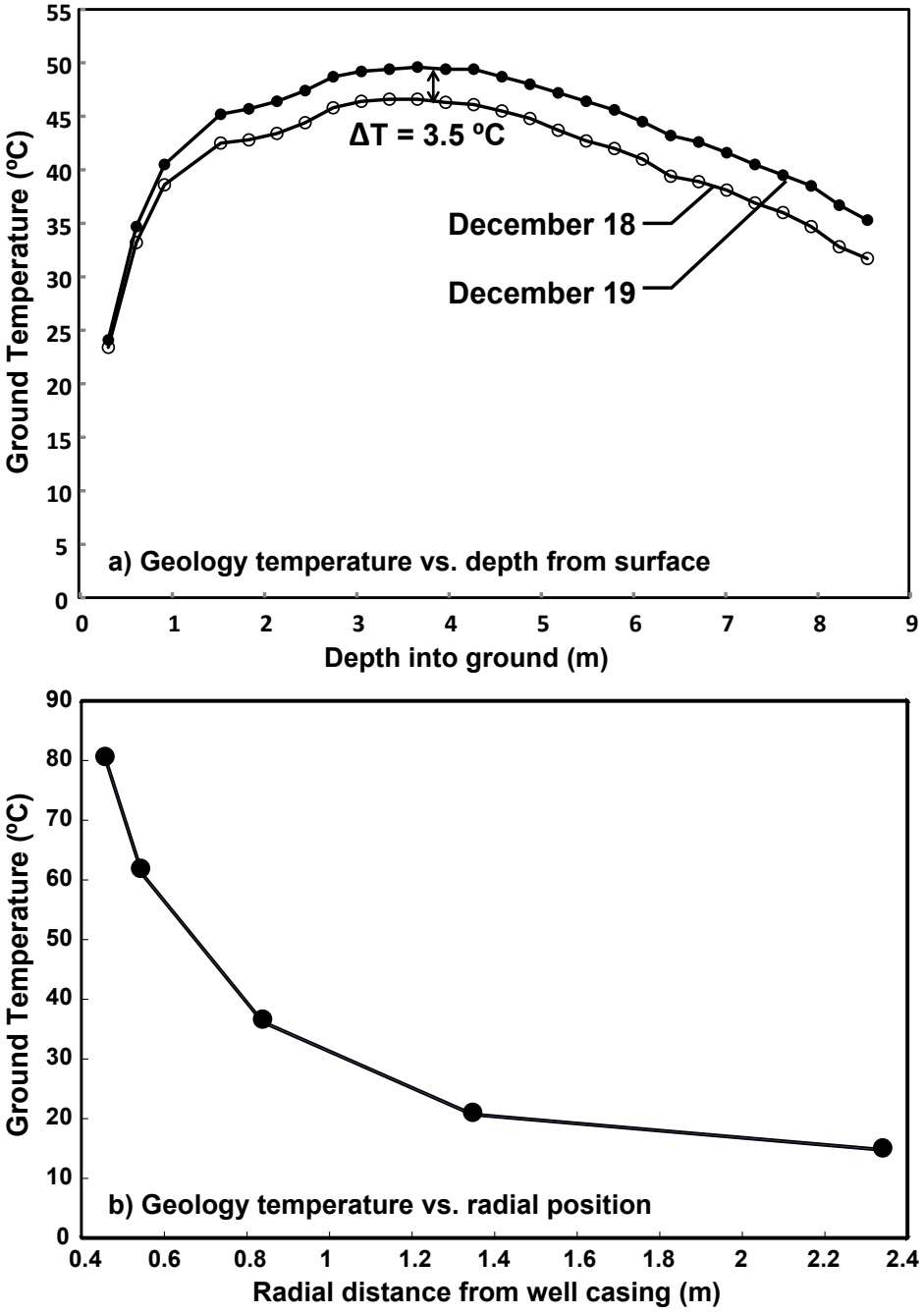

Figure 3.8: Geology temperature: a) as a function of vertical depth from the surface measured on consecutive days of testing; b) as a function of radial distance from the sidewall of the casing in which the Geothermic Fuel Cell assembly is placed. Measurements were taken at a vertical position of 4 m (13 ft.) below the surface.

3.4 Conclusions

This chapter reports on the design and performance of the world's first Geothermic Fuel Cells. Three cylinderical GFC modules, each containing three 1.5 kW*e* solid-oxide fuel cell stacks, were mechanically and electrically coupled and joined to a gas-preheater/heat-exchanger assembly. The 9-m-long assembly was placed within the earth, integrated with extensive balance-of-plant components, controls, and diagnostics, then continuously operated over a period of 600 hours. An initial data set was gathered, and the effectiveness of the GFCs in heating the surrounding geology while simultaneously generating electricity was demonstrated.

In an effort to establish a steady operating point, the Geothermic Fuel Cell system was set at an electrical current output of 65 A while fueled with reformed natural gas. With the SOFC stacks within the GFC assembly operating at temperatures as high as 800 °C, and the surrounding geology at temperatures less than 100 °C, high heat transfer was observed from the GFC assembly to the surroundings. This necessitated a Geothermic Fuel Cell operating condition that favored generation of thermal energy over generation of electricity. Key operating characteristics under this condition include:

- 4.4 kW of continuous electricity generation;
- 29.2 kW of heat transferred from the GFC-preheater assembly to the surrounding geology, with 18.8 kW liberated by the GFCs, and 10.3 kW provided by the preheater;
- 55% combined heat-and-power efficiency;
- 3.2 kW m^{-1} of heat flux transferred to the geology across the 9 m length of the GFC-preheater assembly.

The 22.4 kW of energy loss from the low fuel utilization and ensuing unreacted reformate exiting the GFC is the primary source of the relatively low system electrical efficiency (7.2%).

Considerable performance increases could be realized by harnessing the chemical and thermal energy in the unreacted fuel exiting the GFC.

The use of Geothermic Fuel Cells in unconventional oil-and-gas recovery presents an exciting new application for solid-oxide fuel cell technology. For the present study, the primary resource to be accessed is the four-trillion barrels of oil trapped within U.S. oil-shale reserves. Other potential applications include down-hole steam generation for accessing tight oils and advanced conventional oil recovery.

CHAPTER 4

MODELING AND SIMULATION OF A NOVEL 4.5 KW_e MULTI-STACK SOLID-OXIDE FUEL CELL PROTOTYPE ASSEMBLY FOR COMBINED HEAT AND POWER

This chapter describes a steady-state system model developed in Aspen Plus^{TM} to predict the GFC-stacks electrochemical performance and the heat-rejection from the module. The model development and simulation results outlined herein were submitted and accepted for publication [79].

4.1 Introduction

This chapter presents a steady-state system model that simulates the electrochemical performance and thermal-energy generation of a multi-stack solid-oxide fuel cell assembly. This novel assembly is termed a "Geothermic Fuel Cell" (GFC). As first presented in Sullivan, et al. [60], the GFC concept entails placement of a network of GFC modules within oil-shale formations hundreds of meters below the earth's surface. The high-temperature solid oxide fuel cells contained in the GFC release thermal energy to the surrounding geology, resulting in conversion of the kerogen within the shale into liquid oil and natural gas at $\sim$ 350 °C [1, 9]. Fueled by natural gas, the SOFCs contained in the GFC modules continuously generate electricity that can be used to serve plant processes at the surface or be fed back to the electrical grid.

The high operating temperatures required for SOFCs (700 – 1000 °C), make them suitable for combined heat and power applications when coupled with heat-recovery systems. As shown by Dodds et al. and Elmer et al. [80, 81], SOFC-CHP systems can achieve efficiencies of up to 90%, resulting in a low-CO_2-emitting alternative-power and thermal-energy co-generation technology. Current residential and commercial SOFC-CHP systems are used for electricity production and thermal-energy generation for space heating or domestic hot

water [32, 33]. The primary objective of these systems is electricity generation to meet the building consumer loads; this application results in intermittent part-load operation of the SOFCs and consequently lower efficiencies [80]. These state-of-the-art SOFC-CHP systems generate relatively low-quality heat. Unreacted fuel in the SOFC exhaust is burned within a combustor located downstream of the stack. This high-quality heat is used for reactant-gas processing and preheating. Following reactant heating, the remaining thermal energy available for meeting building space heating or domestic hot water demands is typically of low quality (< 350 °C) [34–36]. Studies show that the variations of the operating conditions and thermal cycling of these SOFC-CHP systems cause an overall increase in the mechanical and electrochemical degradation of the SOFC stacks during prolonged use [82].

In contrast, the Geothermic Fuel Cell technology presents critical improvements to the current state-of-the-art oil-shale processing and SOFC-CHP technologies described above:

- The adverse environmental impacts and high costs of ex situ processing are alleviated by placing the GFC modules directly within the geology and utilizing heat from the SOFCs to upgrade the kerogen in situ;
- The high efficiency and lower CO_2-emissions of SOFC-CHP systems provide a potentially efficient and environmentally sustainable alternative to current in situ shale processing methods that rely on centrally generated power to operate buried resistive heater elements:
  - Brandt et al. estimate life-cycle carbon emissions for SOFC-based in situ oil-shale upgrading processes to be 64% lower than Shell's ICP process and 49% lower than conventional oil [83];
  - Cleveland et al. estimate the GFC energy ratio to be greater than 15:1 [84];
- Unlike most SOFC-CHP applications, the GFC application places higher value on high-grade thermal-energy generation at the expense of electricity generation:

  - The objective of the system is to reject high-grade heat from the GFC assembly at temperatures greater than 500 °C to the surrounding geology;

- The GFC system is continuously operated over a four-year period, with the SOFCs held at a single steady-state condition for months at a time. In this application, there are no load-following or transient-demand constraints that necessitate dynamic-power and thermal-cycling conditions. This extends stack lifetime and consequently reduces system costs.

In this chapter, we present a model of the Geothermic Fuel Cell prototype shown in Figure 4.1a. The module is designed and built by Delphi Powertrain Systems [50–52, 56, 59], and consists of three 1.5 kW_e SOFC stack-and-combustor assemblies packaged within a stainless-steel casing. The stacks are placed in a 1.8 m tall, 0.3 m diameter cylindrical housing and vertically distributed to promote uniform housing surface temperature and heat rejection.

Fuel and air reactants are fed to the stacks in a parallel configuration, and are electrochemically converted into electricity and product gases. Both products and unutilized reactants can mix and burn within a combustor located below each stack. Alternately, the anode exhaust can vent to the atmosphere through "anode-return" plumbing (not shown); mechanical valving is used to regulate anode-return flow. This anode return enhances operational flexibility by reducing thermal-energy generation with only a modest impact to electrochemical performance. Hot product gases exit the combustors and flow upwards through an annular space between two stainless steel housings, rejecting heat to the surroundings before being exhausted above ground.

The experimental testing and performance of this Geothermic Fuel Cell module is described in Anyenya et al. [47], where electrochemical and thermal performance were quantified over a wide range of operating conditions. In this paper, we present a computational model that simulates GFC thermo-electrochemical behavior. The model is validated using experimental data from laboratory testing presented in Anyenya et al. [47]. A thermal-

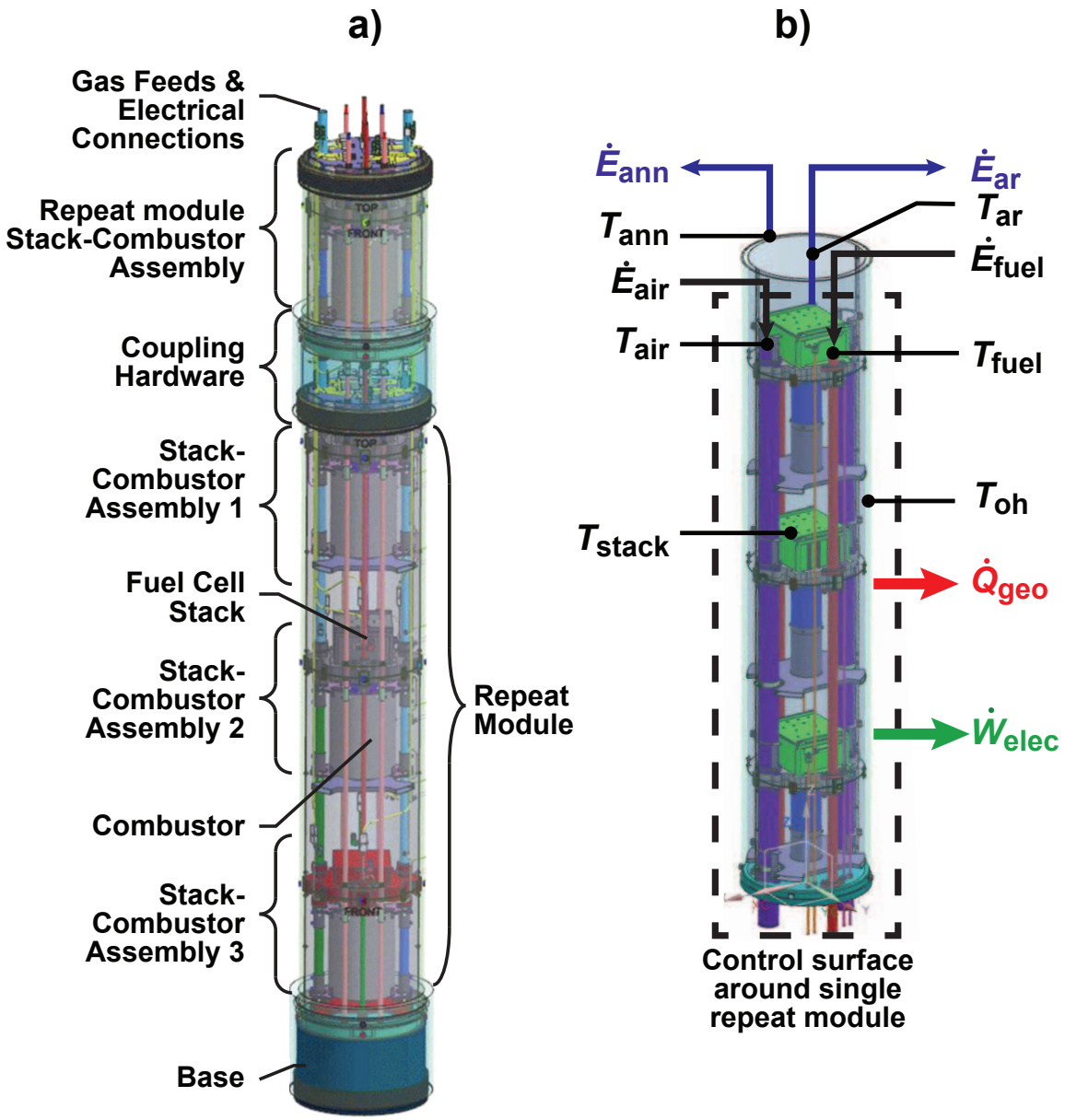

Figure 4.1: a) Schematic of the Geothermic Fuel Cell module. b) Control volume analysis around single 3-stack module and thermocouple locations for temperature measurements used.

resistive network simulates heat rejection from the stack and burner components to the surrounding outer wall. Following validation, the model is exercised over a far-wider range of conditions than could be demonstrated experimentally. The physics underlying the observed experimental performance is presented, and GFC operational characteristics are reviewed.

The novel contributions of this modeling work include:

- The first detailed thermo-electrochemical model of a novel SOFC system architecture that is designed to reject high-temperature / high-quality process heat;
- Model and simulate the thermally integrated design as a means to characterize the stack-combustor units' performance in this application;
- Explore operating conditions that favor thermal energy output to electricity production, contrary to other SOFC-CHP applications.

4.2 Computational model development

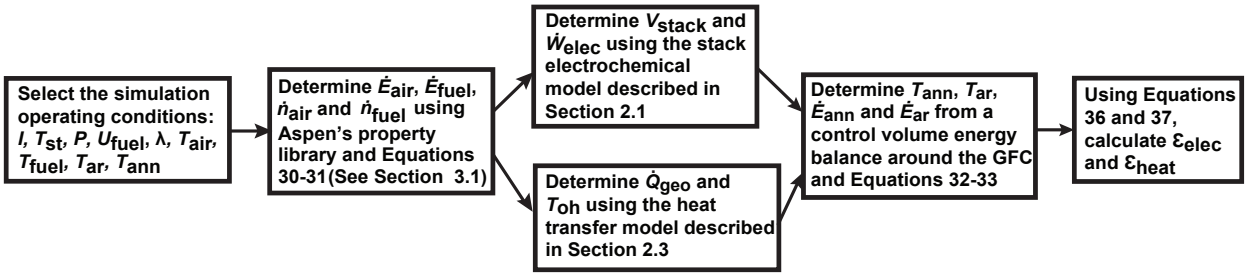

Figure 4.2: Computational flow-chart of the simulation model.

A model of the GFC system is used to capture the gross transport of chemical, thermal and electrical energy through the module. Developed in Aspen Plus^{TM}, the model utilizes mass and energy balances, chemical equilibrium, and reaction kinetics to simulate thermochemical system processes. As shown in Figure 4.2, the GFC operating condition to be simulated is defined by nine input parameters: stack operating current I, stack temperature $T_{\rm st}$, operating pressure P, fuel utilization $U_{\rm fuel}$, stoics of air λ, air inlet temperature $T_{\rm air}$, fuel

inlet temperature T_{fuel} and fuel composition. Using these inputs, the stack voltages and GFC electric power are predicted through an electrochemical model configured as a user-defined subroutine (Section 5.4.19).

The model uses gas stream temperatures, electric current, fuel composition and utilization to predict the required reactant flow rates and the total energy in the inlet streams. The composition of anode and cathode exhaust streams are determined from equilibrium calculations. Energy and mass balances are solved for the chemical, thermal and electrical energy flows into and out of the module as shown in Figure 4.1b. The heat to the surrounding and the temperature of the module's outer housing are predicted by a heat-transfer subroutine descried in Section 4.2.3. Electrochemical and heating performance of the module is calculated from the resulting electric power and heat loss. This model provides insight on the physical phenomena underway during GFC operation, and guidance regarding operating conditions for optimal CHP performance.

4.2.1 Electrochemical model

Following the approach of Trendewicz et al. [27], Leah et al. [85] and Keegan et al. [86], a zero-dimensional computational model simulates the electrochemical performance of an SOFC unit-cell. The single-cell performance is then extrapolated to a full 1.5 kW_e stack by assuming that the stack is comprised of identical repeating unit cells n_{cells} arranged in electrical series

$$V_{\text{stack}} = n_{\text{cells}} \cdot V_{\text{cell}}. \tag{4.1}$$

The model is used to predict the stack voltage V_{stack}, and GFC electric power $\dot{W}_{\text{elec}}$ for a given current I, stack temperature T_{st} and fuel utilization U_{fuel}

$$\dot{W}_{\text{elec}} = n_{\text{stacks}} \cdot V_{\text{stack}} \cdot I. \tag{4.2}$$

The single cell voltage V_{cell} is given as

$$V_{\text{cell}} = V_{\text{ocv}} - \eta_{\text{ohm}} - \eta_{\text{act}} - \eta_{\text{conc,a}} - \eta_{\text{conc,c}} \tag{4.3}$$

with the open-circuit voltage V_{ocv}, the activation losses η_{act}, the ohmic losses η_{ohm}, and the concentration losses $\eta_{\text{conc,a}}$ and $\eta_{\text{conc,c}}$ at the anode and cathode, respectively.

The Nernst potential E_n is a function of the stack temperature T_{st}, the universal gas constant $\bar{R}$, Faraday's constant F, number of electrons transfered in the reaction n, mole fractions of steam $X_{\text{H}_2\text{O}}$, hydrogen X_{H_2} and oxygen X_{O_2} at the stack outlets and the standard electrode potential E°

$$E_n = E^\circ - \frac{\bar{R}T_{\text{st}}}{nF} \ln\left(\frac{X_{\text{H}_2\text{O}}}{X_{\text{H}_2} \cdot \sqrt{X_{\text{O}_2}}}\right). \tag{4.4}$$

The standard electrode potential is calculated using Equation 4.5 as used in Becker et al. [87]

$$E^\circ = 1.2723 - 2.7645 \cdot 10^{-4} \cdot T_{\text{st}}. \tag{4.5}$$

An empirical leakage coefficient θ is used to account for the deviation of the observed open-circuit voltage from the Nernst potential as in Bove et al. [88] and Lisbona et al. [29]

$$V_{\text{ocv}} = E_n \cdot \theta. \tag{4.6}$$

This leakage coefficient was determined from experiments executed on a similar Delphi 1.5 kW_e stack, where $\theta = 0.9827$.

The activation, ohmic and concentration over-potentials are calculated using the "SOFC spreadsheet-based unit-cell model" developed by Pacific Northwest National Laboratories (PNNL) [89]. In this work, the original PNNL model is calibrated using experimental data collected from early generation Delphi SOFC unit-cell tests under H_2/N_2 fuels across a wide range of temperatures. The model predicts ohmic losses through cell components, charge-transfer overpotential at the electrodes, and losses due to diffusion of reactants into and products out of the porous electrodes. The model also takes into account cell parameters such as component thicknesses, porosities and tortuosities. These losses are dependent on the current density i, fuel and air compositions, cell operating temperature T_{st} and pressure P. These inputs are assumed to be homogeneous over a small electrochemically active area.

The activation polarization η_{act} is given by an approximation of the Butler-Volmer equation

$$\eta_{\text{act}} = \left(\frac{\bar{R}T_{\text{st}}}{\alpha F}\right) \sinh^{-1}\left(\frac{i}{2i_{\text{o}}}\right) \tag{4.7}$$

where α is the symmetry factor, F is Faraday's constant. The exchange current density i_o is a function of the pressure-dependent pre-exponential term P_o, the cell temperature T_{st}, the universal gas constant $\bar{R}$ and the activation energy for charge transfer E_{act}

$$i_{\text{o}} = P_o \cdot \exp\left(-\frac{E_{\text{act}}}{\bar{R}T_{\text{st}}}\right). \tag{4.8}$$

The adjustable Butler-Volmer parameters (α, P_o, E_{act}) are calibrated to fit experimental data collected from single-stack electrochemical-performance measurements.

The ohmic polarization η_{ohm} is given by

$$\eta_{\text{ohm}} = i \cdot \mathbb{R} \tag{4.9}$$

where $\mathbb{R}$ is the sum of the charge-transfer resistances of the anode, cathode, electrolyte and interconnect layers

$$\mathbb{R} = \frac{t_{\text{an}}}{\sigma_{\text{an}}} + \frac{t_{\text{cat}}}{\sigma_{\text{cat}}} + \frac{t_{\text{el}}}{\sigma_{\text{el}}} + \frac{t_{\text{ic}}}{\sigma_{\text{ic}}}. \tag{4.10}$$

The electronic conductivity values σ are calculated using the porosity, cell temperature and empirical constants from cell experiments. The thicknesses t_i are obtained from the cell manufacturer (Delphi Powertrain Systems). The formulation above assumes negligible contact resistances, cross-plane charge flow and series connection of resistances, as discussed in Aguiar et al. [25].

The cathode concentration polarization ($\eta_{\text{conc,c}}$) is given by

$$\eta_{\text{conc,c}} = -\frac{\bar{R}T_{\text{st}}}{4F} \ln\left(1 - \frac{i}{i_{\text{O}_2}}\right) \tag{4.11}$$

where i_{O_2} is the oxygen limiting current density

$$i_{\text{O}_2} = \frac{4FPD_{\text{O}_2-\text{N}_2}}{\bar{R}T_{\text{st}}t_{\text{cat}}} \ln\left(\frac{P}{P - P_{\text{O}_2}}\right) \tag{4.12}$$

and is a function of the cathode thickness t_{cat}, effective binary diffusion coefficient between oxygen and nitrogen $D_{O_2-N_2}$, the partial pressure of oxygen in the bulk gas P_{O_2}, the total pressure in the cathode P and the cell operating temperature T_{st}. Similarly, the anode concentration polarization $\eta_{\text{conc,a}}$ is given by

$$\eta_{\text{conc,a}} = -\frac{\bar{R}T_{\text{st}}}{2F}\left[\ln\left(1-\frac{i}{i_{H_2}}\right) - \ln\left(1+\frac{i}{i_{H_2O}}\right)\right] \tag{4.13}$$

where i_{H_2} and i_{H_2O} are the hydrogen and steam limiting current densities, respectively

$$i_{H_2} = \frac{2FP_{H_2}D_{H_2-H_2O}}{\bar{R}T_{\text{st}}t_{\text{an}}} \tag{4.14}$$

$$i_{H_2O} = \frac{2FP_{H_2O}D_{H_2-H_2O}}{\bar{R}T_{\text{st}}t_{\text{an}}}. \tag{4.15}$$

These are functions of the anode thickness t_{an}, effective binary diffusion coefficients of H_2 and H_2O in the anode $D_{H_2-H_2O}$, the partial pressures of hydrogen and steam in the bulk gas of the anode P_{H_2} and P_{H_2O}, and the cell operating temperature T_{st}.

Table 4.1 lists the parameters used in calculating the cell performance through the set of equations above. The anode, electrolyte, cathode and interconnect thicknesses (t_{an}, t_{el}, t_{cat} and t_{ic}, respectively), anode and cathode tortuosities and the anode and cathode porosity are obtained from the cell manufacturer. The average cell temperature (T_{st}), pressure (P) and fuel composition are experimental set points. The resulting values for activation and concentration polarization are within the expected ranges outlined in Mogensen et al. [90] for anode-supported thin-electrolyte SOFCs in the 650-850 °C temperature range.

4.2.2 Calibration and validation of electrochemical model

Figure 4.3 illustrates the model calibration to experimental results of stack voltage and power density as a function of current, while holding reactant flow rates and stack temperature constant (∼740 °C). For these experiments, in-cell fuel utilization ranged from 0-32%. The model-to-experiment comparison at this operating condition resulted in R^2 values of 94.1% and 99.5% for the stack-voltage and power-density curves, respectively.

Table 4.1: Top: Inputs to the electrochemical model, including cell geometry parameters. Middle: Component conductivities derived from the model. Bottom: Tuned parameters fitted to experimental data.

Input parameters	Value	Units
Cell active area	105.75	cm^2
Anode thickness, t_{an}	500	μm
Cathode thickness, t_{cat}	50	μm
Electrolyte thickness, t_{el}	10	μm
Interconnect thickness, t_{ic}	500	μm
Average cell temperature, T_{st}	750	°C
Cell operating pressure, P	1	atm
Fuel composition	48.5% H_2 48.5% N_2 3% H_2O	
Model-determined parameters	**Value**	**Units**
Anode conductivity, σ_{an}	$2.44 \cdot 10^2$	S cm^{-1}
Cathode conductivity, σ_{cat}	6.88	S cm^{-1}
Electrolyte conductivity, σ_{el}	$2.99 \cdot 10^{-2}$	S cm^{-1}
Exchange current density, i_o	0.363	A cm^{-2}
Cathode effective binary diffusion coefficients, $D_{O_2-N_2}$	0.0215	cm^2 s^{-1}
Anode effective binary diffusion coefficients, $D_{H_2-H_2O}$	0.144	cm^2 s^{-1}
Tuned parameters	**Calibrated value**	**Units**
Symmetry factor, α	$S \cdot T_{st} + C$ $S = 1.62 \cdot 10^{-3}$ $C = -1.19$	- K^{-1}
Pre-exponential, P_o	$\exp(L \cdot T_{st} + K)$ $L = -6.54 \cdot 10^{-3}$ $K = 1.975$	A cm^{-2} K^{-1} -
Activation energy, E_{act}	$1.26 \cdot 10^5$	J mol^{-1}

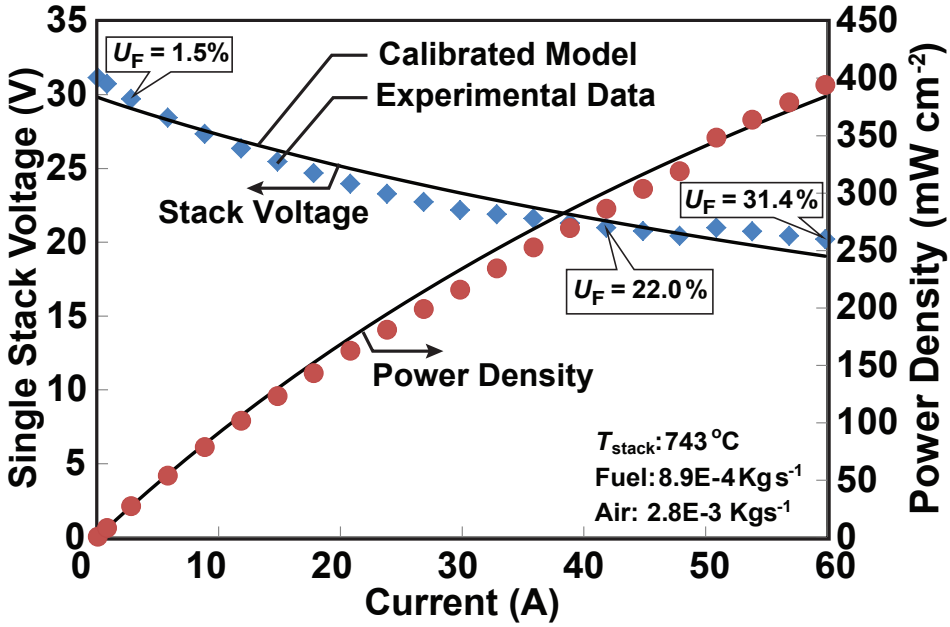

Figure 4.3: Comparison of model-predicted and experimentally measured polarization curves for a 1.5 kW_e stack at 743 °C under 48.5% H_2, 48.5% N_2 and 3% H_2O fuel. Experimental data is shown as symbols, while model results are shown as lines.

This calibrated electrochemical model is then validated through experimental data from GFC-module testing. As the GFC assembly contains three stacks operating at slightly different temperatures, module experimentation creates a wealth of data for model validation. Figure 4.4 shows the comparison between simulation results and experimental stack voltage data at different stack temperatures and electric currents. The top stack (Stack 1, Figure 4.1a) demonstrated the highest temperature, while the bottom stack (Stack 3, Figure 4.1a) was the coolest. Constant fuel utilization of $U_F = 63\%$ was maintained across all conditions shown in Figure 4.4. However, air flow rate was adjusted to maintain stack temperature within constraints. Model predictions match experimental results within an error of 4%. This result shows that the electrochemical model captures the voltage dependence on stack operating temperature and current draw.

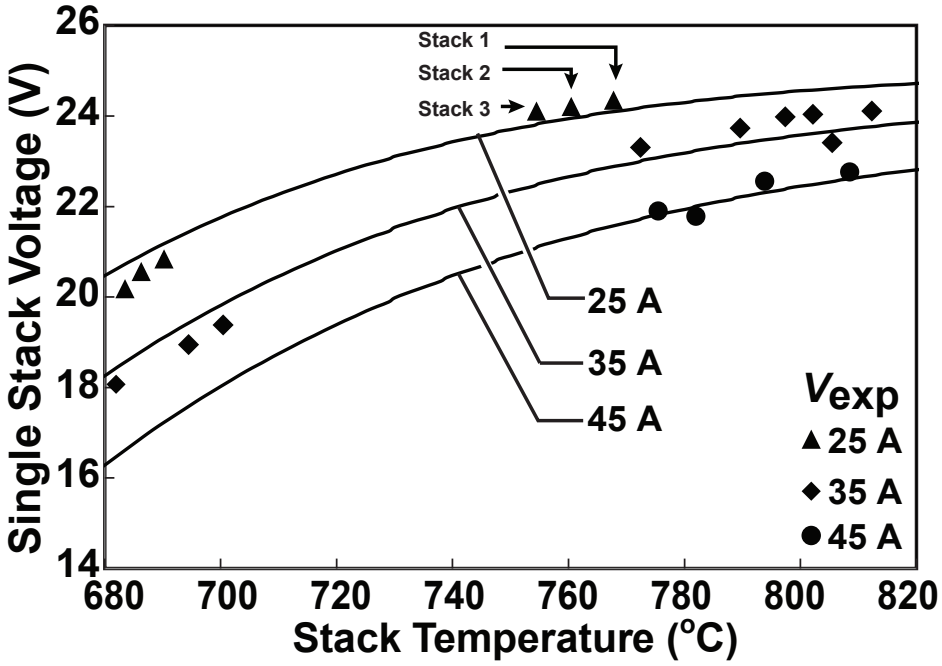

Figure 4.4: Comparison of model-predicted and experimentally measured stack voltage in the GFC module as a function of stack operating temperature and current. Experimental data is shown as symbols, while model results are shown as lines.

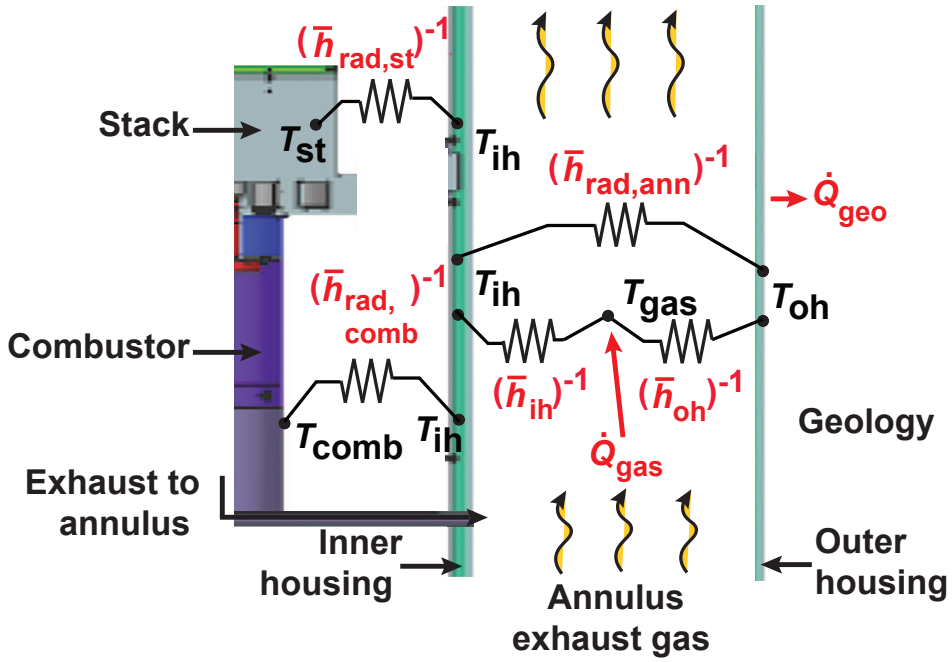

Figure 4.5: Thermal resistive network from the stack-combustor assembly to the GFC's outer wall (not to scale).

4.2.3 Heat-transfer model development

A heat transfer model is used to predict the heat loss from the hot GFC components to the cooler surroundings at steady-state operating conditions. The radial heat loss is calculated using the equivalent thermal circuit for a single stack-combustor assembly shown in Figure 4.5. In this network, heat transfer from the module to the surrounding geology is driven by two mechanisms:

- Radiation heat transfer from the stack, combustor, and inner-housing surfaces;
- Convection heat transfer from the hot exhaust gases to the inner and outer housing;

Uniform/lumped surface temperatures are assumed for each of the components. Given the stack, combustor, and outer-housing temperatures as inputs, the model predicts the heat flux from the module to the surroundings. Values for these inputs are obtained from physical measurements of the GFC module presented in a companion paper.

Several common heat transfer mechanisms are not included in the model. Convective heat transfer within the cavity between the stack-combustor assembly and the inner housing is assumed negligible; no gas is fed through this space, and bouyant-convection heat transfer is generally small in comparison to radiation and forced-convection heat transfer. Conduction heat transfer between GFC components is also assumed negligible. Thermal communication between the stack and the combustor is neglected as physical measurements found the temperature difference between these two components to be below 10 °C. Conduction heat transfer from the gas plumbing to the inner shield is also ignored, as the thickness of the sheet-metal components limits this heat conduction.

There are five thermal resistors shown in Figure 4.5 to simulate the following heat-transfer mechanisms:

1. Radiation from the stack to the inner housing $(\bar{h}_{\mathrm{rad,st}})^{-1}$;
2. Radiation from the combustor to the inner housing $(\bar{h}_{\mathrm{rad,comb}})^{-1}$;

3. Radiation from the inner to the outer housing $(\bar{h}_{\mathrm{rad,ann}})^{-1}$;

4. Convection between the inner housing and hot exhaust gases $(\bar{h}_{\mathrm{ih}})^{-1}$;

5. Convection between the hot exhaust gases and the outer housing $(\bar{h}_{\mathrm{oh}})^{-1}$.

The radiation heat transfer coefficients $\bar{h}_{\mathrm{rad}}$ are calculated using the engineering approximation formula from Nellis et al. [91] and Lai et al. [92]. The radiation heat transfer coefficient between the stack and inner wall, is

$$\bar{h}_{\mathrm{rad,st}} = 4\sigma\varepsilon_{\mathrm{st}}\varepsilon_{\mathrm{ih}}(\bar{T}_1^3) \tag{4.16}$$

where $\varepsilon_{\mathrm{st}}$ and $\varepsilon_{\mathrm{ih}}$ are the stack and inner-housing emissivities, respectively. $\bar{T}_1$ is the film temperature between the stack and inner-housing temperatures, T_{st} and T_{ih}, respectively

$$\bar{T}_1 = \frac{1}{2} \cdot (T_{\mathrm{st}} + T_{\mathrm{ih}}). \tag{4.17}$$

Similarly, the radiation heat transfer coefficient between the combustor and inner-housing is given as

$$\bar{h}_{\mathrm{rad,comb}} = 4\sigma\varepsilon_{\mathrm{comb}}\varepsilon_{\mathrm{ih}}(\bar{T}_2^3) \tag{4.18}$$

where $\varepsilon_{\mathrm{comb}}$ is the combustor emissivity and $\bar{T}_2$ is the film temperature between the combustor T_{comb} and inner-housing temperatures. $\bar{T}_2$ is equal to $\bar{T}_1$ because the combustor temperature is assumed equal to the stack temperature. Finally, the radiation heat transfer coefficient between the inner and outer housing is

$$\bar{h}_{\mathrm{rad,ann}} = 4\sigma\varepsilon_{\mathrm{ih}}\varepsilon_{\mathrm{oh}}(\bar{T}_3^3) \tag{4.19}$$

where $\varepsilon_{\mathrm{oh}}$ is the outer-housing emissivity and $\bar{T}_3$ is the film temperature between the inner and outer T_{oh} housing temperatures

$$\bar{T}_3 = \frac{1}{2} \cdot (T_{\mathrm{ih}} + T_{\mathrm{oh}}). \tag{4.20}$$

Convection heat transfer coefficients are calculated for the inner housing $\bar{h}_{\text{ih}}$, and the outer housing $\bar{h}_{\text{oh}}$

$$\bar{h}_{\text{ih}} = \frac{\overline{\text{Nu}}_{\text{ih}} \cdot k_{\text{air}}}{D_h} \tag{4.21}$$

$$\bar{h}_{\text{oh}} = \frac{\overline{\text{Nu}}_{\text{oh}} \cdot k_{\text{air}}}{D_h} \tag{4.22}$$

where the average Nusselt numbers $\overline{\text{Nu}}_{\text{ih}}$ and $\overline{\text{Nu}}_{\text{oh}}$ are derived for fully developed laminar flow in a circular tube annulus from Table 8.3 in Bergman et al. [93]. The thermal conductivity of the exhaust gas k_{air} is taken to be that of air at the exhaust temperature. The hydraulic diameter D_h is given by

$$D_h = D_{\text{oh}} - D_{\text{ih}}. \tag{4.23}$$

The model assumes $T_{\text{st}} = T_{\text{comb}}$ with negligible loss in model fidelity, resulting in an equivalent heat transfer resistance R_{total}

$$\begin{aligned} R_{\text{total}} = &\left(\bar{h}_{\text{rad,st}} A_{\text{st}} + \bar{h}_{\text{rad,comb}} A_{\text{comb}}\right)^{-1} \\ &+ \left(\bar{h}_{\text{rad,ann}} A_{\text{ih}} + \left[\frac{1}{\bar{h}_{\text{ih}} A_{\text{ih}}} + \frac{1}{\bar{h}_{\text{oh}} A_{\text{oh}}}\right]^{-1}\right)^{-1} \end{aligned} \tag{4.24}$$

where A_{st} and A_{comb} are the total stack and combustor surface areas exposed to the inner housing, respectively. The inner and outer annulus wall surface areas are given by A_{ih} and A_{oh}, respectively.

The heat flow due to the temperature difference between the GFC outer casing and the stack-combustor assembly $\dot{Q}_{\text{st-comb}}$ is given by

$$\dot{Q}_{\text{st-comb}} = \frac{T_{\text{st}} - T_{\text{oh}}}{R_{\text{total}}}. \tag{4.25}$$

A fraction of $\dot{Q}_{\text{st-comb}}$ is the thermal energy convected out of the module via hot exhaust gases in the annular spacing $\dot{Q}_{\text{gas}}$ with the remainder transfered to the geology via the outer housing wall $\dot{Q}_{\text{geo}}$

$$\dot{Q}_{\text{st-comb}} = \dot{Q}_{\text{geo}} + \dot{Q}_{\text{gas}}. \tag{4.26}$$

As discussed in Braun et al. [94], an approximation of $\dot{Q}_{\text{gas}}$ is formulated by assuming equivalence to an empirical fraction β of the net heat flow $\dot{Q}_{\text{st-comb}}$

$$\dot{Q}_{\text{st-comb}} = \dot{Q}_{\text{geo}} + \beta \cdot \dot{Q}_{\text{st-comb}}. \tag{4.27}$$

This results in the heat transfered to the geology via the outer housing wall $\dot{Q}_{\text{geo}}$ being equivalent to

$$\dot{Q}_{\text{geo}} = (1 - \beta) \cdot \left(\frac{T_{\text{st}} - T_{\text{oh}}}{R_{\text{total}}} \right). \tag{4.28}$$

Table 4.2: Heat transfer model parameters and calculated heat transfer coefficient values for different component temperatures and current conditions. [References]

Input parameters	Values			
Stack emissivity, ε_{st}	0.40			
Combustor emissivity, $\varepsilon_{\text{comb}}$	0.58			
Inner wall emissivity, ε_{ih}	0.88 [95]			
Outer wall emissivity, ε_{oh}	0.80 [95]			
Nusselt number,$\overline{\text{Nu}}_{\text{ih}}$	8.66 [93]			
Nusselt number,$\overline{\text{Nu}}_{\text{oh}}$	7.90 [93]			
Physical measurements	Values			Units
Current	30	35	45	A
Fuel flow rate	90.1	105.1	135.2	SLPM
Air flow rate	350	315	357	SLPM
Stoics of air, λ	2.9	2.6	2.3	-
Stack temperature, T_{st}	775	786	794	°C
Inner housing temperature, T_{ih}	633	611	612	°C
Outer housing temperature, T_{oh}	628	592	605	°C
Calculated heat transfer properties	Values			Units
$h_{\text{rad,st}}$	74.9	73.8	74.9	W m^{-2} K^{-1}
$\bar{h}_{\text{rad,comb}}$	109	107	109	W m^{-2} K^{-1}
$\bar{h}_{\text{rad,ann}}$	117	107	109	W m^{-2} K^{-1}
$\bar{h}_{\text{ih}}$	21.3	20.8	21.0	W m^{-2} K^{-1}
$\bar{h}_{\text{oh}}$	19.5	19.0	19.1	W m^{-2} K^{-1}
R_{total}	0.0144	0.0149	0.0147	K W^{-1}
β	0.64	0.61	0.62	-

Component and gas temperatures vary considerably across GFC operating conditions and state points. This leads to changes in the heat-transfer properties described previously.

Table 4.2 presents measurements of component temperatures and electric current at three GFC operational state points, and the associated values of the calculated heat-transfer properties at these state points. Again, the physical measurements of component temperatures and electric current are used as model inputs. The fractional term β is tuned so that $\dot{Q}_{\text{geo}}$ calculated from this heat transfer model is in agreement with heat loss $\dot{Q}_{\text{geo}}$ determined by control-volume energy-conservation calculations. The observed decrease in inner and outer annulus surface temperatures with increasing stack temperature is perhaps counterintuitive. The observed behavior is tied to the increased air utilization. Higher air utilization leads to less stack cooling, and higher stack temperature. The reduced air flow rates at high utilization also lead to decreased convective heat transfer from the hot exhaust gases to the outer housing. This reduces the housing temperature, though the stack temperature climbs. During laboratory testing, reactant gases are preheated in a furnace that was operated at a constant heat rate which resulted in the varying reactant temperatures with changing flow rates. Following the tuning procedure, the R_{total} and β values are found to deviate by only 0.03% and 1.5% across the three state points, respectively. As a result, the values for R_{total}=0.015 and β=0.62 are assumed to be constant.

Table 4.3: Comparison of model-predicted and experimentally measured outer housing temperatures at different operating conditions.

Experimental state point data	1	2	3	4	Units
Current drawn, I	25	30	35	45	A
Fuel flow rate	75.1	90.1	105.1	135.2	SLPM
Air flow rate	350	350	315	375	SLPM
Middle stack temperature, T_{st}	787	800	786	809	°C
Fuel inlet temperature, T_{fuel}	680	684	695	611	°C
Air inlet temperature, T_{air}	700	699	761	611	°C
Annulus exhaust temperature, T_{ann}	694	690	637	602	°C
Anode exhaust temperature, T_{ar}	712	604	665	654	°C
Outer housing temperature, T_{oh}	674	671	590	605	°C
Model-predicted outer housing temperature, T_{oh}	675	657	587	606	°C
% difference	0.1	2.1	0.5	0.2	%

This model is validated by comparing the predicted outer-housing temperature T_{oh} calculated by Equation 4.28 to physical measurements. Table 4.3 shows this comparison across a range of operating currents. It should be noted that in addition to differences in electric-current draw, the four state points shown in Table 4.3 also bear differences in stack temperatures, inlet and outlet gas-stream temperatures, and flow rates. The combined effects of these differences are well captured in the simulations; the model-predicted outer housing temperatures differ from measured values by about 2%, demonstrating close model-to-experiment agreement. This 2% difference is comparable to the measurement error of 1.7% for the Type K thermocouples used in the experiment [96].

Using ground temperature data from in-ground GFC testing presented in Sullivan et al. [60], an empirical equivalent heat transfer resistance R_{geo} from the outer housing wall to the geology is computed. As a result, given GFC stack temperature T_{st} and geology (or ambient) temperature T_{geo}, the expected outer housing temperature T_{oh} when the GFC is placed in the ground, is computed by solving Equation 4.28 and Equation 4.29,

$$T_{\text{oh}} = T_{\text{geo}} + R_{\text{geo}} \cdot \dot{Q}_{\text{geo}}, \tag{4.29}$$

simultaneously.

4.3 Results and discussion

The model is used to simulate the electrochemical performance of the stacks and heat loss from the GFC module at different operating conditions under a hydrogen fuel blend.

4.3.1 Performance evaluation

A "base case" GFC operating condition of 35 A current draw serves for a more-detailed comparison of model predictions to experimental results. Table 4.4 presents the model inputs used to analyze the performance of the three-stack Geothermic Fuel Cell module at a 35 A operating state point.

Table 4.4: Summary of system performance simulation inputs and results at the 35 A operating condition.

Input parameters	Input values		Units
Stack temperature, T_{st}	785		°C
Current drawn, I	35		A
Fuel utilization, U_{F}	63		%
Stoics of air, λ	3		-
Fuel composition	48.5% H_2 48.5% N_2 3% H_2O		
Fuel inlet temperature, T_{fuel}	695		°C
Air inlet temperature, T_{air}	761		°C
Annulus exhaust temperature, T_{ann}	637		°C
Anode exhaust temperature, T_{ar}	665		°C
Control volume energy flows	Calculated values		Units
Total flow of energy in reactant streams, $\dot{E}_{\text{fuel}} + \dot{E}_{\text{air}}$	15.09		kW
Total flow of energy in product streams, $\dot{E}_{\text{ann}} + \dot{E}_{\text{ar}}$	7.51		kW
Chemical energy flow in fuel stream, $\dot{E}_{\text{chem,in}}$	8.45		kW
Chemical energy flow in anode exhaust stream, $\dot{E}_{\text{chem,out}}$	2.13		kW
Radial heat loss, $\dot{Q}_{\text{geo}}$	5.08		kW
Thermal-electrochemical model results	Model	Experiment	Units
Total electric power, $\dot{W}_{\text{elec}}$	2.49	2.42	kW
Outer housing temperature, T_{oh}	584	589	°C
GFC module performance	Values		Units
GFC electrical efficiency, $\mathcal{E}_{\text{elec}}$	41.14		%
GFC Heating efficiency, $\mathcal{E}_{\text{heat}}$	33.67		%

The flow of chemical and sensible energy in the streams are determined from thermodynamic properties at measured gas temperatures and measured flow rates and composition

$$\dot{E}_{\text{fuel}} = \dot{n}_{\text{fuel}} \sum_j X_j \cdot \left(\left[\bar{h}_j(T_{\text{fuel}}) - \bar{h}_j(T_0) \right] + LHV_j \right) \tag{4.30}$$

where $\dot{E}_{\text{fuel}}$ is the sum of the flow of sensible and chemical energy of the preheated fuel stream flowing at temperature T_{fuel} and molar flow rate $\dot{n}_{\text{fuel}}$. $\dot{E}_{\text{air}}$ is the flow of sensible energy of the preheated air stream entering at temperature T_{air} and molar flow rate $\dot{n}_{\text{air}}$

$$\dot{E}_{\text{air}} = \dot{n}_{\text{air}} \sum_j X_j \cdot \left[\bar{h}_j(T_{\text{air}}) - \bar{h}_j(T_0) \right]. \tag{4.31}$$

Energy outputs include the flow of sensible energy in the exhaust products exiting the GFC annulus $\dot{E}_{\text{ann}}$ at temperature T_{ann}

$$\dot{E}_{\text{ann}} = \dot{n}_{\text{ann}} \sum_j X_j \cdot \left[\bar{h}_j(T_{\text{ann}}) - \bar{h}_j(T_0) \right]. \tag{4.32}$$

$\dot{E}_{\text{ar}}$ is the sum of the flow of sensible and chemical energy in the anode return exiting at temperature T_{ar}, molar flow rate $\dot{n}_{\text{ar}}$, and mole fractions $X_{j,\text{ar}}$

$$\dot{E}_{\text{ar}} = \dot{n}_{\text{ar}} \sum_j X_{j,\text{ar}} \cdot \left(\left[\bar{h}_j(T_{\text{ar}}) - \bar{h}_j(T_0) \right] + LHV_j \right). \tag{4.33}$$

The mole fractions, molar enthalpy and lower heating values of each species j in the fuel and air streams are given by X_j, $\bar{h}_j$ and LHV_j, respectively. The sensible energy is defined as the amount of energy that can be harnessed by cooling the hot inlet and outlet gases back to ambient temperature (298 K). This is represented by the difference in species enthalpy at the respective stream temperature (T) and the ambient temperature (T_0), i.e. $[\bar{h}_j(T) - \bar{h}_j(T_0)]$.

The reactant flow rates are determined by the stack fuel utilization (U_{fuel}) and the desired stoics of excess air (λ) constraints

$$\dot{n}_{\text{fuel}} = \frac{\dot{n}_{\text{H}_2,\text{utilized}}}{U_{\text{fuel}} \cdot X_{\text{H}_2}} \tag{4.34}$$

$$\dot{n}_{\text{air}} = \frac{\lambda \cdot \dot{n}_{\text{O}_2,\text{utilized}}}{X_{\text{O}_2}}. \tag{4.35}$$

The total energy into the three-stack assembly is 15.09 kW: 6.64 kW from the sensible energy in the pre-heated inlet gases and 8.45 kW of chemical energy in the fuel mixture. At this 35 A condition, the model predicts 2.49 kW of electric power is continuously generated by the solid oxide fuel cell stacks at 63% fuel utilization and three stoics of air. The GFC module electrical efficiency of 41.14% is calculated as the ratio of electric power output to the chemical energy in the fuel stream

$$\mathcal{E}_{\text{elec}} = \frac{\dot{W}_{\text{elec}}}{\dot{E}_{\text{chem,in}}}. \tag{4.36}$$

The module heating efficiency of 33.67% is based on the flow of chemical and sensible energy contained in the fuel and air inlet streams ($\dot{E}_{\text{fuel}}$ and $\dot{E}_{\text{air}}$)

$$\mathcal{E}_{\text{heat}} = \frac{\dot{Q}_{\text{geo}}}{\dot{E}_{\text{fuel}} + \dot{E}_{\text{air}}}. \tag{4.37}$$

The heat flux to the geology $\dot{Q}_{\text{loss}}$ is the heat transfered via the outer housing wall per unit length of the GFC module

$$\dot{Q}_{\text{loss}} = \frac{\dot{Q}_{\text{geo}}}{\text{GFC length}}. \tag{4.38}$$

Considerable energy (7.51 kW) exits the GFC module in the form of unreacted fuel and hot products. The GFC module liberates 5.08 kW to the surroundings at a wall temperature of 579 °C at this condition. This results in a heat flux of 2.04 kW m^{-1} and a combined heat and power efficiency of 74.8%. The effect of the unconverted chemical energy flow exiting the GFC through the anode return ($\dot{E}_{\text{ar,chem}} = 2.13$ kW) on the GFC module performance is exemplified by the low CHP value at this condition. However, since the linear heat flux value exceeds the 1.6 kW m^{-1} target, activating the stack combustors by closing the anode return would lead to higher heating rates. An increase in module performance could instead be realized by increasing the fuel utilization from the modest 63% at this condition. The high radiation heat transfer coefficients show that this is the dominant mode of heat transfer and could be enhanced by increasing the temperature of the solid components.

4.3.2 Parametric study

An important application of the computational model is to explore how choices of operating conditions can lead to trade-offs in electrochemical and thermal performance. Following calibration and validation of the thermal-electrochemical model, the model is used to simulate the impact of variations in electric current, fuel utilization and stoics of air on GFC-module performance. As noted in Anyenya et al. [47], the Geothermic Fuel Cell was placed within a furnace containing refractory insulation to simulate geology heating within the laboratory setting. The GFC was not subjected to any external heating, as the furnace elements were not activated. When placed within the geology, significant heat will be transported from the module into the surrounding oil shale, resulting in decreased module-surface temperatures.

High-heat-output operating conditions are desirable during down-hole operations (for example, 5.0 kW / m of GFC length). The numerical simulations carried out in this section offer a direct insight into the critical control parameters that ensure that the geology-heating demands are met. The heating requirements for in situ oil shale upgrading vary substantially over the multi-year shale-processing period, as presented in Aouizerate et al. [97]. As geology temperature increases over time, the GFC thermal load drops, and electricity generation becomes more favorable. The objective of this study is to show that the GFC operating window is extensible enough to meet these changing heat demands.

Practical operation and control of a GFC system requires reactant flow and current control, and critical process variable measurements, such as temperature and stack voltage. Table 4.5 displays representative process variables of a GFC system. As described in Ogunnaike et al. [98], the control parameters represent process variables which can be controlled (e.g., through actuation of a valve) by a system operator. The stack operating current is controlled using programmable load banks, while the reactant flow rates are varied using mass flow controllers. Disturbance variables represent temperature inputs for which we do not have active control but which can be measured. For example, the fuel (anode) and air (cathode) inlet temperatures have been shown to vary with reactant flow rates in Table 4.3.

Table 4.5: Process variables of the GFC system employed in the simulations

Inputs	
Control parameters	Measured disturbance variables
Current drawn, I Fuel utilization, U_{F} (or fuel flow rate) Stoics of air, λ (or air flow rate) Fuel composition	Fuel inlet temperature, T_{fuel} Air inlet temperature, T_{air} Geology (or ambient) temperature, T_{geo}
Outputs	
Measured variables	Unmeasured variables
Stack voltage, V_{stack} GFC electric power, $\dot{W}_{\mathrm{elec}}$ Stack temperature, T_{st} Outer housing temperature, T_{oh} Annulus exhaust temperature, T_{ann}	Radial heat flux, $\dot{Q}_{\mathrm{loss}}$ Reactant energy flows, $\dot{E}_{\mathrm{fuel}}, \dot{E}_{\mathrm{air}}$ Exhaust energy flows, $\dot{E}_{\mathrm{ann}}, \dot{E}_{\mathrm{ar}}$

These variables are measured but not controlled. Measured output variables, such as stack temperature, can be verified by direct on-line measurements and can be used for active control purposes. Unmeasured output variables are those which are difficult to measure, but can be calculated, such as heat loss from the system.

In system simulation, control inputs are more flexible in that air and fuel flow rate control can be substituted with specification of (i.e., input) air stoics and fuel utilization, for instance. Measured disturbance variables listed in Table 4.5 are inputted to the model. It is important that the stack temperature remain elevated during in-ground operation whereby the GFC will be losing a significant amount of heat to the surrounding geology. Thus, supplying the SOFC stacks with the highest amount of sensible energy in the reactants is desirable. These considerations have motivated our specification of inlet air (cathode) and fuel (anode) temperatures to values of 761 °C and 695 °C, respectively, for the simulations. These temperatures represent the highest reactant inlet temperatures recorded during GFC testing and are indicative of feasible operating conditions. The stack voltage V_{stack}, and GFC electric power $\dot{W}_{\mathrm{elec}}$ are calculated using the electrochemical model described in Section

5.4.19. The heat loss to the geology $\dot{Q}_{\text{geo}}$ is predicted using Equation 4.28 from the heat-transfer subroutine described in Section 4.2.3.

Under nominal solid-oxide fuel cell system operations, the waste heat is transported out of the stack by the cooling power of the cathode air. These systems assume near adiabatic conditions around the stack as conduction and surface radiation play a minor role, Braun et al. and Lisbona et al. both assign empirical percentage values (3-7%) to these thermal losses [29, 99]. As such, conventional SOFC system models assume the stack temperature is equal to either the cathode inlet, exhaust or average temperature depending on the flow configuration [29, 87, 99, 100]. The unique design and application of the Geothermic Fuel Cell modules result in significant heat loss from the stack via radiative heat transfer to the inner housing. For this reason, the stack temperature in these simulations is estimated by the average of the temperature at the cathode inlet to the module and a calculated adiabatic flame temperature at the middle combustor exit. This modeling approach for estimating SOFC stack temperature is in close agreement with measured values [47] for the operating conditions simulated.

A centrally important operating condition is the choice in electric current draw. As shown in Figure 4.6a, both heat flux and electric power output increase with increasing current. Assuming constant fuel utilization and stoics of air, there is an increase in the mass of reactants being fed to the stacks at higher currents. The power output increases with increasing current as the electrochemical reaction rate is directly proportional to the current. Though the stack voltage decreases by 5.2 volts over the range of current explored, this still results in higher electrical power output at high currents. The observed increase in heat flux to the periphery is credited to the increase in irreversible heat generation within the SOFC stacks at higher currents. The increase in reactant flow rate also generates an increase in the chemical energy of the unutilized fuel exiting the SOFC stack; this fuel is burned in the combustor, releasing yet-more heat.

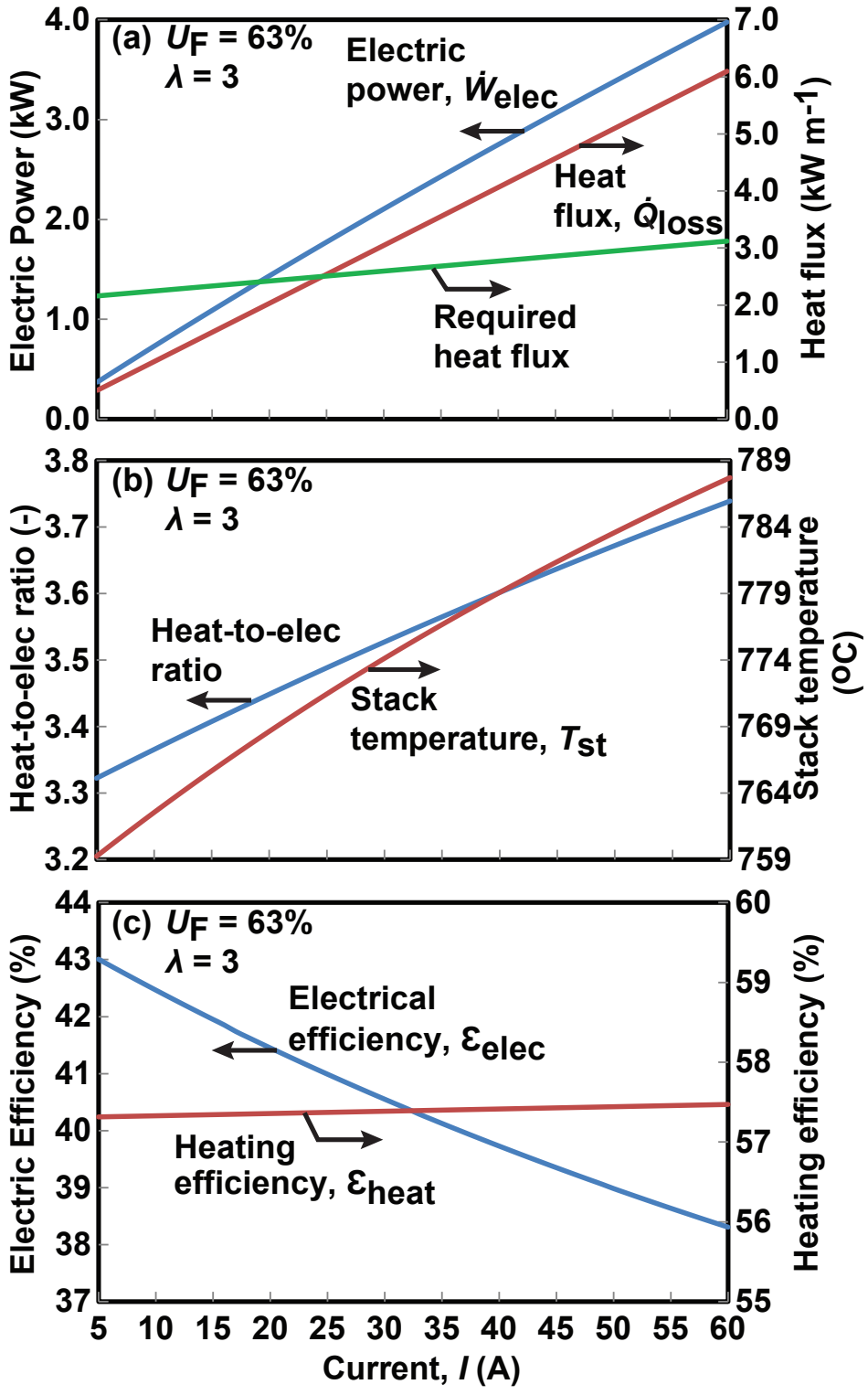

Figure 4.6: Effect of electric current draw on: (a) Electric power and heat flux ((1) Heat flux values expected when the exhaust temperature is set to 500 °C. (2) Simulated heat flux required for the GFC in ambient temperature (20 °C).) (b) Heat-to-electric power ratio and stack temperature (c) Module heating and electrical efficiencies. The fuel utilization and stoics of air are held constant at 63% and 3, respectively.

The heat flux values calculated in this simulation represent the expected heat loss to the periphery given a fixed GFC exhaust temperature of 500 °C. The actual heat flux to the surrounding that is dependent on the temperature difference between the stack and the ambient is also shown in Figure 4.6a. This result shows that for currents under 20 A, the GFC cannot be operated at the given air and fuel utilization factors without running into the risk of quenching. For instance at 10 A, the GFC would have to dispense 5.5 kW of heat to the surrounding which would result in an exhaust stream temperature of -263 °C. As such, the chemical and sensible energy in the reactant streams is not sufficient to meet GFC heat demands at low current conditions when the geology temperature is at a minimum. Consequently, the GFC should be operated at high current conditions during start up.

Another repercussion of the heightened joule heating is a slight increase in the stack temperature by 29 °C (Figure 4.6b). This modest increase translates to a rise in radiative heat flux to the geology. Additionally, the trend in heat-to-electric power ratio shown in Figure 4.6b reveals that the fraction of energy directed towards heating the geology increases substantially with increasing current. During initial start-up when the geology is at very low temperatures (< 150 °C), the heating demands placed on the GFC are far higher than that for electricity generation. In order to keep the SOFC stacks from quenching at these cold-start conditions, a high-heat-flux operating condition is required.

Improved GFC electrical power and heat output does not translate to a significant increase in the GFC heating and electrical efficiencies. As shown in Figure 4.6c, the electric efficiency decreases by 9.0% while the heating efficiency climbs modestly by 0.2% at higher currents. The decreasing electrical efficiency is a result of the drop in stack voltage at high currents caused by higher cell-level ohmic and activation polarization values (Equations 4.7 and 4.9). Despite the increase in heat flux to the geology, the modest increase in heating efficiency is a result of the increase in the total sensible and chemical energy supplied to the control volume from the higher reactant mass flow rates. The sizable drop in GFC electrical efficiency compared to the modest increase in heating efficiency results in an overall drop

in GFC combined heat and power efficiency. This result shows that the stack current draw can be varied to alter the heat flux to the geology, with little to no overall change in GFC performance.

Increasing the fuel utilization at constant current has the reverse effect on the heat and power outputs. As shown in Figure 4.7a, both heat flux and electric power output decrease with increasing fuel utilization. At higher fuel utilization and constant current, there is a decrease in the mass of reactants being fed to the Geothermic Fuel Cell module. The drop in stack voltage at higher fuel utilization leads to a modest decrease in power. The maximum stack voltage is dictated by the Nernst potential calculated by Equation 4.4. Higher utilization leads to increased steam and decreased hydrogen concentrations at the stack outlet that cause a drop in the Nernst potential. The lower reactant flow rates at higher utilization also lead to increased kinetic and mass-transport limitations that also cause a drop in stack voltage. A slight drop in heat flux is observed due to the decreased amount of energy into the control volume; a much-greater fraction of this energy is directed towards electric-power production.

Figure 4.7b shows an increase in the stack temperature as a consequence of the reduced reactant mass flow rates at higher fuel utilization. The amount of heat convected from the stack surface by the flowing reactant gases is reduced at low mass flow rates resulting in an increased risk of stack overheating at these conditions. Figure 4.7b also shows that the fraction of energy directed towards heating the geology decreases slightly with increasing fuel utilization. The heat demand on the GFC module is greatly reduced over the course of operation, once geology temperatures start to exceed 300 °C. By increasing the fuel utilization, the loads on the fuel and air compressors can be reduced due to the lower reactant flow rates, without constraining the amount of heat required. At these low-heat-high-power turn-down conditions, operating at high fuel utilization could potentially result in additional revenue from the surplus electricity production due to the reduced compressor power loads.

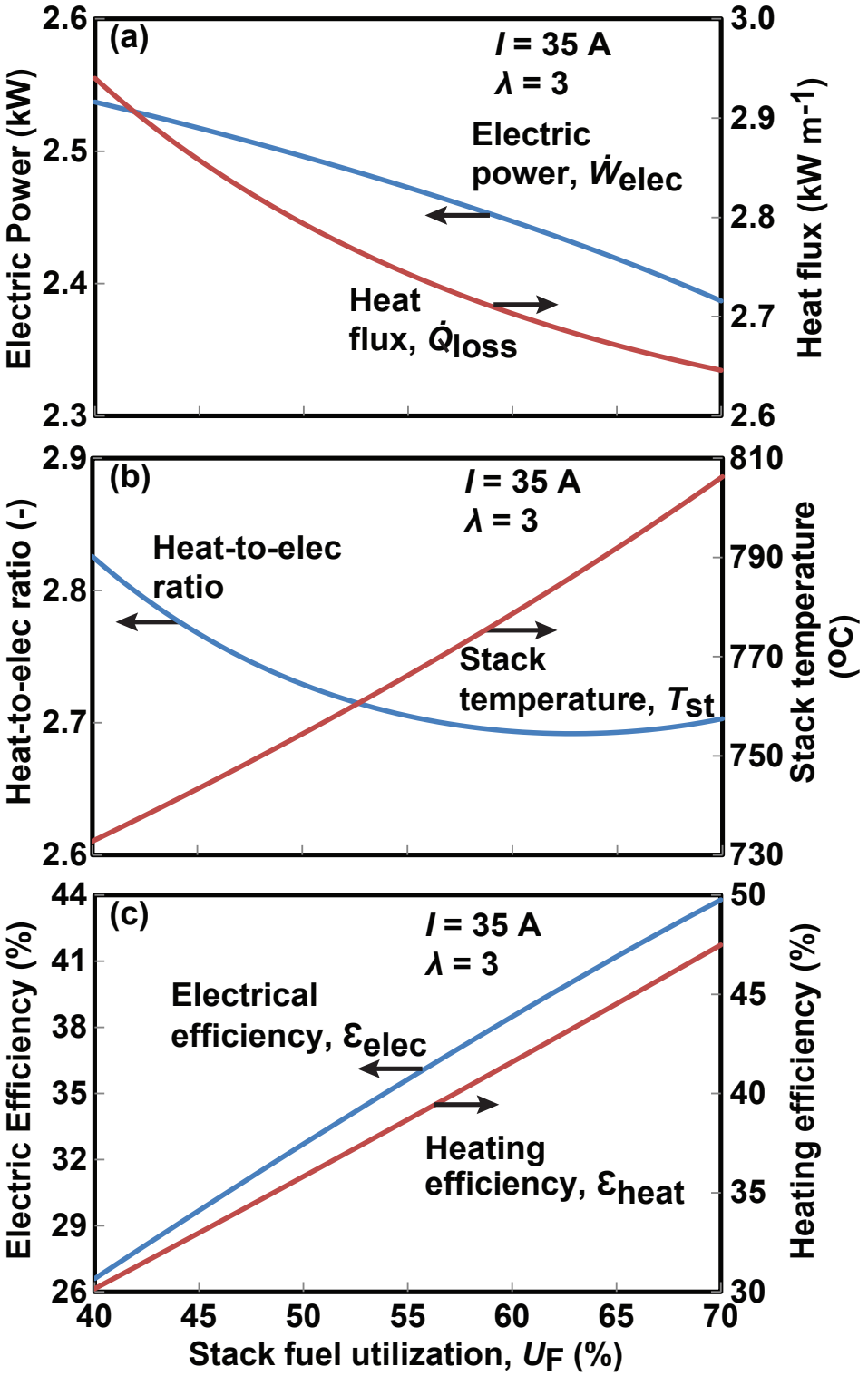

Figure 4.7: Effect of fuel utilization on: (a) Electric power and heat flux (b) Heat-to-electric power ratio and stack temperature (c) Module heating and electrical efficiencies. The current and stoics of air are held constant at 35 A and 3, respectively. The surroundings are at ambient temperature (20 °C).

Varying fuel utilization has the same effect on both electrical and heating efficiency values. The simulation shows a 17% rise in both heating and electrical efficiencies over the range of utilization factors explored. Consequently, maximum combined heat and power efficiency is achieved at high fuel utilization. This result shows that increasing the fuel utilization can be used in improving the system's CHP performance while decreasing the heat flux to the geology during low-heat, high-power turn-down conditions.

Changing the flow rate of air into the system by varying the stoics of air has a modest effect on the GFC electrical performance, as shown in Figure 4.8. Despite the change in flow rate of air into the stack, there is very little fluctuation in the concentration of oxygen in the cathode, resulting in little to no effect on the stack electrochemical performance. As shown in Figure 4.8a, the GFC electric power production is near constant in the range of stoics of air explored. Similarly, Figure 4.8c shows the GFC electrical efficiency also stays constant, as neither the power production nor the amount of chemical energy into the system changes. The rise in heat flux with stoics of air shown in Figure 4.8a is as a result of the increase in sensible energy into the system from the increased air flow rates. This sensible energy increase results in the 12% decrease in heating efficiency as seen in Figure 4.8c.

Contrary to the observations stated above, the flow of excess air is not a trivial operating parameter, as it is used to moderate the temperature of the stack. Figure 4.8b shows a 111 °C drop in stack temperature when the stoics of air is increased from two to five. Raising the flow of excess cooling air will reduce the risk of damage to the stacks from overheating and degradation at high temperatures. By contrast, the analyses presented in Figure 4.6b and Figure 4.7b show that increasing current and fuel utilization both result in high stack temperatures. During field operation, the GFC modules will be buried over 200 m below the ground surface. Consequently, significant energy demands will be placed on the fuel and air compressors. The greatest impact of the excess air flow rate on the system is the electric power required by the air compressor to drive the air down-hole. The increased flow of excess air into the system during operating conditions that require stack cooling will result in high

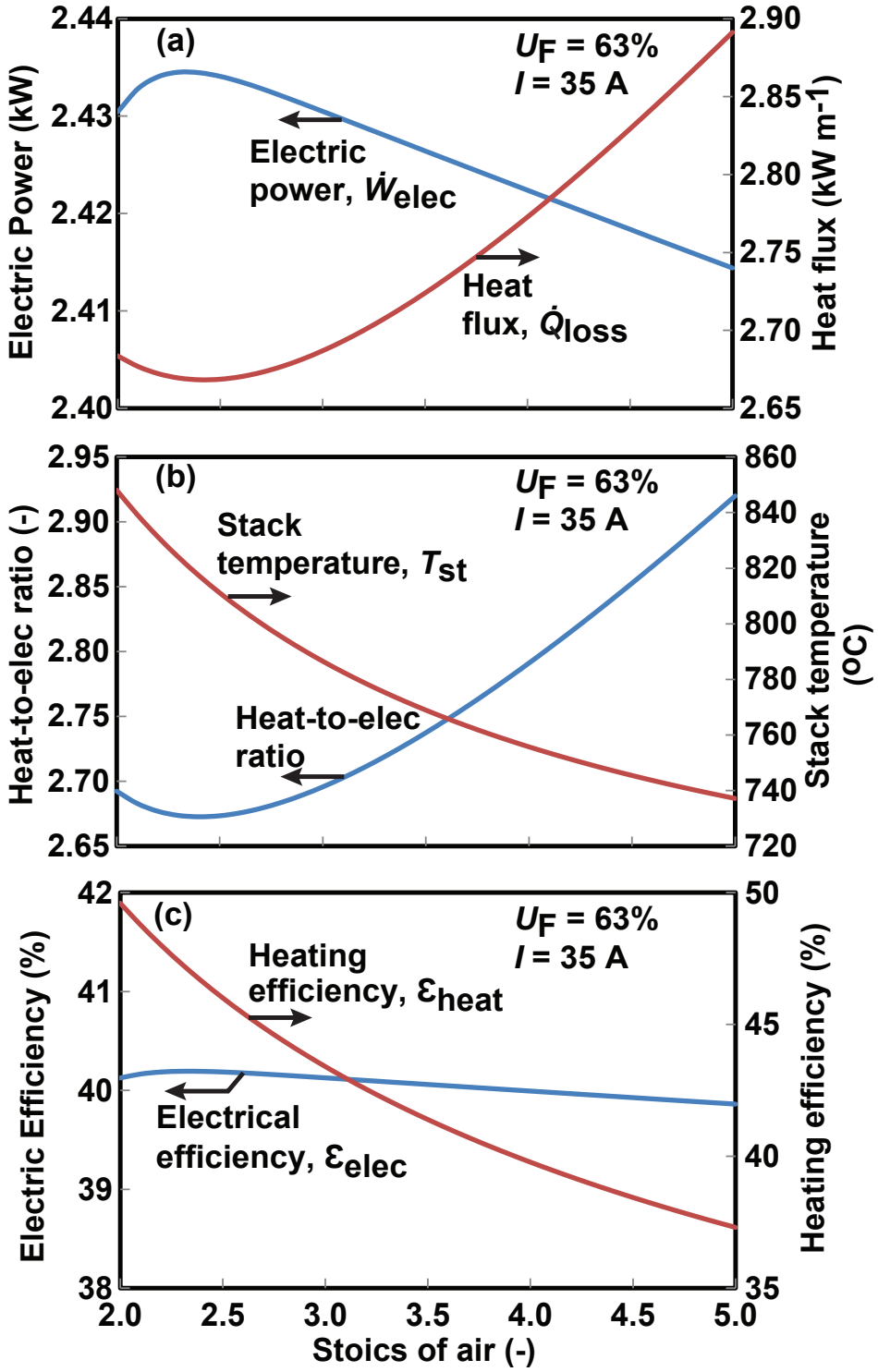

Figure 4.8: Effect of stoics of air on: (a) Electric power and heat flux (b) Heat-to-electric power ratio and stack temperature (c) Module heating and electrical efficiencies. The fuel utilization and current are held constant at 63% and 35 A, respectively. The surroundings are at ambient temperature (20 °C).

compressor electric-power demands. This condition could potentially result in the need for an outside source of electric power to supplement GFC electricity generation.

The simulations carried out above depict GFC heating performance when exposed to ambient temperature conditions (20 °C) as in the laboratory experiment. The model is further exercised to characterize the effect of changing geology temperatures on the GFC heat output as well as the outer housing temperature. As stated above, the flow of excess air is used to moderate the temperature of the stack. In these simulations, the stack temperature is held constant at the nominal 750 °C by varying the stoics of excess air.

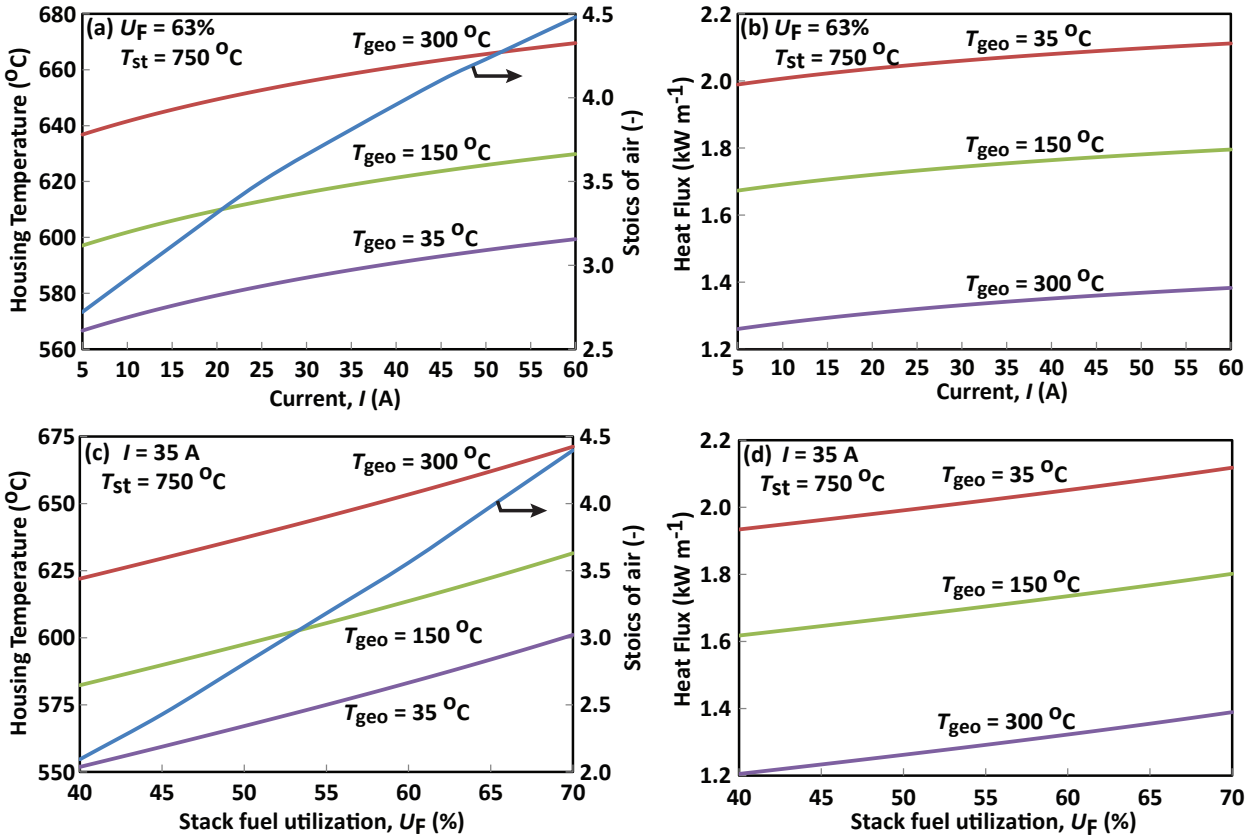

Figure 4.9: Effect of changing geology temperature on the GFC outer housing temperature and heat flux to the geology: (a) and (b) as a function of current, (c) and (d) as a function of fuel utilization. The flow of excess air needed to keep the stack temperature at 750 °C is also shown.

Figure 4.9a and Figure 4.9b show the effect of changing geology temperatures on the GFC outer housing temperature and heat flux, respectively as a function of operating current. Results for three different geology temperatures (35, 150, and 300 °C), which are reflective of different thermal conditions expected in GFC applications throughout its operational life, are shown. The increase in heat flux and surface temperature as a function of current is a result of the increased joule heating and reactant flow rates explained in Figure 4.6 above. The stoics of excess air flow increases with increasing current as more air is required to cool the hotter stacks (see Figure 4.6b) at higher currents. The GFC outer housing temperature increases while the heat flux values decrease with increasing geology temperature. The resulting decrease in the temperature difference between the GFC outer housing and geology causes the observed decrease in heat flux values as the geology temperature rises.

Figure 4.9c and Figure 4.9d show the effect of changing geology temperatures on the GFC outer housing temperature and heat flux, respectively as a function of fuel utilization. Contrary to the observations made in simulations carried out in Figure 4.7 above, the heat flux to the geology increases slightly as a function of fuel utilization in these simulations. This is a result of the increased cooling air flow rates required to maintain the stack temperature at 750 °C for higher fuel utilization factors. The increased flow rates raise the amount of sensible energy introduced to the GFC control volume. Similarly, the resulting decrease in the temperature difference between the GFC outer housing and geology causes the observed decrease in heat flux values as the temperature of the ambient geology increases.

It is also useful to directly observe the relationship between geology temperature and housing temperature and heat flux. Figure 4.10 shows the effect of varying geology temperature on the outer housing temperature and the heat flux to the geology at a single GFC operating condition. The GFC operating current, fuel utilization, stoics of air and stack temperature are specified. As stated above, the flow of excess air is used to moderate the temperature of the stack. In this simulation, the stack temperature is held constant at 750 °C by flowing 3.8 stoics of excess air. As expected, the GFC outer housing temperature

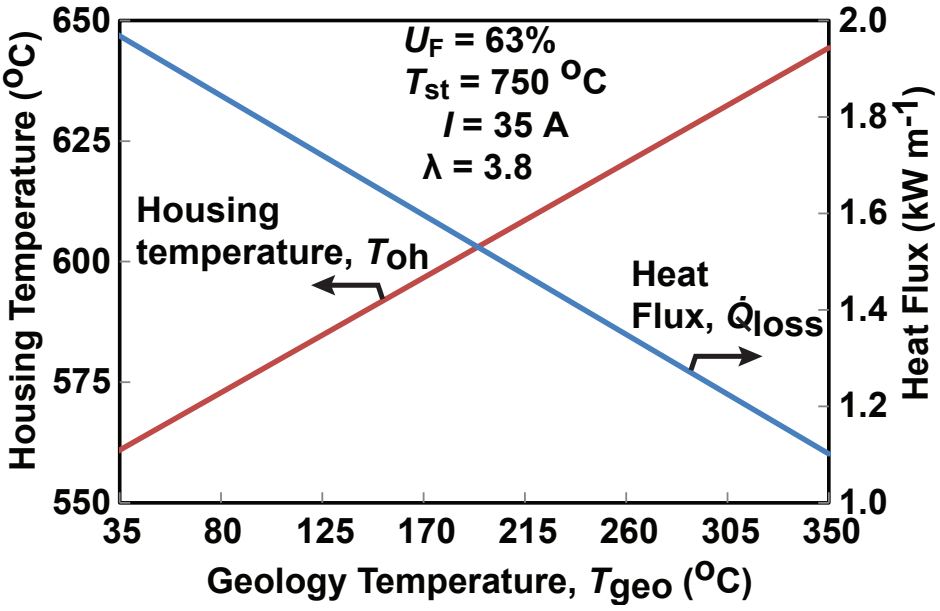

Figure 4.10: Effect of varying geology temperature on the GFC outer housing temperature and heat flux to the geology.

increases by 86 °C with increasing geology temperature. The resulting decrease in the temperature difference between the GFC outer housing and geology causes the observed 0.89 kW m^{-1} decrease in heat flux values at this operating condition.

Since the GFC application targets heat as the more valuable resource over electricity, a high-heat-flux, low-electric-power operating condition is generally desirable. However, in subsequent years of operation, the heat flux (kW m^{-1} value) from the GFC assembly to the geology must be turned down significantly in order to increase the quality of the oil produced. The simulation model and the subsequent parametric study will prove useful in determining ideal operating conditions for start-up, steady-state and turn-down conditions.

4.4 Conclusions

Geothermic Fuel Cell technology entails the harnessing of heat that is generated by high-temperature solid-oxide fuel cells during electricity generation for the liberation of crude oil and natural gas from oil shale. This paper describes a thermal-electrochemical model of a Geothermic Fuel Cell module containing three 1.5 kW$_e$ solid-oxide fuel cell stacks. The

model is used to simulate the electrochemical performance of the stacks and heat loss from the GFC module at different operating conditions under a hydrogen fuel blend. The heat rejection from the GFC module is simulated using a thermal-resistive network from the stack and burner components to the surrounding outer housing. The model is validated against experimental data obtained from laboratory testing of a three-stack GFC module. Simulation results serve as a tool to understanding the system combined-heat-and-power efficiency and for developing strategies for varying the heat flux to the geology during GFC operation.

A parametric study reveals:

- The electric current can be used to increase the module electric power and heat flux while keeping the combined heat and power efficiency of the system nearly constant;
- The fuel utilization can be used to increase system efficiency and to decrease the heat flux to the geology during turn-down conditions;
- The stack temperature can be controlled by varying the flow of excess cooling air. However, increased air flow rates will result in high compressor electric power demands.

The Geothermic Fuel Cell thermal-electrochemical model can be used by in-situ oil-shale developers to simulate a wide range of operating conditions during GFC operation, and inform dispatch of the Geothermic Fuel Cell system in the field. Using the Aspen Plus optimization tool, the current, fuel utilization and stoics of air were varied simultaneously within the ranges explored above. The stack temperature is constrained to values below 800 °C to avoid overheating. The heat flux to the geology is constrained to values above the required average of 1.5 kW m^{-1}. The objective is to maximize the system combined heat and power efficiency. A maximum CHP efficiency of 79.3% is achieved at the following operating conditions: $I = 27.5$ A, $\dot{W}_{\text{elec}} = 1.9$ kW, $\lambda = 3.1$ and $U_{\text{F}} = 70\%$. However, this elementary optimization is strictly energetic in nature and does not consider economical and other operational constraints that will govern the system dispatch. A dispatch optimization

model would require detailed cost equations, and economic and operational constraints with an objective function that seeks to maximize the system heating and electrical efficiency while minimizing costs. Such a model is the subject of future work.

CHAPTER 5

DESIGN AND DISPATCH OPTIMIZATION OF A SOLID-OXIDE FUEL CELL ASSEMBLY FOR UNCONVENTIONAL OIL AND GAS PRODUCTION.

This chapter describes a nonlinear multi-objective optimization model for the design and dispatch of a single GFC heater well. The goal of the model is to appropriately size, configure and operate the GFC system and its auxiliary components at low costs and high thermo-electric efficiencies. The optimization model development and results will be submitted for publication in *Optimization and Engineering*.

5.1 Abstract

This paper presents a multi-objective design and dispatch optimization model of a solid-oxide fuel cell (SOFC) assembly for unconventional oil and gas production. The Geothermic Fuel Cell (GFC) proposes the utilization of heat generated by fuel cells during electricity generation, to provide thermal energy required to pyrolyze kerogen into a mixture of oil, hydrocarbon gas and carbon-rich shale coke. Fuel cells are galvanic cells which chemically convert hydrocarbon-based fuels to electricity. A continuous, non-convex nonlinear programming (NLP) optimization model is formulated in A Mathematical Programming Language (AMPL). The GFC system costs, heating and electrical efficiencies are optimized, subject to geology heating demands, auxiliary component electric power demands and the GFC system performance characteristics. Specifically, we model the maximum length of each heater well, and consequently, the number of solid-oxide fuel cell stacks in each GFC assembly. The dispatch problem varies the fuel-cell operating current, fuel and air utilizations to meet the heat and power-demand constraints at each time period. Solutions to the NLP design and dispatch problems are obtained using KNITRO 10.2.0 solver. A case study shows that the optimal well-head cost of oil and gas produced using the GFC technology is about \$37/bbl

which is comparable to conventional crude oil extraction. The optimal dispatch strategy resulted in a maximum combined-heat-and-power-efficiency of 79%.

5.2 Introduction

Over four trillion barrels of oil are trapped within oil shale formations found in the Piceance Basin of northwestern Colorado, the Uinta Basin of northeastern Utah, and the Greater Green River Basin of southwestern Wyoming as reported by the U.S. Geological Survey [4, 5]. Oil shale is a sedimentary rock that contains organic matter called kerogen, which decomposes into a mixture of oil, hydrocarbon gas and carbon-rich shale coke when heated to approximately 350 °C [8, 9]. Presently, no cost-effective or environmentally sustainable method exists for accessing these vast oil reserves. Ex situ extraction methods entail mining the shale rock from the earth and then retorting it above ground. These processes lead to significant environmental impacts including surface disturbance, large water requirements, and waste management of char and other unwanted materials [11]. In order to mitigate the detrimental environmental impacts of ex situ processing, oil shale processing techniques are being developed in which the formation is heated to retort the oil shale without mining. In situ methods currently being pursued rely on resistive heaters, radio waves and hot gas injection to supply heat to the shale. A significant percentage of the electricity supply for these in situ conversion processes originate from coal-fired power plants that average generation-and-transmission efficiencies near 33%. The use of low efficiency, coal-based electric power for in situ oil extraction results in full-fuel-cycle emissions that are 21 – 47% larger than those from conventionally produced oil [10].

The high operating temperatures required for solid-oxide fuel cell systems (700–1000 °C), make them suitable for combined heat and power applications when coupled with heat-recovery systems. As shown by Dodds et al. and Elmer et al. [80, 81], SOFC-CHP systems can achieve efficiencies of up to 90%, resulting in a low-CO_2-emitting alternative-power and thermal-energy co-generation technology. As first described in Sullivan et al. [60], the "Geothermic Fuel Cell" concept proposes the continuous operation (3–5 years) of SOFCs

placed hundreds of meters below the earth's surface within the oil-shale geology. The thermal energy released during fuel-cell operation is harnessed to heat the surrounding oil shale to temperatures near 350 °C. At these temperatures, the kerogen trapped within the oil shale is retorted to form liquid oil and natural gas. This novel SOFC combined-heat-and-power application in unconventional oil and gas processing presents a cost-effective, environmentally sustainable method of accessing oil shale reserves. Consequently, a large, high-volume market opportunity for SOFCs emerges [47].

Residential and commercial SOFC-CHP systems are used for electricity production and thermal-energy generation for space heating or domestic hot water. Velumani et al. proposes a hybrid-CHP distributed generation system for industrial and commercial scale customers. Solid-oxide fuel cells and a micro gas turbine are combined to generate efficient, reliable and cost-effective electric power while applying the waste heat to local heating or cooling needs [32]. Similar natural gas fueled, SOFC-based systems presented in literature offer a promising electric and thermal energy generation technology for implementation in future commercial buildings [28, 33, 41, 101]. Additionally, SOFCs are also included in most distributed energy systems that combine different renewable and non-renewable energy technologies for power generation [102–104]. These complex combined heat and power systems require elaborate computational tools to determine the optimal configuration, size and operation strategies that meet consumer demands at low-cost and high-efficiency values. For this reason, extensive studies have been carried out to optimize SOFC-CHP system design and operation [105–109].

In this study, we develop a multi-objective design and dispatch optimization model for the Geothermic Fuel Cell assembly. As described in Kuchta et al. [110], optimization models are commonly used to make decisions, represented with decision variables, so as to attain a goal, specified as an objective function, while meeting operational limits, called constraints. The optimization model developed in this work minimizes the cost of a single GFC heater well system and maximizes the heating and electrical efficiencies of the SOFCs, subject to

geology heating demands, auxiliary component electric power demands and the GFC system performance characteristics. This multi-objective approach whereby thermal and economical considerations are analyzed simultaneously is similar to works by Sadeghi et al., Petrescu et al., Pruitt et al. and Sanaye et al. on SOFC and distributed energy systems [111–116].

The objectives of this work is to: (i) optimize the GFC well design such that the maximum volume of oil shale is heated by each heater well; (ii) provide a low-cost-high-efficiency dispatch strategy for the GFC module operation that meets the geology heating demands and auxiliary component electric power demands; (iii) make design recommendations that result in reduced system costs; and (iv) propose ways to improve model performance by reducing solution times and guaranteeing global optimality.

5.2.1 Geothermic Fuel Cell system description

Figure 5.1 shows the composition of a Geothermic Fuel Cell system assembly for a single heater well. The multi-stack solid oxide fuel cell (SOFC) assembly is designed for underground combined-heat-and-power operation. The SOFCs electrochemically convert reformed natural gas fuel into electric power and heat, simultaneously. The heat liberated by the GFC assembly is used to retort oil shale within underground geological formations into high-value crude oil and natural gas. The kerogen beds in which the GFC heaters would be located are buried under approximately 250 m of overburden. As a result, the fuel and air reactants into the GFC heater well have to be supplied at high pressures such that, despite the drop in fluid pressure due to pipe flow frictional losses, the GFC exhaust pressure is still high enough to drive exhaust gases up and out of the well. For this reason, the GFC assembly is comprised of a fuel compressor, an air compressor and a water pump that supply pressurized reactants. An autothermal fuel reformer converts natural gas fuel into syngas ($CO+H_2$) used by the SOFCs. A heat exchanger unit located above the GFC in the overburden section is used to pre-heat the fuel and air into the GFC using hot exhaust gases exiting the heater section. A power conditioning unit is used to convert the DC power produced by the SOFCs into AC power that is then used to provide electric power to the auxiliary components that make up

the system.

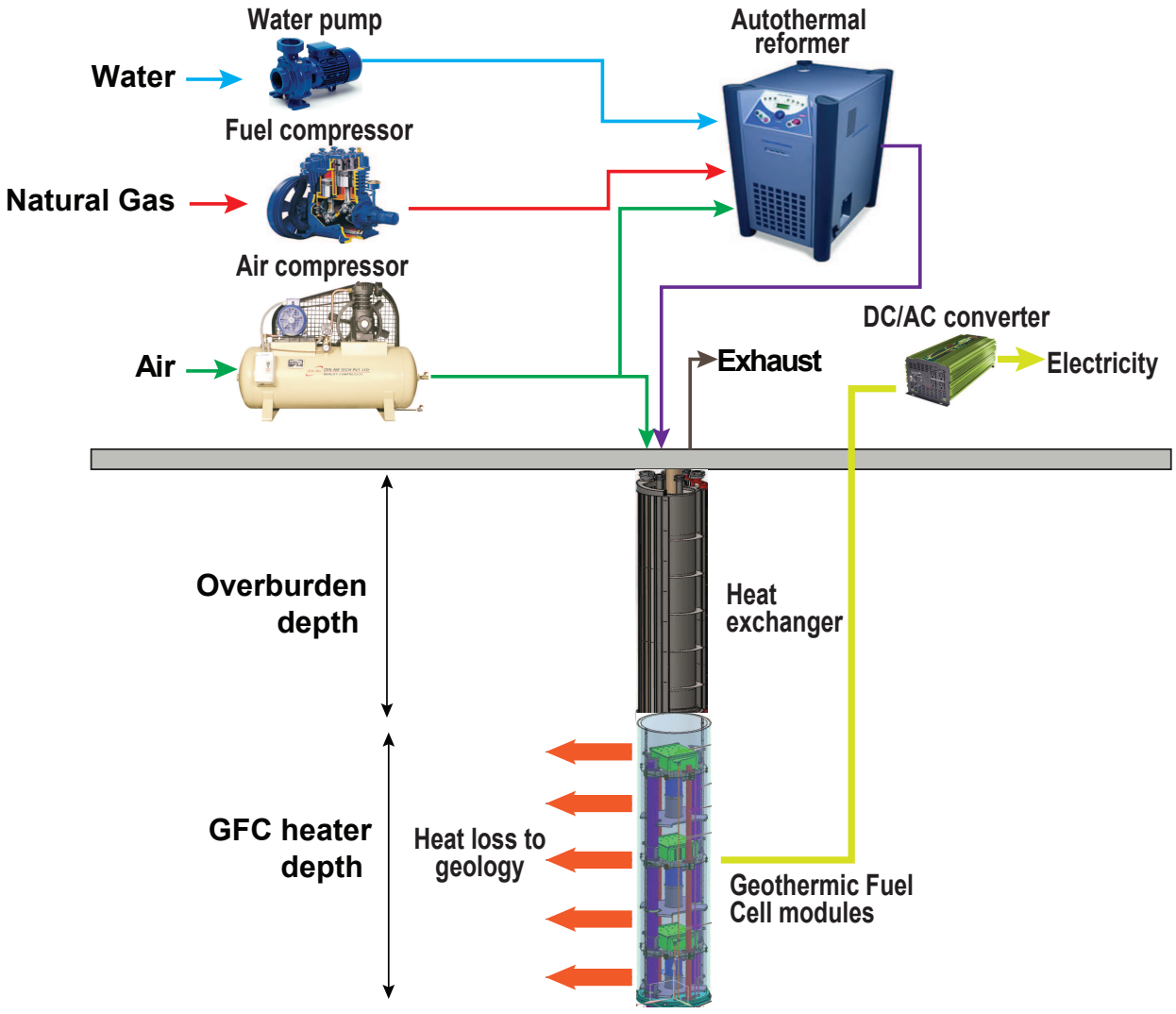

Figure 5.1: System flow diagram showing the components that make up the GFC system and the flows in and out of the control volume.

5.3 Design model formulation

In this section, we present the mathematical formulation of the design problem for the system described in Section 5.2.1. Regular font letters represent parameters and bold font letters represent variables. Superscripts and accents distinguish between parameters and variables that utilize the same base letter, while subscripts identify elements of a set. Some

parameters and variables are only defined for certain set elements listed in the definition. The units of each variable and parameter are also listed in brackets after its definition.

5.3.1 Sets

- $k \in \mathcal{K}$: set of system components

  1. Water pump
  2. Fuel compressor
  3. Air compressor
  4. Natural gas reformer
  5. Heat exchanger
  6. GFC heaters
  7. DC/AC inverter

- $p \in \mathcal{P}$: set of sections of piping and nozzles in the GFC system

  1. Combustor located downstream of the stack
  2. Nozzle entrance to the combustor on the anode side
  3. Nozzle entrance to the combustor on the cathode side
  4. Anode piping in the heat exchanger section
  5. Cathode piping in heat exchanger section
  6. Exhaust through the heat exchanger section
  7. Anode piping in the GFC section
  8. Cathode piping in the GFC section
  9. Exhaust annulus in the GFC section
  10. Nozzle entrance to the stack on the anode side

11. Nozzle entrance to the stack on the cathode side

- $f \in \mathcal{F}$: set of fluid streams in the GFC system

    1. Natural gas flowing into the reformer
    2. Air flowing into the reformer
    3. Water flowing into the reformer
    4. Reformed natural gas fuel flow in the heat exchanger section
    5. GFC air flow in the heat exchanger section
    6. GFC exhaust flow in the heat exchanger section
    7. Reformed natural gas fuel flow in the GFC section
    8. GFC air flow in the GFC section
    9. GFC exhaust flow in the GFC section

- $j \in \mathcal{J}$: set of discrete volumes used to calculate the pressure drop across the GFC section

- $j \in \hat{\mathcal{J}}$: subset of discrete volumes in $\mathcal{J}$ that contain a stack inlet or outlet

5.3.2 Geothermic Fuel Cell (GFC) module and heat exchanger section parameters

$\dot{P}^{\text{GFC}}$ = maximum electric power rating for each SOFC stack in the GFC module [kW]

l^{HX} = heat exchanger section length [m]

l^{mod} = length of each three-stack GFC module [m]

n^{cells} = number of cells per stack [-]

$\bar{I}$ = maximum stack operating current [A]

U^{fuel} = fuel utilization factor [-]

U^{air} = air utilization factor [-]

d_p = hydraulic diameter of each section of pipe $p \in \mathcal{P}$ [m]

w = objective function weighting constant [m kW^{-1}]

5.3.3 Fluid property parameters

ρ_f = density of each fluid stream $f \in \mathcal{F} \mid f = 3, ..., 9$ [kg m^{-3}]

μ_f = dynamic viscosity of each fluid stream $f \in \mathcal{F} \mid f = 4, ..., 9$ [Pa s^{-1}]

k_f = specific heat ratio of air and natural gas at standard conditions $f \in \mathcal{F} \mid f = 1, 2$ [-]

M_f = molar mass of fluid streams $f \in \mathcal{F} \mid f = 1, 2, 4$ [kg mol^{-1}]

Y_f = mass fraction of fluid streams $f \in \mathcal{F} \mid f = 1, 2, 3$ [-]

X^{H_2} = mole fraction of hydrogen in reformed natural gas fuel [-]

X^{CO} = mole fraction of carbon monoxide in reformed natural gas fuel [-]

X^{CH_4} = mole fraction of methane in reformed natural gas fuel [-]

a_1, a_2 = friction factor approximation constants [-]

P^{81}, P^{71} = initial pressure guess at GFC section inlet pipes [Pa]

5.3.4 Physical constants

$\bar{R}$ = universal gas constant [kJ mol^{-1} K^{-1}]

T_o = temperature at standard conditions [K]

P_o = pressure at standard conditions [Pa, kg m^{-1} s^{-2}]

F = Faraday's constant [C mol^{-1}]

$X^{\mathrm{O_2,air}}$ = mole fraction of oxygen in air [-]

5.3.5 Compressor and pump performance parameters

η_k = isentropic efficiency for each component $k \in \mathcal{K} \mid k = 1, 2, 3$

5.3.6 GFC design variables

$\mathbf{L}^{\mathrm{GFC}}$ = GFC section length [m]

$\mathbf{n}^{\mathrm{stacks}}$ = number of SOFC stacks in the GFC section [-]

5.3.7 Compressor performance variables

$\mathbf{P}^{\mathrm{fuel}}$ = total pressure drop of fuel over the length of anode piping in the heat exchanger and GFC heater sections [Pa]

$\mathbf{P}^{\mathrm{air}}$ = total pressure drop of air over the length of cathode piping in the heat exchanger and GFC heater sections [Pa]

$\dot{\mathbf{M}}_f$ = mass flow rate of each fluid stream in the system $f \in \mathcal{F}$ [kg s^{-1}]

$\dot{\mathbf{W}}_k$ = electric power requirement for the compressor and pump components $k \in \mathcal{K} \mid k = 1, 2, 3$ [kW]

$\dot{\mathbf{W}}^{\mathrm{surp}}$ = surplus power required to meet the compressor electric power requirements not met by the GFC stacks [kW]

5.3.8 Pressure drop through heat exchanger and GFC sections variables

$\mathbf{R}_f$ = Reynolds number of each fluid in the heat exchanger section $\forall f \in \mathcal{F} \mid f = 4, 5, 6$ [-]

$\mathbf{f}_f$ = friction factor of each fluid in the heat exchanger section $\forall f \in \mathcal{F} \mid f = 4, 5, 6$ [-]

$\mathbf{P}_p$ = pressure drop through each section of piping in the heat exchanger section $\forall p \in \mathcal{P} \mid p = 4, 5, 6$ [Pa]

$\bar{\mathbf{P}}_{pp'}$ = pressure drop due to tube and nozzle diameter change from section p to p' $\forall p \in \mathcal{P}$ $\forall p' \in \mathcal{P}$ [Pa]

$\hat{\mathbf{R}}_{fj}$ = Reynolds number of each fluid $\forall f \in \mathcal{F} \mid f = 7, 8, 9$ in the GFC section at each discrete volume $j \in \mathcal{J}$ [-]

$\hat{\mathbf{f}}_{fj}$ = friction factor of each fluid $\forall f \in \mathcal{F} \mid f = 7, 8, 9$ in the GFC section at each discrete volume $j \in \mathcal{J}$ [-]

$\hat{\mathbf{P}}_{pj}$ = pressure drop through each section of piping $\forall p \in \mathcal{P} \mid p = 7, 8, 9$ in the GFC section at each discrete volume $j \in \mathcal{J}$ [Pa]

$\hat{\dot{\mathbf{M}}}_{fj}$ = mass flow rate of each fluid $\forall f \in \mathcal{F} \mid f = 7, 8, 9$ into and out of the stacks in the GFC section at each discrete volume $j \in \mathcal{J}$ [kg s^{-1}]

$\mathbf{U}_{fj}$ = velocity of each fluid $\forall f \in \mathcal{F} \mid f = 7, 8, 9$ in the GFC section at each discrete volume $j \in \mathcal{J}$ [m s^{-1}]

$\mathbf{\Delta y}$ = length of each discrete finite volume [m]

5.3.9 Objective function

The design problem objective ($\mathcal{D}$) maximizes the length of the Geothermic Fuel Cell heater section ($\mathbf{L}^{\mathrm{GFC}}$) while minimizing the surplus electric power ($\dot{\mathbf{W}}^{\mathrm{surp}}$) required from an outside source to meet compressor and pump electric power needs. The surplus electric power scaling factor w, is the unit cost of electricity.

$$(\mathcal{D}) \text{ maximize } \mathbf{L}^{\mathrm{GFC}} - w \cdot \dot{\mathbf{W}}^{\mathrm{surp}} \tag{5.1}$$

5.3.10 Design constraints

(**See Section 5.3.11**): Electric power demand constraints.

$$\dot{P}^{\text{GFC}} \cdot \mathbf{n}^{\text{stacks}} + \dot{\mathbf{W}}^{\text{surp}} \geq \sum_{k=1}^{3} \dot{\mathbf{W}}_k \tag{5.2}$$

$$\dot{\mathbf{W}}_1 = \frac{P_o + \mathbf{P}^{\text{fuel}}}{\eta_1} \cdot \frac{\dot{\mathbf{M}}_3}{\rho_3} \tag{5.3a}$$

$$\dot{\mathbf{W}}_2 = \frac{\bar{R} \cdot (T_o)}{M_1} \cdot \left(\frac{k_1}{k_1 - 1}\right) \cdot \left[\frac{P_o + \mathbf{P}^{\text{fuel}}}{P_o}\right]^{\left(\frac{k_1 - 1}{k_1}\right)} \cdot \frac{\dot{\mathbf{M}}_1}{\eta_2} \tag{5.3b}$$

$$\dot{\mathbf{W}}_3 = \frac{\bar{R} \cdot (T_o)}{M_2} \cdot \left(\frac{k_2}{k_2 - 1}\right) \cdot \left[\frac{P_o + \mathbf{P}^{\text{air}}}{P_o}\right]^{\left(\frac{k_2 - 1}{k_2}\right)} \cdot \frac{\dot{\mathbf{M}}_2 + \dot{\mathbf{M}}_5}{\eta_3} \tag{5.3c}$$

(**See Section 5.3.12**): Maximum reactant mass flow rate constraints.

$$\mathbf{n}^{\text{stacks}} = 3 \cdot \frac{\mathbf{L}^{\text{GFC}}}{l^{\text{mod}}} \tag{5.4a}$$

$$\dot{\mathbf{M}}_5 = \left(\frac{\bar{I} \cdot n^{\text{cells}}}{4F}\right) \cdot \left(\frac{M_2}{U^{\text{air}} \cdot X^{\text{O}_2,\text{air}}}\right) \cdot \mathbf{n}^{\text{stacks}} \tag{5.4b}$$

$$\dot{\mathbf{M}}_4 = \left(\frac{\bar{I} \cdot n^{\text{cells}}}{2F}\right) \cdot \left(\frac{M_4}{U^{\text{fuel}} \cdot (X^{\text{H}_2} + X^{\text{CO}} + 4X^{\text{CH}_4})}\right) \cdot \mathbf{n}^{\text{stacks}} \tag{5.4c}$$

$$\dot{\mathbf{M}}_f = Y_f \cdot \dot{\mathbf{M}}_4 \qquad \forall f \in \mathcal{F} \mid f = 1, 2, 3 \tag{5.4d}$$

$$\dot{\mathbf{M}}_7 = \dot{\mathbf{M}}_4 \tag{5.4e}$$

$$\dot{\mathbf{M}}_8 = \dot{\mathbf{M}}_5 \tag{5.4f}$$

$$\dot{\mathbf{M}}_9 = \dot{\mathbf{M}}_6 = \dot{\mathbf{M}}_4 + \dot{\mathbf{M}}_5 \tag{5.4g}$$

(**See Section 5.3.13**): Pressure drop across the heat exchanger section constraints.

$$\mathbf{P}_p = \frac{\mathbf{f}_f}{2} \cdot \frac{l^{\text{HX}}}{d_p \cdot \rho_f} \cdot \left(\frac{\dot{\mathbf{M}}_f}{\frac{\pi}{4}(d_p)^2}\right)^2 \qquad \forall f \in \mathcal{F} \mid f = 4, 5, 6 \qquad \forall p \in \mathcal{P} \mid p = f \tag{5.5a}$$

$$\mathbf{f}_f = a_1 \cdot (\mathbf{R}_f)^{-a_2} \qquad \forall f \in \mathcal{F} \mid f = 4, 5, 6 \qquad \forall p \in \mathcal{P} \mid p = f \tag{5.5b}$$

$$\mathbf{R}_f = \frac{4}{\pi \cdot \mu_f} \cdot \frac{\dot{\mathbf{M}}_f}{d_p} \qquad \forall f \in \mathcal{F} \mid f = 4, 5, 6 \qquad \forall p \in \mathcal{P} \mid p = f \tag{5.5c}$$

(**See Section 5.3.14**): Pressure drop due to pipe diameter change constraints.

Pressure drop due to pipe diameter change from large pipe p to a smaller pipe p'.

$$\bar{\mathbf{P}}_{pp'} = 0.42 \cdot \left(1 - \left[\frac{d_{p'}}{d_p}\right]^2\right) \cdot \frac{1}{2 \cdot \rho_f} \cdot \left(\frac{\dot{\mathbf{M}}_f}{\frac{\pi}{4}(d_{p'})^2}\right)^2 \qquad \forall p, p' \in \mathcal{P} \mid d_p \geq d_{p'} \qquad \forall f \in \mathcal{F} \mid f = p \tag{5.6}$$

Pressure drop due to pipe diameter change from small pipe p to a larger pipe p'.

$$\bar{\mathbf{P}}_{pp'} = \left(1 - \left[\frac{d_p}{d_{p'}}\right]^2\right)^2 \cdot \frac{1}{2 \cdot \rho_f} \cdot \left(\frac{\dot{\mathbf{M}}_f}{\frac{\pi}{4}(d_{p'})^2}\right)^2 \qquad \forall p, p' \in \mathcal{P} \mid d_p \leq d_{p'} \qquad \forall f \in \mathcal{F} \mid f = p \tag{5.7}$$

(**See Section 5.3.15**): Pressure drop across the GFC section constraints.

Anode inlet pipe section pressure drop:

$$0 = \rho_7 \cdot \left[\frac{\mathbf{U}_{7,j+1} - \mathbf{U}_{7j}}{\mathbf{\Delta y}}\right] + \frac{\hat{\dot{\mathbf{M}}}_{7j}}{\frac{\pi}{4} \cdot (d_7)^2 \cdot \mathbf{\Delta y}} \qquad \forall j \in \mathcal{J} \mid j = 1, ..., \mathrm{J}-1 \tag{5.8a}$$

$$0 = \rho_7 \cdot \mathbf{U}_{7j} \cdot \left[\frac{\mathbf{U}_{7,j+1} - \mathbf{U}_{7j}}{\mathbf{\Delta y}}\right] - \frac{\hat{\dot{\mathbf{M}}}_{7j}}{\frac{\pi}{4} \cdot (d_7)^2 \cdot \mathbf{\Delta y}} + \frac{2 \cdot \hat{\mathbf{f}}_{7j} \cdot \rho_7}{d_7} \cdot (\mathbf{U}_{7j})^2 + \left[\frac{\hat{\mathbf{P}}_{7j} - \hat{\mathbf{P}}_{7,j-1}}{\mathbf{\Delta y}}\right] \qquad \forall j \in \mathcal{J} \mid j = 1, ..., \mathrm{J}-1 \tag{5.8b}$$

$$0 = \mathbf{U}_{7\mathrm{J}} \tag{5.8c}$$

$$0 = P^{71} - \hat{\mathbf{P}}_{71} \tag{5.8d}$$

$$\hat{\mathbf{R}}_{7j} = \frac{\rho_7 \cdot d_7}{\mu_7} \cdot \mathbf{U}_{7j} \qquad \forall j \in \mathcal{J} \tag{5.8e}$$

$$\hat{\mathbf{f}}_{7j} = a_1 \cdot (\hat{\mathbf{R}}_{7j})^{-a_2} \qquad \forall j \in \mathcal{J} \tag{5.8f}$$

Cathode inlet pipe section pressure drop:

$$0 = \rho_8 \cdot \left[\frac{\mathbf{U}_{8,j+1} - \mathbf{U}_{8j}}{\mathbf{\Delta y}}\right] + \frac{\hat{\dot{\mathbf{M}}}_{8j}}{\frac{\pi}{4} \cdot (d_8)^2 \cdot \mathbf{\Delta y}} \qquad \forall j \in \mathcal{J} \mid j = 1, ..., \mathrm{J}-1 \tag{5.9a}$$

$$0 = \rho_8 \cdot \mathbf{U}_{8j} \cdot \left[\frac{\mathbf{U}_{8,j+1} - \mathbf{U}_{8j}}{\mathbf{\Delta y}}\right] - \frac{\hat{\dot{\mathbf{M}}}_{8j}}{\frac{\pi}{4} \cdot (d_8)^2 \cdot \mathbf{\Delta y}} + \frac{2 \cdot \hat{\mathbf{f}}_{8j} \cdot \rho_8}{d_8} \cdot (\mathbf{U}_{8j})^2 + \left[\frac{\hat{\mathbf{P}}_{8j} - \hat{\mathbf{P}}_{8,j-1}}{\mathbf{\Delta y}}\right] \qquad \forall j \in \mathcal{J} \mid j = 1, ..., \mathrm{J}-1 \tag{5.9b}$$

$$0 = \mathbf{U}_{8\mathrm{J}} \tag{5.9c}$$

$$0 = P^{81} - \hat{\mathbf{P}}_{81} \tag{5.9d}$$

$$\hat{\mathbf{R}}_{8j} = \frac{\rho_8 \cdot d_8}{\mu_8} \cdot \mathbf{U}_{8j} \qquad \forall j \in \mathcal{J} \tag{5.9e}$$

$$\hat{\mathbf{f}}_{8j} = a_1 \cdot (\hat{\mathbf{R}}_{8j})^{-a_2} \qquad \forall j \in \mathcal{J} \tag{5.9f}$$

Exhaust section pressure drop:

$$0 = \rho_9 \cdot \left[\frac{\mathbf{U}_{9j} - \mathbf{U}_{9,j-1}}{\mathbf{\Delta y}}\right] - \frac{\hat{\dot{\mathbf{M}}}_{9j}}{\frac{\pi}{4} \cdot (d_9)^2 \cdot \mathbf{\Delta y}} \qquad \forall j \in \mathcal{J} \mid j = 2, ..., \mathrm{J} \tag{5.10a}$$

$$0 = \rho_9 \cdot \mathbf{U}_{9j} \cdot \left[\frac{\mathbf{U}_{9j} - \mathbf{U}_{9,j-1}}{\mathbf{\Delta y}}\right] + \frac{\mathbf{U}_{9j} \cdot \hat{\dot{\mathbf{M}}}_{9j}}{\frac{\pi}{4} \cdot (d_9)^2 \cdot \mathbf{\Delta y}} + \frac{2 \cdot \hat{\mathbf{f}}_{9j} \cdot \rho_9}{d_9} \cdot (\mathbf{U}_{9j})^2 + \left[\frac{\hat{\mathbf{P}}_{9,j+1} - \hat{\mathbf{P}}_{9j}}{\mathbf{\Delta y}}\right] \qquad \forall j \in \mathcal{J} \mid j = 1, ..., \mathrm{J}-1 \tag{5.10b}$$

$$0 = \mathbf{U}_{91} \tag{5.10c}$$

$$0 = P_o + \mathbf{P}_6 + \bar{\mathbf{P}}_{96} - \hat{\mathbf{P}}_{9\mathrm{J}} \tag{5.10d}$$

$$\hat{\mathbf{R}}_{9j} = \frac{\rho_9 \cdot d_9}{\mu_9} \cdot \mathbf{U}_{9j} \qquad \forall j \in \mathcal{J} \tag{5.10e}$$

$$\hat{\mathbf{f}}_{9j} = a_1 \cdot (\hat{\mathbf{R}}_{9j})^{-a_2} \qquad \forall j \in \mathcal{J} \tag{5.10f}$$

Mass flow rates through each discrete finite volume:

$$\sum_{j\in\mathcal{J}} \hat{\dot{\mathbf{M}}}_{7j} = \dot{\mathbf{M}}_7 \tag{5.11a}$$

$$\sum_{j\in\mathcal{J}} \hat{\dot{\mathbf{M}}}_{8j} = \dot{\mathbf{M}}_8 \tag{5.11b}$$

$$\hat{\dot{\mathbf{M}}}_{9j} = \hat{\dot{\mathbf{M}}}_{7j} + \hat{\dot{\mathbf{M}}}_{8j} \qquad \forall j \in \hat{\mathcal{J}} \tag{5.11c}$$

$$\hat{\dot{\mathbf{M}}}_{7j}, \hat{\dot{\mathbf{M}}}_{8j}, \hat{\dot{\mathbf{M}}}_{9j} = 0 \qquad \forall j \notin \hat{\mathcal{J}} \tag{5.11d}$$

(**See Section 5.3.16**): Total pressure drop across the whole system constraints:

$$\mathbf{P}^{\text{fuel}} = \mathbf{P}_4 + \bar{\mathbf{P}}_{47} + (\hat{\mathbf{P}}_{71} - \hat{\mathbf{P}}_{7\text{J}}) + \bar{\mathbf{P}}_{7,10} + \bar{\mathbf{P}}_{21} + (\hat{\mathbf{P}}_{91} - \hat{\mathbf{P}}_{9\text{J}}) + \bar{\mathbf{P}}_{96} + \mathbf{P}_6 \tag{5.12a}$$

$$\mathbf{P}^{\text{air}} = \mathbf{P}_5 + \bar{\mathbf{P}}_{58} + (\hat{\mathbf{P}}_{81} - \hat{\mathbf{P}}_{8\text{J}}) + \bar{\mathbf{P}}_{811} + \bar{\mathbf{P}}_{31} + (\hat{\mathbf{P}}_{91} - \hat{\mathbf{P}}_{9\text{J}}) + \bar{\mathbf{P}}_{96} + \mathbf{P}_6 \tag{5.12b}$$

(**See Section 5.3.17**): Non-negativity constraints.

$\mathbf{L}^{\text{GFC}},\ \mathbf{n}^{\text{stacks}},\ \mathbf{P}^{\text{fuel}},\ \mathbf{P}^{\text{air}} \geq 0$

$\dot{\mathbf{W}}^{\text{NGC}}\ ,\ \dot{\mathbf{W}}^{\text{AC}},\ \dot{\mathbf{W}}^{\text{WP}}\ ,\ \dot{\mathbf{W}}^{\text{surp}},\ \boldsymbol{\Delta}\mathbf{y} \geq 0$

$\mathbf{R}_f,\ \mathbf{f}_f,\ \dot{\mathbf{M}}_f,\ \mathbf{P}_p,\ \bar{\mathbf{P}}_{pp'},\ \hat{\mathbf{R}}_{fj},\ \hat{\mathbf{f}}_{fj},\ \hat{\mathbf{P}}_{pj},\ \hat{\dot{\mathbf{M}}}_{fj},\ \mathbf{U}_{fj} \geq 0\ \ \forall f \in \mathcal{F},\ \forall p \in \mathcal{P},\ \forall j \in \mathcal{J}$

5.3.11 Electric power demand constraints

Constraint (5.2) ensures that the electric power demands of the compressors and water pump ($\sum_{k=1}^{3} \dot{\mathbf{W}}_k$) are met by the electric power from the SOFC stacks and surplus power ($\dot{\mathbf{W}}^{\text{surp}}$). The maximum electric power from the GFC system is the product of the stack power rating $\dot{P}^{\text{GFC}}$ and the number of stacks in each well $\mathbf{n}^{\text{stacks}}$. Constraints (5.3a)-(5.3c) calculate the electric power demands of the compressors and water pump which are functions of the fluid mass flow rates $\dot{\mathbf{M}}_f$ and the required reactant supply pressures ($\mathbf{P}^{\text{fuel}}$, $\mathbf{P}^{\text{air}}$). The power requirement for a centrifugal water pump in (5.3a) is taken from White [117]. The expressions used in (5.3b) and (5.3c) to calculate the power required to isentropically compress air and fuel are obtained from Borgnakke and Sonntag [118].

5.3.12 Maximum reactant mass flow rate constraints

Constraint (5.4a) addresses the number of stacks $\mathbf{n}^{\text{stacks}}$ in the GFC as a function of the heater length $\mathbf{L}^{\text{GFC}}$. The length of a single three-stack module is taken from the GFC prototype design presented in Anyenya et. al [47]. The maximum flow rate of air required by the GFC (Constraint (5.4b)) is a function of: (i) The moles of oxygen ions utilized in the electrochemical conversion process by each cell ($\frac{\bar{I}}{4F}$); (ii) the mole fraction of oxygen in air $X^{\text{O}_2,\text{air}}$ to compute the moles of air utilized; (iii) the molar mass of air M_2 to convert the molar flow rate to mass flow rate; (iv) the reciprocal of air the utilization factor U^{air} to compute the total air flow rate per stack. Similarly, the maximum flow rate of reformed fuel required by the GFC (Constraint (5.4c)) is a function of: (i) The moles of hydrogen ions utilized in the electrochemical conversion process by each cell ($\frac{\bar{I}}{2F}$); (ii) the reciprocal of the mole fractions of hydrogen, methane and carbon monoxide in the reformate (X^{H_2}, X^{CH_4}, X^{CO}) to compute the moles of reformate utilized; (iii) the molar mass of the reformed fuel mixture M_4 to convert the molar flow rate to mass flow rate; and (iv) the reciprocal of the fuel utilization factor U^{fuel} to compute the total fuel flow rate per stack. Constraint (5.4d) states that the mass flow rates of reactants flowing into the reformer are the product of the total mass flow rate into and out of the reformer $\dot{\mathbf{M}}_4$, and the mass fraction of each reactant Y_f. Constraints (5.4e)-(5.4g) address the mass-balance requirements for the different fluid streams in the system.

5.3.13 Pressure drop across the heat exchanger section constraints

Constraints (5.5a)-(5.5c) address the pressure drop due to frictional losses in the reactant and exhaust streams flowing through the piping in the heat exchanger section. Constraint (5.5a) states that the pressure drop in each section of pipe is a function of the Darcy friction factor $\mathbf{f}_f$, the pipe length l^{HX} and diameter d_p, the density ρ_f and mass flow rate $\dot{\mathbf{M}}_f$ of the fluid in the pipe. Assuming turbulent flow in the pipes, the Darcy friction factor expression in Constraint (5.5b) is derived from the Haaland approximation in White [117]:

$$\frac{1}{\sqrt{\mathbf{f}_f}} = -1.8 \cdot \log_{10}\left[\frac{6.9}{\mathbf{R}_f} + \left(\frac{\frac{\epsilon}{d_p}}{3.7}\right)^{1.11}\right]$$

which is a function of the Reynolds number, pipe diameter and the pipe surface roughness $\epsilon = 0.000002$ m (stainless steel). The above expression is approximated as a function of simply the Reynolds number $\mathbf{R}_f$ as there is less than a 3% change in the friction factor with changing pipe diameter. Constraint (5.5c) calculates the Reynolds number given mass flow rate, pipe diameter and the dynamic viscosity of the fluid.

5.3.14 Pressure drop due to pipe diameter change constraints

Constraints (5.6) and (5.7) account for the minor losses associated with a change in the size of the pipe. Constraint (5.6) determines the pressure loss due to pipe diameter change from a large pipe p to a smaller pipe p', as a function of fluid mass flow rate $\dot{\mathbf{M}}_f$, fluid density ρ_f, the diameter of the smaller pipe $d_{p'}$ and an empirical approximation of loss coefficient for sudden contraction (SC) from White [117]:

$$K_{\text{SC}} = 0.42 \cdot \left(1 - \left[\frac{d_{p'}}{d_p}\right]^2\right)$$

Constraint (5.7) determines the pressure loss due to pipe diameter change from a small pipe p to a larger pipe p', as a function of fluid mass flow rate $\dot{\mathbf{M}}_f$, fluid density ρ_f, the diameter of the larger pipe $d_{p'}$ and a theoretical loss coefficient for sudden expansion (SE) from White [117]:

$$K_{\text{SE}} = \left(1 - \left[\frac{d_p}{d_{p'}}\right]^2\right)^2$$

5.3.15 Pressure drop across the GFC section constraints

Constraints (5.8a)-(5.10f) address the pressure drop by utilizing Reynold's Transport Theorem and inferring simplifications to the GFC pipe flow. Assuming constant density and viscosity, fully developed plug flow in the pipes, the mass balance equation derived from the general form of the Reynold's Transport Theorem is:

$$\rho_f \cdot \frac{d}{dy}\mathbf{U}_f = -\frac{\hat{\dot{\mathbf{M}}}_f}{\frac{\pi}{4}d_p^2 \cdot \mathbf{\Delta y}}$$

where $\hat{\dot{\mathbf{M}}}_f$ is the mass flow rate of the fluid f leaving or entering the pipe, ρ_f is the density of the fluid f, d_p is the pipe diameter, $\mathbf{\Delta y}$ is the length of each differential control volume and $\frac{d}{dy}\mathbf{U}_f$ is the mean fluid velocity $\mathbf{U}_f$ differential in the direction of flow. Similarly, the momentum balance equation is:

$$\rho_f \cdot \mathbf{U}_f \cdot \frac{d}{dy}\mathbf{U}_f - \mathbf{U}_f \cdot \frac{\hat{\dot{\mathbf{M}}}_f}{\frac{\pi}{4}d_p^2 \cdot \mathbf{\Delta y}} = -\frac{d}{dy}\hat{\mathbf{P}}_p - \rho\mathbf{U}^2 \cdot \frac{2\hat{\mathbf{f}}_f}{d_p}$$

where $\frac{d}{dy}\hat{\mathbf{P}}_p$ is the pressure differential in the direction of flow and $\hat{\mathbf{f}}_f$ is the friction factor. In order to numerically solve the mass- and momentum-balance differential equations, the GFC anode-, cathode- and annulus-pipe sections are discretized using a finite-volume mesh network. Figure 5.2 illustrates the finite-difference discretization stencil for the GFC anode, cathode and annulus pipe sections and the boundary conditions applied in the model.

Constraints (5.8a), (5.9a) and (5.10a) represent the finite-volume difference approximations of the mass-balance equation for each differential volume j. The values of the mass flow rates of fluids into or out of each differential control volume are either positive if the fluid is going into the pipe (as is the case in the exhaust pipe $\hat{\dot{\mathbf{M}}}_{9j}$) or negative if exiting the pipe (as is the case in the anode $\hat{\dot{\mathbf{M}}}_{7j}$ and cathode $\hat{\dot{\mathbf{M}}}_{8j}$ pipes). Similarly Constraints (5.8b), (5.9b) and (5.10b) represent the finite-volume difference approximations of the momentum-balance equation for each differential volume j. Constraints (5.8c), (5.9c) and (5.10c) account for the velocity boundary conditions and Constraints (8d), (9d) and (10d) account for the pressure boundary conditions. Constraints (5.8e), (5.9e) and (5.10e) calculate the Reynolds numbers given the mean fluid velocity, density, pipe diameter and the dynamic viscosity of the fluid in each differential volume j. Constraints (5.8f), (5.9f) and (5.10f) calculate the friction factors of the fluid in each differential volume j using the approximation formula introduced in Section 5.3.13. Constraints (5.11a)-(5.11c) address the mass balance requirements for the different pipe sections. Constraint (5.11d) dictates that at each differential volume $j \notin \hat{\mathcal{J}}$,

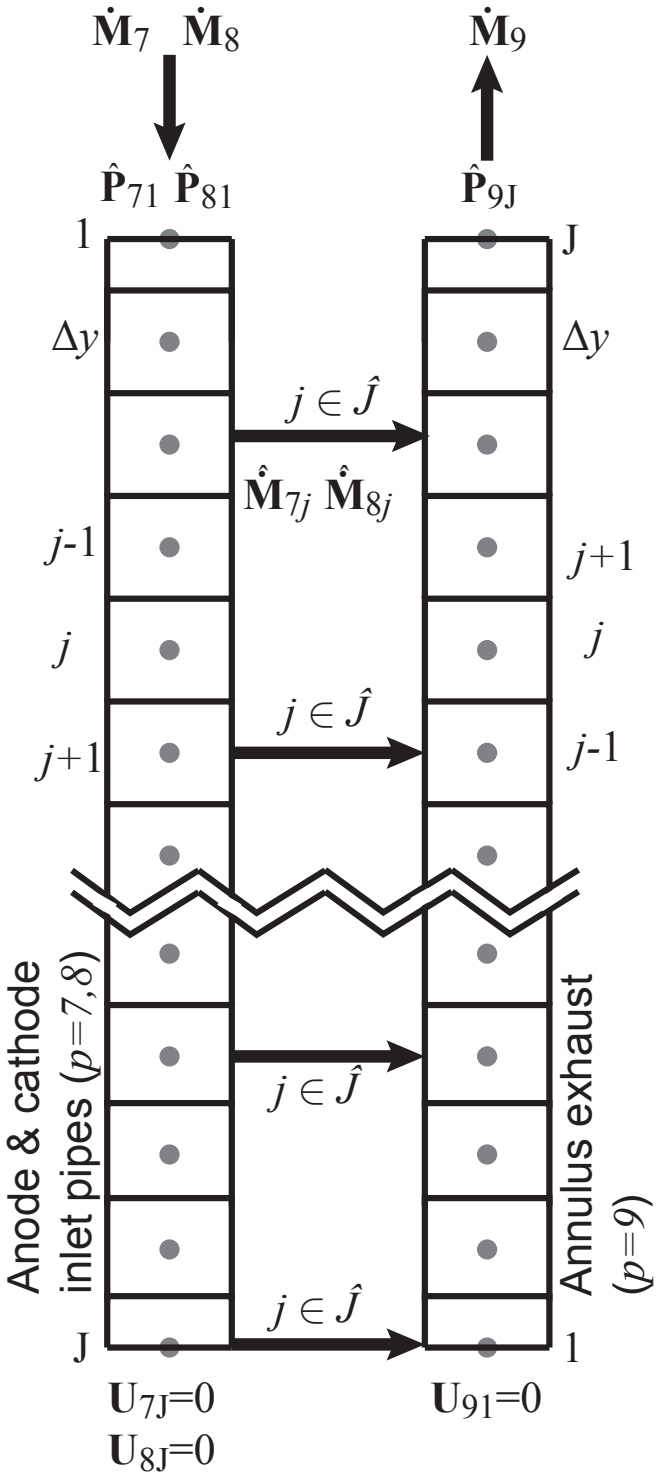

Figure 5.2: Finite-difference discretization stencil for the GFC anode, cathode and annulus pipe sections and the boundary conditions applied in the model.

the mass flow rate of fluid leaving the pipe is equal to zero as there is no stack anode or cathode inlet and exhaust outlet at these differential volumes.

5.3.16 Total pressure drop across the whole system constraints

The total pressure drop of fuel across the entire GFC system is calculated by Constraint (5.12a). The total fuel pressure drop is the sum of: (i) The pressure drop across the anode piping in the heat exchanger section $\mathbf{P}_4$; (ii) pressure drop due to anode pipe diameter change from the heat exchanger section to the GFC section $\bar{\mathbf{P}}_{47}$; (iii) the pressure drop across the anode piping in the GFC section ($\hat{\mathbf{P}}_{71}-\hat{\mathbf{P}}_{7\mathrm{J}}$); (iv) the pressure drop due to sudden contraction at the nozzle entrance to the stack on the anode side $\bar{\mathbf{P}}_{7,10}$; (v) the pressure drop due to sudden expansion at the nozzle entrance to the combustor on the anode side $\bar{\mathbf{P}}_{21}$; (vi) the pressure drop across the annulus exhaust piping in the GFC section ($\hat{\mathbf{P}}_{91}-\hat{\mathbf{P}}_{9\mathrm{J}}$); (vii) pressure drop due to annulus diameter change from the GFC section to the heat exchanger section $\bar{\mathbf{P}}_{96}$; and (viii) the pressure drop across the annulus exhaust piping in the heat exchanger section $\mathbf{P}_6$.

The total pressure drop of air across the entire GFC system is calculated by Constraint (5.12b). The total air pressure drop is the sum of: (i) The pressure drop across the cathode piping in the heat exchanger section $\mathbf{P}_5$; (ii) pressure drop due to cathode pipe diameter change from the heat exchanger section to the GFC section $\bar{\mathbf{P}}_{58}$; (iii) the pressure drop across the cathode piping in the GFC section ($\hat{\mathbf{P}}_{81} - \hat{\mathbf{P}}_{8\mathrm{J}}$); (iv) the pressure drop due to sudden contraction at the nozzle entrance to the stack on the cathode side $\bar{\mathbf{P}}_{811}$; (v) the pressure drop due to sudden expansion at the nozzle entrance to the combustor on the cathode side $\bar{\mathbf{P}}_{31}$; (vi) the pressure drop across the annulus exhaust piping in the GFC section ($\hat{\mathbf{P}}_{91} - \hat{\mathbf{P}}_{9\mathrm{J}}$); (vii) pressure drop due to annulus diameter change from the GFC section to the heat exchanger section $\bar{\mathbf{P}}_{96}$; and (viii) the pressure drop across the annulus exhaust piping in the heat exchanger section $\mathbf{P}_6$.

5.3.17 Non-negativity constraints

The non-negativity constraints ensure that every variable in the system is greater than or equal to zero.

5.4 Dispatch model formulation

In this section, we present the mathematical formulation of the dispatch problem. The parameters included in this formulation are in addition to those already introduced in the design problem formulation (see Section 5.3). Regular font letters represent parameters and bold font letters represent variables. Superscripts and accents distinguish between parameters and variables that utilize the same base letter, while subscripts identify elements of a set. Some parameters and variables are only defined for certain set elements listed in the definition. The units of each variable and parameter are also listed in brackets after its definition.

5.4.1 Sets

- $k \in \mathcal{K}$: set of system components (see Section 5.3.1)
- $p \in \mathcal{P}$: set of sections of piping and nozzles in the GFC system (see Section 5.3.1)
- $f \in \mathcal{F}$: set of fluid streams in the GFC system (see Section 5.3.1)
- $m \in \mathcal{M}$: set of reformed natural gas mixture components
    1. Methane - CH_4
    2. Carbon dioxide - CO_2
    3. Carbon monoxide - CO
    4. Steam - H_2O
    5. Hydrogen - H_2
    6. Nitrogen - N_2

- $i \in \mathcal{I}$: set of linear, exponential and quadratic approximation constants used to calculate GFC performance aspects throughout the model

- $t \in \mathcal{T}$: set of all time periods

  $\hat{t}_t$ = number of days in each time period $t \in \mathcal{T}$ [days]

  t^{day} = seconds per day conversion constant [s day^{-1}]

5.4.2 Capital, installation and operating cost parameters

c_k = capital cost scaling parameter for each system component $k \in \mathcal{K} \mid k = 1, ..., 7$ [\$, \$ cm^{-2}, \$ kW^{-1}]

s_k = capital cost scaling parameter for each system component $k \in \mathcal{K} \mid k = 1, ..., 5$ [kW, kg, m^2]

m_k = capital cost scaling parameter for each system component $k \in \mathcal{K} \mid k = 1, ..., 5$ [-]

c^{drill} = drilling cost per unit depth [\$ m^{-1}]

c^{NG} = unit cost of natural gas [\$ ft^{-3}]

c^{NGvol} = natural gas mass-to-volume conversion constant [ft^3 kg^{-1}]

C^{stack} = capital cost for the SOFC stacks in the system [\$]

C^{invert} = capital cost for the AC-DC inverter [\$]

C^{drill} = cost of drilling a single well [\$]

w_1, w_2 = objective function weighting constants [\$ kW^{-1}, \$]

5.4.3 Geothermic Fuel Cell (GFC) module and heat exchanger parameters

L^{GFC} = length of GFC heater section [m]

n^{stacks} = number of stacks per well [-]

d^{stack} = stack performance degradation constant [% per day]

A^{cell} = SOFC active area per cell [cm^{-2}]

5.4.4 Physical constants

π = Pi [-]

$\widetilde{R}$ = universal gas constant [J mol^{-1} K^{-1}],

T^{kelv} = degrees Celsius to Kelvin temperature conversion constant [K]

$\rho^{\text{H}_2\text{O}}$ = density of water at standard conditions [kg m^{-3}]

L^{CH_4} = lower heating value of natural gas [kJ kg^{-1}]

5.4.5 Fluid property parameters

M_m = molar mass of each component $m \in \mathcal{M}$ in the reformed natural gas mixture [kg mol^{-1}]

X_m = mole fraction of each component $m \in \mathcal{M}$ in the reformed natural gas mixture [-]

5.4.6 Geothermic Fuel Cell electrochemical and heating performance parameters

θ = cell leakage coefficient [fraction]

$\widetilde{a}_1$ = standard electrode potential approximation constant [V] or [J C^{-1}]

$\widetilde{a}_2$ = standard electrode potential approximation constant [V K^{-1}]

$\widetilde{a}_3$ = area-specific resistance pre-exponent approximation constant [Ω cm^2]

$\widetilde{a}_4$ = area-specific resistance exponent approximation constant [K^{-1}]

p_i = GFC heating performance polynomial surface approximation constants i=1,...,26 [°C, °C A^{-1}, °C A^{-2}, kW m^{-1}, kW m^{-1} A^{-1}, kW m^{-1} A^{-2}]

$\dot{Q}_t^{\text{demand}}$ = oil shale heating demand for time period $t \in \mathcal{T}$ [kW m^{-1}]

V^{oil} = total barrels of oil produced over the entire operating time horizon [BOE]

5.4.7 System pressure drop parameters

$\widetilde{a}_5$, $\widetilde{a}_6$ = friction factor approximation constants [-]

$\widetilde{a}_i$ = GFC section pressure drop approximation constants i=7,...,15 [Pa, Pa s kg^{-1}, Pa s^2 kg^{-2}]

5.4.8 Heat exchanger sizing parameters

Cp^{air} = air specific heat [kJ kg^{-1} K^{-1}]

Cp^{ref} = reformate specific heat [kJ kg^{-1} K^{-1}]

T^{air} = air pre-heat temperature change [K]

T^{ref} = reformate pre-heat temperature change [K]

T^{LMTD} = log mean temperature difference based on the pre-heat temperature changes [K]

U = heat exchanger approximate heat transfer coefficient [kW m^{-2} K^{-1}]

5.4.9 GFC dispatch decision variables

$\mathbf{I}_t$ = current drawn at time period $t \in \mathcal{T}$ [A] or [C s^{-1}]

$\mathbf{U}_t^{\text{fuel}}$ = fuel utilization at time period $t \in \mathcal{T}$ [fraction]

$\boldsymbol{\lambda}_t$ = stoics of air at time period $t \in \mathcal{T}$ [fraction]

5.4.10 GFC performance variables

$\mathcal{E}_t^{\text{elec}}$ = GFC module electrical efficiency based on chemical power in natural gas fuel at time period $t \in \mathcal{T}$ [fraction]

$\mathcal{E}_t^{\text{heat}}$ = GFC module heating efficiency based on chemical power in natural gas fuel at time period $t \in \mathcal{T}$ [fraction]

$\dot{\mathbf{P}}_t^{\text{chem,NG}}$ = chemical power in natural gas fuel at time period $t \in \mathcal{T}$ [kW]

$\dot{\mathbf{W}}_t^{\text{GFC,elec}}$ = electrical power drawn from GFC module at each time period $t \in \mathcal{T}$ [kW]

$\dot{\mathbf{Q}}_t^{\text{GFC,heat}}$ = heat flux from GFC module to the surrounding geology at time period $t \in \mathcal{T}$ [kW m^{-1}]

$\mathbf{T}_t^{\text{stack}}$ = GFC stacks operating temperature at time period $t \in \mathcal{T}$ [°C]

$\mathbf{V}_t^{\text{ocv}}$ = cell open circuit voltage at time period $t \in \mathcal{T}$ [V]

$\mathbf{E}_t^0$ = temperature dependent standard electrode potential at time period $t \in \mathcal{T}$ [V]

$\mathbf{V}_t^{\text{cell}}$ = cell voltage at time period $t \in \mathcal{T}$ [V]

$\mathbf{V}_t^{\text{stack}}$ = stack voltage at time period $t \in \mathcal{T}$ [V]

$\mathbf{X}_t^{\text{H}_2\text{O,out}}$ = mole fraction of steam in stack anode exhaust at time period $t \in \mathcal{T}$ [fraction]

$\mathbf{X}_t^{\text{H2,out}}$ = mole fraction of hydrogen in stack anode exhaust at time period $t \in \mathcal{T}$ [fraction]

$\mathbf{X}_t^{\text{O2,out}}$ = mole fraction of oxygen in stack cathode exhaust at time period $t \in \mathcal{T}$ [fraction]

5.4.11 Reactant flow rate variables

$\mathbf{A}_t^{\text{HX}}$ = heat exchanger area required to pre-heat the GFC reactants at time period $t \in \mathcal{T}$ [m^2]

$\dot{\mathbf{M}}_{ft}$ = mass flow rate of each fluid stream $f \in \mathcal{F}$ at time period $t \in \mathcal{T}$ [kg s^{-1}]

$\dot{\mathbf{N}}_{ft}$ = molar flow rate of reformate and GFC air streams $f \in \mathcal{F} \mid f = 4, 5$ at time period $t \in \mathcal{T}$ [mol s^{-1}]

$\dot{\mathbf{M}}_t^{\text{H}_2}$ = mass flow rate of hydrogen in reformate at time period $t \in \mathcal{T}$ [Kg s^{-1}]

5.4.12 Compressor electric power and pressure drop variables

$\dot{\mathbf{W}}_{kt}$ = electric power requirement for the compressor and pump components $k \in \mathcal{K} \mid k = 1, 2, 3$ at time period $t \in \mathcal{T}$ [kW]

$\dot{\mathbf{W}}_{t}^{\text{surp}}$ = surplus power required to meet the compressor electric power requirements not met by the GFC stacks at time period $t \in \mathcal{T}$ [kW]

$\mathbf{P}_{t}^{\text{fuel}}$ = total pressure drop of fuel over the length of anode piping in the heat exchanger and GFC heater sections at time period $t \in \mathcal{T}$ [Pa]

$\mathbf{P}_{t}^{\text{air}}$ = total pressure drop of air over the length of cathode piping in the heat exchanger and GFC heater sections at time period $t \in \mathcal{T}$ [Pa]

$\mathbf{P}_{t}^{\text{exh}}$ = total pressure drop of exhaust over the length of annulus in the heat exchanger and GFC heater sections at time period $t \in \mathcal{T}$ [Pa]

$\mathbf{R}_{ft}$ = Reynolds number of each fluid stream in the heat exchanger section $f \in \mathcal{F} \mid f = 4, 5, 9$ at time period $t \in \mathcal{T}$ [-]

$\mathbf{f}_{ft}$ = friction factor of each fluid stream in the heat exchanger section $f \in \mathcal{F} \mid f = 4, 5, 6$ at time period $t \in \mathcal{T}$ [-]

$\mathbf{P}_{pt}$ = pressure drop through each section of piping in the heat exchanger and GFC sections $p \in \mathcal{P} \mid p = 4, ..., 9$ at time period $t \in \mathcal{T}$ [Pa]

$\bar{\mathbf{P}}_{pp't}$ = pressure drop due to tube and nozzle diameter change from section $p \in \mathcal{P}$ to section $p' \in \mathcal{P}$ at time period $t \in \mathcal{T}$ [Pa]

5.4.13 Capital, installation and operating cost variables

$\mathbf{C}_{k}$ = total capital cost for each component $k \in \mathcal{K} \mid k = 1, ..., 5$ [$]

$\mathbf{S}_{k}$ = capital cost scaling factor for each component $k \in \mathcal{K} \mid k = 1, ..., 5$ [kW, kg s^{-1}, m^2]

$\mathbf{C}^{\text{fuel}}$ = total cost of natural gas fuel used to power a single GFC well for the entire time horizon [\$]

$\mathbf{DPB}^{\text{oil}}$ = dollar per barrel of oil equivalent value of the total volume of hydrocarbons produced [\$ bbl^{-1}]

5.4.14 Objective functions

The dispatch problem is used to optimize two different objective functions independent of each other,

Objective ($\mathcal{O}1$): minimizes the total capital, installation and system operating costs and the surplus electric power required from an outside source to meet compressor and pump electric power needs.

Objective ($\mathcal{O}2$): minimizes the total capital, installation and system operating costs and the surplus electric power required from an outside source to meet compressor and pump electric power needs, while maximizing the sum of the GFC electrical and heating efficiencies at each time period.

$$(\mathcal{O}1) \text{ minimize} \sum_{k=1}^{5} \quad \mathbf{C}_k + \mathbf{C}^{\text{fuel}} + C^{\text{stack}} + C^{\text{invert}} + C^{\text{drill}} + w_1 \cdot \sum_t \dot{\mathbf{W}}_t^{\text{surp}} \tag{5.13a}$$

$$(\mathcal{O}2) \text{ minimize} \sum_{k=1}^{5} \quad \mathbf{C}_k + \mathbf{C}^{\text{fuel}} + C^{\text{stack}} + C^{\text{invert}} + C^{\text{drill}} + w_1 \cdot \sum_t \dot{\mathbf{W}}_t^{\text{surp}} - w_2 \cdot \sum_t \left(\mathcal{E}_t^{\text{elec}} + \mathcal{E}_t^{\text{heat}}\right) \tag{5.13b}$$

5.4.15 Dispatch constraints

(**See Section 5.4.16**): Electric power demand constraints.

$$\dot{\mathbf{W}}_t^{\text{GFC,elec}} + \dot{\mathbf{W}}_t^{\text{surp}} \geq \sum_{k=1}^{3} \dot{\mathbf{W}}_{kt} \qquad \forall t \in \mathcal{T} \tag{5.14}$$

$$\dot{\mathbf{W}}_{1t} = \frac{P_o + \mathbf{P}_t^{\text{fuel}}}{\eta_1} \cdot \frac{\dot{\mathbf{M}}_{3t}}{\rho_3} \qquad \forall t \in \mathcal{T} \tag{5.15a}$$

$$\dot{\mathbf{W}}_{2t} = \frac{\bar{R} \cdot (T_o)}{M_1} \cdot \left(\frac{k_1}{k_1 - 1}\right) \cdot \left[\frac{P_o + \mathbf{P}_t^{\text{fuel}}}{P_o}\right]^{\left(\frac{k_1-1}{k_1}\right)} \cdot \frac{\dot{\mathbf{M}}_{1t}}{\eta_2} \qquad \forall t \in \mathcal{T} \tag{5.15b}$$

$$\dot{\mathbf{W}}_{3t} = \frac{\bar{R} \cdot (T_o)}{M_2} \cdot \left(\frac{k_2}{k_2 - 1}\right) \cdot \left[\frac{P_o + \mathbf{P}_t^{\text{air}}}{P_o}\right]^{\left(\frac{k_2-1}{k_2}\right)} \cdot \frac{\dot{\mathbf{M}}_{2t} + \dot{\mathbf{M}}_{5t}}{\eta_3} \qquad \forall t \in \mathcal{T} \tag{5.15c}$$

(**See Section 5.4.17**): GFC heating demand constraints.

$$\dot{\mathbf{Q}}_t^{\text{GFC,heat}} \geq \dot{Q}_t^{\text{demand}} \qquad \forall t \in \mathcal{T} \tag{5.16}$$

(**See Section 5.4.18**): Reactant mass flow rate constraints.

$$\dot{\mathbf{N}}_{5t} = \frac{n^{\text{cells}} \cdot n^{\text{stacks}} \cdot \mathbf{I}_t}{4F} \cdot \frac{\boldsymbol{\lambda}_t}{X^{\text{O}_2,\text{air}}} \qquad \forall t \in \mathcal{T} \tag{5.17a}$$

$$\dot{\mathbf{M}}_{5t} = M_2 \cdot \dot{\mathbf{N}}_{5t} \qquad \forall t \in \mathcal{T} \tag{5.17b}$$

$$\dot{\mathbf{N}}_{4t} = \frac{n^{\text{cells}} \cdot n^{\text{stacks}} \cdot \mathbf{I}_t}{2F} \cdot \frac{1}{(X_5 + X_3 + 4X_1) \cdot \mathbf{U}_t^{\text{fuel}}} \qquad \forall t \in \mathcal{T} \tag{5.17c}$$

$$\dot{\mathbf{M}}_{4t} = \sum_m (M_m \cdot X_m) \cdot \dot{\mathbf{N}}_{4t} \qquad \forall t \in \mathcal{T} \tag{5.17d}$$

$$\dot{\mathbf{M}}_f = Y_f \cdot \dot{\mathbf{M}}_4 \qquad \forall f \in \mathcal{F} \mid f = 1, 2, 3 \qquad \forall t \in \mathcal{T} \tag{5.17e}$$

$$\dot{\mathbf{M}}_{7t} = \dot{\mathbf{M}}_{4t} \qquad \forall t \in \mathcal{T} \tag{5.17f}$$

$$\dot{\mathbf{M}}_{8t} = \dot{\mathbf{M}}_{5t} \qquad \forall t \in \mathcal{T} \tag{5.17g}$$

$$\dot{\mathbf{M}}_{9t} = \dot{\mathbf{M}}_{6t} = \dot{\mathbf{M}}_{4t} + \dot{\mathbf{M}}_{5t} \qquad \forall t \in \mathcal{T} \tag{5.17h}$$

$$\dot{\mathbf{M}}_t^{\text{H}_2} = M_5 \cdot X_5 \cdot \dot{\mathbf{N}}_{4t} \qquad \forall t \in \mathcal{T} \tag{5.17i}$$

$$\dot{\mathbf{P}}_t^{\text{chem,NG}} = L^{\text{CH}_4} \cdot \dot{\mathbf{M}}_{1t} \qquad \forall t \in \mathcal{T} \tag{5.17j}$$

(**See Section 5.4.19**): Fuel cell electrochemical performance constraints.

$$\mathbf{V}_t^{\text{ocv}} = \theta \cdot \left[\mathbf{E}_t^0 - \frac{\widetilde{R} \cdot (\mathbf{T}_t^{\text{stack}} + T^{\text{kelv}})}{2F} \cdot \ln \left(\frac{\mathbf{X}_t^{\text{H2O,out}}}{\mathbf{X}_t^{\text{H2,out}} \cdot \sqrt{\mathbf{X}_t^{\text{O2,out}}}} \right) \right] \qquad \forall t \in \mathcal{T} \qquad (5.18a)$$

$$\mathbf{E}_t^0 = \widetilde{a}_1 - \widetilde{a}_2 \cdot (\mathbf{T}_t^{\text{stack}} + T^{\text{kelv}}) \qquad \forall t \in \mathcal{T} \qquad (5.18b)$$

$$\mathbf{V}_t^{\text{cell}} = \mathbf{V}_t^{\text{ocv}} - \left[\widetilde{a}_3 \exp^{-\widetilde{a}_4 \cdot (\mathbf{T}_t^{\text{stack}} + T^{\text{kelv}})} \right] \cdot \frac{\mathbf{I}_t}{A^{\text{cell}}} \qquad \forall t \in \mathcal{T} \qquad (5.18c)$$

$$\mathbf{V}_t^{\text{stack}} = n^{\text{cells}} \cdot \mathbf{V}_t^{\text{cell}} \qquad \forall t \in \mathcal{T} \qquad (5.18d)$$

$$\dot{\mathbf{W}}_t^{\text{GFC,elec}} = \frac{n^{\text{stacks}}}{1000} \cdot \left(1 - d^{\text{stack}} \cdot \sum_{t'=1}^{t} \hat{t}_{t'} \right) \cdot \left(\mathbf{V}_t^{\text{stack}} \cdot \mathbf{I}_t \right) \qquad \forall t \in \mathcal{T} \qquad (5.18e)$$

$$\mathcal{E}_t^{\text{elec}} = \frac{\dot{\mathbf{W}}_t^{\text{GFC,elec}}}{\dot{\mathbf{P}}_t^{\text{chem,NG}}} \qquad \forall t \in \mathcal{T} \qquad (5.18f)$$

$$\mathbf{X}_t^{\text{H2,out}} = \frac{\dot{\mathbf{N}}_{4t} \cdot (X_5 + X_3) - \frac{n^{\text{cells}} \cdot n^{\text{stacks}} \cdot \mathbf{I}_t}{2F}}{\dot{\mathbf{N}}_{4t} + \frac{n^{\text{cells}} \cdot n^{\text{stacks}} \cdot \mathbf{I}_t}{4F}} \qquad \forall t \in \mathcal{T} \qquad (5.18g)$$

$$\mathbf{X}_t^{\text{H2O,out}} = \frac{\dot{\mathbf{N}}_{4t} \cdot X_4 + \frac{n^{\text{cells}} \cdot n^{\text{stacks}} \cdot \mathbf{I}_t}{2F}}{\dot{\mathbf{N}}_{4t} + \frac{n^{\text{cells}} \cdot n^{\text{stacks}} \cdot \mathbf{I}_t}{4F}} \qquad \forall t \in \mathcal{T} \qquad (5.18h)$$

$$\mathbf{X}_t^{\text{O2,out}} = \frac{\dot{\mathbf{N}}_{5t} \cdot X^{\text{O2air}} - \frac{n^{\text{cells}} \cdot n^{\text{stacks}} \cdot \mathbf{I}_t}{4F}}{\dot{\mathbf{N}}_{5t} - \frac{n^{\text{cells}} \cdot n^{\text{stacks}} \cdot \mathbf{I}_t}{4F}} \qquad \forall t \in \mathcal{T} \qquad (5.18i)$$

(**See Section 5.4.20**): Geothermic Fuel Cell heating performance constraints.

$$\begin{aligned} \mathbf{T}_t^{\text{stack}} &= p_1 + p_2 \cdot \boldsymbol{\lambda}_t + p_3 \cdot \mathbf{I}_t + p_4 \cdot \boldsymbol{\lambda}_t^2 + p_5 \cdot \boldsymbol{\lambda}_t \cdot \mathbf{I}_t \\ &\quad + p_6 \cdot \mathbf{I}_t^2 + p_7 \cdot \mathbf{I}_t \cdot \boldsymbol{\lambda}_t^2 + p_8 \cdot \boldsymbol{\lambda}_t \cdot \mathbf{I}_t^2 + p_9 \cdot \boldsymbol{\lambda}_t^3 \qquad \forall t \in \mathcal{T} \qquad (5.19a) \\ \dot{\mathbf{Q}}_t^{\text{GFC,heat}} &= p_{17} + p_{18} \cdot \boldsymbol{\lambda}_t + p_{19} \cdot \mathbf{I}_t + p_{20} \cdot \boldsymbol{\lambda}_t^2 + p_{21} \cdot \boldsymbol{\lambda}_t \cdot \mathbf{I}_t \\ &\quad + p_{26} \cdot \mathbf{I}_t^2 \qquad \forall t \in \mathcal{T} \qquad (5.19b) \\ \dot{\mathbf{Q}}_t^{\text{GFC,heat}} &= p_{10} + p_{11} \cdot \mathbf{U}_t^{\text{fuel}} + p_{12} \cdot \mathbf{I}_t + p_{13} \cdot (\mathbf{U}_t^{\text{fuel}})^2 + p_{14} \cdot \mathbf{U}_t^{\text{fuel}} \cdot \mathbf{I}_t \\ &\quad + p_{15} \cdot \mathbf{I}_t^2 + p_{16} \cdot \mathbf{I}_t \cdot (\mathbf{U}_t^{\text{fuel}})^2 \qquad \forall t \in \mathcal{T} \qquad (5.19c) \\ \mathcal{E}_t^{\text{heat}} &= \frac{L^{\text{GFC}} \cdot \dot{\mathbf{Q}}_t^{\text{GFC,heat}}}{\dot{\mathbf{P}}_t^{\text{chem,NG}}} \qquad \forall t \in \mathcal{T} \qquad (5.19d) \end{aligned}$$

(**See Section 5.4.21**): Heat exchanger sizing constraints.

$$\mathbf{A}_t^{\text{HX}} = \frac{(Cp^{\text{air}} \cdot T^{\text{air}} \cdot \dot{\mathbf{M}}_{5t} + Cp^{\text{ref}} \cdot T^{\text{ref}} \cdot \dot{\mathbf{M}}_{4t})}{U \cdot T^{\text{LMTD}}} \qquad \forall t \in \mathcal{T} \qquad (5.20)$$

(**See Section 5.4.22**): Pressure drop across the heat exchanger section constraints.

$$\mathbf{P}_{pt} = \frac{\mathbf{f}_{ft}}{2} \cdot \frac{l^{\mathrm{HX}}}{d_p \cdot \rho_f} \cdot \left(\frac{\dot{\mathbf{M}}_{ft}}{\frac{\pi}{4}(d_p)^2} \right)^2 \qquad \forall f \in \mathcal{F} \mid f = 4,5,6 \qquad \forall p \in \mathcal{P} \mid p = f \qquad \forall t \in \mathcal{T} \tag{5.21a}$$

$$\mathbf{f}_{ft} = a_1 \cdot (\mathbf{R}_{ft})^{-a_2} \qquad \forall f \in \mathcal{F} \mid f = 4,5,6 \qquad \forall p \in \mathcal{P} \mid p = f \qquad \forall t \in \mathcal{T} \tag{5.21b}$$

$$\mathbf{R}_{ft} = \frac{4}{\pi \cdot \mu_f} \cdot \frac{\dot{\mathbf{M}}_{ft}}{d_p} \qquad \forall f \in \mathcal{F} \mid f = 4,5,6 \qquad \forall p \in \mathcal{P} \mid p = f \qquad \forall t \in \mathcal{T} \tag{5.21c}$$

(**See Section 5.4.23**): GFC section and total system pressure drop constraints.

Annulus exhaust stream pressure drop:

$$\bar{\mathbf{P}}_{96t} = \frac{0.5}{\rho_6} \cdot \left(1 - \left[\frac{d_6}{d_9} \right]^2 \right)^2 \cdot \left(\frac{\dot{\mathbf{M}}_{6t}}{\frac{\pi}{4}(d_6)^2} \right)^2 \qquad \forall t \in \mathcal{T} \tag{5.22a}$$

$$\mathbf{P}_{9t} = \widetilde{a}_7 + \widetilde{a}_8 \cdot \dot{\mathbf{M}}_{6t} + \widetilde{a}_9 \cdot (\dot{\mathbf{M}}_{6t})^2 \qquad \forall t \in \mathcal{T} \tag{5.22b}$$

$$\mathbf{P}_t^{\mathrm{exh}} = \mathbf{P}_{6t} + \bar{\mathbf{P}}_{96t} + \mathbf{P}_{9t} \qquad \forall t \in \mathcal{T} \tag{5.22c}$$

Reformed fuel stream pressure drop:

$$\bar{\mathbf{P}}_{47t} = \frac{0.21}{\rho_7} \cdot \left(1 - \left[\frac{d_7}{d_4} \right]^2 \right) \cdot \left(\frac{\dot{\mathbf{M}}_{4t}}{\frac{\pi}{4}(d_7)^2} \right)^2 \qquad \forall t \in \mathcal{T} \tag{5.23a}$$

$$\mathbf{P}_{7t} = \widetilde{a}_{10} + \widetilde{a}_{11} \cdot \dot{\mathbf{M}}_{4t} + \widetilde{a}_{12} \cdot (\dot{\mathbf{M}}_{4t})^2 \qquad \forall t \in \mathcal{T} \tag{5.23b}$$

$$\mathbf{P}_t^{\mathrm{fuel}} = \mathbf{P}_{4t} + \bar{\mathbf{P}}_{47t} + \mathbf{P}_{7t} + \bar{\mathbf{P}}_{71t} + \mathbf{P}_t^{\mathrm{exh}} \qquad \forall t \in \mathcal{T} \tag{5.23c}$$

$$\bar{\mathbf{P}}_{71t} = \frac{0.21}{\rho_7} \cdot \left(1 - \left[\frac{d_{10}}{d_7} \right]^2 \right) \cdot \left(\frac{\dot{\mathbf{M}}_{4t}}{n^{\mathrm{stacks}} \cdot \frac{\pi}{4}(d_{10})^2} \right)^2 + \frac{0.5}{\rho_7} \cdot \left(1 - \left[\frac{d_2}{d_1} \right]^2 \right)^2 \cdot \left(\frac{\dot{\mathbf{M}}_{4t}}{n^{\mathrm{stacks}} \cdot \frac{\pi}{4}(d_2)^2} \right)^2 \qquad \forall t \in \mathcal{T} \tag{5.23d}$$

GFC air pressure drop:

$$\bar{\mathbf{P}}_{58t} = \frac{0.21}{\rho_8} \cdot \left(1 - \left[\frac{d_8}{d_5}\right]^2\right) \cdot \left(\frac{\dot{\mathbf{M}}_{5t}}{\frac{\pi}{4}(d_8)^2}\right)^2 \qquad \forall t \in \mathcal{T} \tag{5.24a}$$

$$\mathbf{P}_{8t} = \widetilde{a}_{13} + \widetilde{a}_{14} \cdot \dot{\mathbf{M}}_{5t} + \widetilde{a}_{15} \cdot (\dot{\mathbf{M}}_{5t})^2 \qquad \forall t \in \mathcal{T} \tag{5.24b}$$

$$\mathbf{P}^{\text{air}}_t = \mathbf{P}_{5t} + \bar{\mathbf{P}}_{58t} + \mathbf{P}_{8t} + \bar{\mathbf{P}}_{81t} + \mathbf{P}^{\text{exh}}_t \qquad \forall t \in \mathcal{T} \tag{5.24c}$$

$$\bar{\mathbf{P}}_{81t} = \frac{0.21}{\rho_8} \cdot \left(1 - \left[\frac{d_{11}}{d_8}\right]^2\right) \cdot \left(\frac{\dot{\mathbf{M}}_{5t}}{n^{\text{stacks}} \cdot \frac{\pi}{4}(d_{11})^2}\right)^2 + \frac{0.5}{\rho_8} \cdot \left(1 - \left[\frac{d_3}{d_1}\right]^2\right)^2 \cdot \left(\frac{\dot{\mathbf{M}}_{5t}}{n^{\text{stacks}} \cdot \frac{\pi}{4}(d_3)^2}\right)^2 \qquad \forall t \in \mathcal{T} \tag{5.24d}$$

(**See Section 5.4.24**): Capital, installation and operating cost constraints.

$$\mathbf{C}_k = c_k \cdot \left(\frac{\mathbf{S}_k}{s_k}\right)^{m_k} \qquad \forall k \in \mathcal{K} \mid k = 1, ..., 5 \tag{5.25a}$$

$$\mathbf{S}_k \geq \dot{\mathbf{W}}_{kt} \qquad \forall t \in \mathcal{T} \qquad \forall k \in \mathcal{K} \mid k = 1, 2, 3 \tag{5.25b}$$

$$\mathbf{S}_4 \geq \dot{\mathbf{M}}^{\text{H}_2}_t \qquad \forall t \in \mathcal{T} \tag{5.25c}$$

$$\mathbf{S}_5 \geq \mathbf{A}^{\text{HX}}_t \qquad \forall t \in \mathcal{T} \tag{5.25d}$$

$$C^{\text{stack}} = c_6 \cdot n^{\text{stacks}} \cdot n^{\text{cells}} \cdot A^{\text{cell}} \tag{5.25e}$$

$$C^{\text{invert}} = c_7 \cdot n^{\text{stacks}} \cdot \dot{P}^{\text{GFC}} \tag{5.25f}$$

$$C^{\text{drill}} = c^{\text{drill}} \cdot (L^{\text{GFC}} + l^{\text{HX}}) \tag{5.25g}$$

$$\mathbf{C}^{\text{fuel}} = c^{\text{NG}} \cdot c^{\text{NGvol}} \cdot \sum_t \left(t^{\text{day}} \cdot \hat{t}_t \cdot \dot{\mathbf{M}}_{1t}\right) \tag{5.25h}$$

$$\mathbf{DPB}^{\text{oil}} = \frac{\sum_{k=1}^{5} \mathbf{C}_k + \mathbf{C}^{\text{fuel}} + C^{\text{stack}} + C^{\text{invert}} + C^{\text{drill}}}{V^{\text{oil}}} \tag{5.25i}$$

(**See Section 5.4.25**): Non-negativity constraints.

$\mathbf{I}_t,\ \mathbf{U}^{\text{fuel}}_t,\ \boldsymbol{\lambda}_t,\ \mathcal{E}^{\text{elec}}_t,\ \mathcal{E}^{\text{heat}}_t,\ \dot{\mathbf{P}}^{\text{chem,NG}}_t,\ \dot{\mathbf{W}}^{\text{GFC,elec}}_t,\ \dot{\mathbf{W}}^{\text{surp}}_t,\ \dot{\mathbf{Q}}^{\text{GFC,heat}}_t,\ \mathbf{T}^{\text{stack}}_t \geq 0 \ \ \forall t \in \mathcal{T}$

$\mathbf{V}^{\text{ocv}}_t,\ \mathbf{E}^0_t,\ \mathbf{V}^{\text{cell}}_t,\ \mathbf{V}^{\text{stack}}_t,\ \mathbf{X}^{\text{H}_2\text{O,out}}_t,\ \mathbf{X}^{\text{H2,out}}_t,\ \mathbf{X}^{\text{O2,out}}_t,\ \mathbf{A}^{\text{HX}}_t \geq 0 \ \ \forall t \in \mathcal{T}$

$\mathbf{P}^{\text{fuel}}_t,\ \mathbf{P}^{\text{air}}_t,\ \mathbf{P}^{\text{exh}}_t,\ \mathbf{P}_{pt},\ \bar{\mathbf{P}}_{pp't} \geq 0 \ \ \forall p \in \mathcal{P},\ \forall t \in \mathcal{T}$

$\dot{\mathbf{M}}_{ft},\ \dot{\mathbf{N}}_{ft},\ \dot{\mathbf{M}}^{\text{H}_2}_t,\ \mathbf{R}_{ft},\ \mathbf{f}_{ft} \geq 0 \ \ \forall f \in \mathcal{F},\ \forall t \in \mathcal{T}$

$\mathbf{C}_k,\ \mathbf{S}_k,\ \dot{\mathbf{W}}_{kt} \geq 0 \ \ \forall k \in \mathcal{K},\ \forall t \in \mathcal{T}$

$\mathbf{C}^{\text{fuel}},\ \mathbf{DPB}^{\text{oil}} \geq 0$

5.4.16 Electric power demand constraints

The electric power demand Constraints (5.14)-(5.15c) are the same as the previously described Constraints (5.2)-(5.3c), respectively in Section 5.3.11. The electric power demand constraints in this section have been generalized for each time period.

5.4.17 GFC heating demand constraints

Constraint (5.16) ensures that the heat flux required by the geology $\dot{Q}_t^{\text{demand}}$ for the kerogen pyrolysis process is met by the heat flux from the GFC module to the surrounding geology $\dot{\mathbf{Q}}_t^{\text{GFC,heat}}$ at each time period.

5.4.18 Reactant mass flow rate constraints

The reactant mass flow rate Constraints (5.17a)-(5.17h) are the same as the previously described Constraints (5.4b)-(5.4g), respectively in Section 5.3.12. The reactant mass flow rate constraints in this section have been generalized for each time period. The mass flow rate of hydrogen in the reformate stream $\dot{\mathbf{M}}_t^{\text{H}_2}$ calculated in Constraint (5.17i), is the product of the molar flow rate, mole fraction and molar mass of hydrogen at each time period. Constraint (5.17j) accounts for the chemical energy $\dot{\mathbf{P}}_t^{\text{chem,NG}}$ in the natural gas used to fuel the system.

5.4.19 Fuel cell electrochemical performance constraints

Constraints (5.18a)-(5.18f) establish the voltage and electric power from the GFC at each time period $t \in \mathcal{T}$ as a function of the SOFC stack operating current and temperature. Constraint (5.18a) determines the open circuit voltage $\mathbf{V}_t^{\text{ocv}}$ at each time period. An empirical leakage coefficient θ is used to account for the deviation of the open-circuit voltage from the Nernst potential as in Bove et al. [88] and Lisbona et al. [29]. The Nernst potential is a function of the stack temperature $\mathbf{T}_t^{\text{stack}}$, the universal gas constant $\widetilde{R}$, Faraday's constant F, mole fractions of steam $\mathbf{X}_t^{\text{H}_2\text{O,out}}$, hydrogen $\mathbf{X}_t^{\text{H}_2\text{,out}}$ and oxygen $\mathbf{X}_t^{\text{O}_2\text{,out}}$ in the stack exhaust streams. The standard electrode potential $\mathbf{E}_t^0$ calculated in Constraint (5.18b) is a function

of the stack temperature. The cell voltage $\mathbf{V}_t^{\text{cell}}$ is determined by the open circuit voltage less the product of current and a temperature-dependent, area-specific resistance (ASR) factor

$$\text{ASR} = \widetilde{a}_3 \exp^{-\widetilde{a}_4 \cdot (\mathbf{T}_t^{\text{stack}} + T^{\text{kelv}})}$$

defined in Constraint (5.18c). The stack voltage $\mathbf{V}_t^{\text{stack}}$ is extrapolated from the performance of a single unit-cell (see Constraint (5.18d)). Constraint (5.18e) calculates the GFC electric power $\dot{\mathbf{W}}_t^{\text{GFC,elec}}$ as the product of the number of stacks per well, the stack voltage, operating current and a loss factor d^{stack} associated with stack performance degradation with time. The GFC electrical efficiency $\mathcal{E}_t^{\text{elec}}$ is the ratio of the electric power produced to the chemical energy $\dot{\mathbf{P}}_t^{\text{chem,NG}}$ in the natural gas used to fuel the system (see Constraint (5.18f)). Constraints (5.18g)-(5.18i) calculate the values for the mole fractions of hydrogen and steam at the anode outlet and the mole fraction of oxygen at the cathode outlet by adding or subtracting the respective moles of the mixture components utilized in the electrochemical conversion process. See Anyenya et al. for a more detailed description of the SOFC electrochemical performance model [79].

5.4.20 Geothermic Fuel Cell heating performance constraints

Constraints (5.19a)-(5.19d) address the GFC heating performance as a function of current $\mathbf{I}_t$, fuel utilization $\mathbf{U}_t^{\text{fuel}}$ and stoics of air $\boldsymbol{\lambda}_t$ at each time period. A comprehensive heat transfer model used to predict the heat loss from the hot GFC components to the cooler surroundings at steady-state operating conditions is presented in Anyenya et al. [79]. The amount of cathode air flow rate is used to moderate the temperature of the stack in conventional SOFC system operations. As such, Constraint (5.19a) determines the stack temperature $\mathbf{T}_t^{\text{stack}}$ as a function of current and stoics of air at each time period, using a third-order polynomial surface fit to data obtained from the model in [79]. Similarly, Constraints (5.19b) and (5.19c) approximate the heat flux from the GFC to the surrounding geology $\dot{\mathbf{Q}}_t^{\text{GFC,heat}}$ as a function of current, fuel utilization and stoics of air at each time period. The approximation applies a third-order polynomial surface fit to data obtained from

the model in [79]. The GFC heating efficiency $\mathcal{E}_t^{\text{heat}}$ is the ratio of heat loss from the GFC to the chemical energy $\dot{\mathbf{P}}_t^{\text{chem,NG}}$ in the natural gas used to fuel the system (see Constraint (5.19d)).

5.4.21 Heat exchanger sizing constraints

Constraint (5.20) addresses the heat exchanger area required to appropriately size the counter-flow heat exchanger needed to pre-heat the reformed fuel and air flowing into the SOFC stacks [119]. The heat exchanger area is determined by: (i) The thermal energy required to heat the cold air and fuel reactants, which is the product of the fluid mass flow rates ($\dot{\mathbf{M}}_{5t}$, $\dot{\mathbf{M}}_{4t}$), temperature changes (T^{air}, T^{ref}) and specific heat capacities (Cp^{air}, Cp^{ref}); (ii) the reciprocal of the log mean temperature difference between the hot GFC exhaust gases and the cold fuel and air reactant fluids (T^{LMTD}) [93]; and (iii) the reciprocal of an approximate heat transfer coefficient for a gas-to-gas counter-flow heat exchanger (U).

5.4.22 Pressure drop across the heat exchanger section constraints

The pressure drop across the heat exchanger section, Constraints (5.21a)-(5.21c), are the same as the previously described Constraints (5.5a)-(5.5c), respectively in Section 5.3.13. The electric power demand constraints in this section have been generalized for each time period.

5.4.23 GFC section and total system pressure drop constraints

Constraints (5.22a), (5.23a) and (5.24a) calculate the pressure drop due to annulus diameter change from the GFC section to the heat exchanger section $\bar{\mathbf{P}}_{96t}$, the pressure drop due to anode pipe diameter change from the heat exchanger section to the GFC section $\bar{\mathbf{P}}_{47t}$ and the pressure drop due to cathode pipe diameter change from the heat exchanger section to the GFC section $\bar{\mathbf{P}}_{58t}$, respectively, at each time period. These constraints are similar to those described in Section 5.3.14 and have been generalized for each time period. Constraints (5.22b),(5.23b) and (5.24b) account for the pressure drop across the annulus exhaust

$\mathbf{P}_{9t}$, anode $\mathbf{P}_{7t}$ and cathode $\mathbf{P}_{8t}$ piping in the GFC section at each time period. These flow rate-dependent pressure drops are calculated by quadratic functions obtained from the numerical solutions to the differential analysis outlined in Section 5.3.15. Constraints (5.22c), (5.23c) and (5.24c) are similar to the total system pressure drop constraints described in Section 5.3.16 and have been generalized for each time period. Constraint (5.23d) calculates the sum of the pressure drop due to sudden contraction at the nozzle entrance to the stack on the anode side and the pressure drop due to sudden expansion at the nozzle entrance to the combustor on the anode side. Constraint (5.24d) calculates the sum of the pressure drop due to sudden contraction at the nozzle entrance to the stack on the cathode side and the pressure drop due to sudden expansion at the nozzle entrance to the combustor on the cathode side. These constraints are similar to those described in Section 5.3.14 and have been generalized for each time period.

5.4.24 Capital and operating cost constraints:

Constraints (5.25a)-(5.25i) address the capital, installation and operating costs of the GFC system and all its components. Constraint (5.25a) evaluates the capital and installation costs of components $k \in \mathcal{K} \mid k = 1, ..., 5$, on the basis of different scaling variables $\mathbf{S}_k$ as seen in literature [27, 87, 101, 116, 120]. For the compressor and pump components, the capital cost is evaluated on the basis of the maximum electric power required, as in Constraint (5.25b). Constraint (5.25c) calculates the cost of the natural gas fuel reformer, based on the the maximum flow rate of hydrogen gas in the reformate. The counter-flow heat exchanger depends on the maximum heat exchanger area required, as in Constraint (5.25d). Constraint (5.25e) relates the cost of the SOFC stacks to the active area of a single cell. The DC electric power from the stacks is converted to usable AC power by an inverter, whose cost depends on the electric power produced by the stacks (see Constraint (5.25f)). The drilling cost estimated in Constraint (5.25g) is dependent on the total depth of a single well and a unit depth cost parameter from Fullenbaum et al. [121]. The fuel cost is evaluated on the basis of the total volume of natural gas used over the entire system operating time horizon, as in

Constraint (5.25h). Constraint (5.25i) estimates the cost per barrel of oil and gas produced by a single GFC heater well as the ratio of the total system costs to the total volume of oil and gas produced (in barrels of oil equivalent).

5.4.25 Non-negativity constraints

The non-negativity constraints ensure that every variable in the system is greater than or equal to zero.

5.5 Model characteristics and solution strategies

The design and dispatch models presented in Sections 5.3 and 5.4 are continuous, non-convex and nonlinear in nature. As reported in Table 5.1, the large number of variables and constraints in the design problem is a result of the set of differential volumes in the GFC pressure-drop calculations (see Section 5.3.15). Specifically, for the design model instances computed in this work, each pipe section is divided into 500 differential volumes (i.e., $j \in \mathcal{J} \ni |\mathcal{J}| = 500$). Similarly, the dispatch problem contains variables and constraints for each time period. The dispatch model is solved over a 2,200-day time horizon, segmented into 115 time periods (i.e., $t \in \mathcal{T} \ni |\mathcal{T}| = 115$).

Table 5.1: Size and problem characteristics for the design and dispatch problems.

Problem characteristics	Design problem	Dispatch problem
Number of variables	5529	6384
Number of constraints	3689	7032
Linear equalities	1584	2423
Non-linear equalities	2104	3804
Linear inequalities	1	805

The following strategies are applied in an effort to reduce solution times for the convex non-linear optimization models:

1. All the variables are bounded above and below.

2. An initial feasible solution is supplied to the solver. The solution is obtained by aggregating each consecutive group of twenty time periods into a single time period and changing the data accordingly thereby reducing the size and solution time of the model.

3. A "Sliding Time Window Heuristic" is applied to reduce the number of time periods solved at each iteration [122]. The heuristic recursively defines, solves and partially fixes an approximating model. For instance, the dispatch model is solved for time periods 1-10, then the variables in time periods 1-5 are fixed and the model is solved for time period 6-15 to obtain solutions for time period 6-10, etcetera.

5.6 Case study results and discussion

The GFC design and dispatch problems are solved using KNITRO 10.2.0 on a Dell Power Edge R430 server with a 1TB hard drive, two Intel Xeon processors and 32GB of RAM. KNITRO employs four state-of-the-art interior-point and active-set methods to find locally optimal solutions to large-scale, continuous, nonlinear optimization problems [123]. The Interior/Direct algorithm used for the GFC design and dispatch optimization applies interior-point methods whereby the nonlinear problem is replaced by a series of barrier subproblems which are solved iteratively using direct linear algebra [124]. Due to the non-convex nature of the GFC optimization model, KNITRO does not guarantee that the locally feasible optimal solution it converges to, is globally optimal. In this study, we employ KNITRO's multi-start feature that restarts the problem at different initial points in an effort to find the local optimum with the best objective-function value.

5.6.1 GFC design problem results

Table 5.2 presents the main GFC system parameters applied in the design problem case study. For each heater well, the first 250 m [8] is assumed to be the overburden section ($^{\mathrm{HX}}$). The GFC stack design parameters (l^{mod}, n^{cells}) and nominal operation parameters ($\dot{P}^{\mathrm{GFC}}$, $\bar{I}$, U^{fuel} , U^{air}) are obtained from Delphi Powertrain Inc., the GFC manufacturer. The values

for the piping diameters have been increased in size from the current GFC design to reduce the pressure drop due to frictional losses and consequently the compressor electric power demands. Solving the design problem yields an optimal GFC heater length of 80 m, which is comprised of 131 stacks. This design ensures that the 196.5 kW of electric power from the SOFC stacks is enough to provide electric power required by the compressors to pressurize the fuel and air reactant stream to 1.2 MPa and 0.7 MPa, respectively.

Table 5.2: Geothermic Fuel Cell system parameters applied in the design problem case study.

Parameter	Value	Units
$\dot{P}^{\text{GFC}}$	1.5	[kW]
l^{HX}, l^{mod}	250, 1.83	[m]
n^{cells}	30	[-]
$\bar{I}$	60	[A]
U^{fuel} , U^{air}	0.63, 0.33	[-]
d_1, d_2, d_3	0.076, 0.0066, 0.0019	[m]
d_4,d_5,d_6	0.0762, 0.102, 0.127	[m]
d_7,d_8,d_9	0.0254, 0.0381, 0.0762	[m]
d_{10}, d_{11}	0.0016, 0.0033	[m]
Y_1, Y_2, Y_3	0.13, 0.68, 0.19	[-]
X^{H_2}, X^{CO}, X^{CH_4}	0.30, 0.099, 0.0022	[-]
η_1, η_2, η_3	0.85, 0.8, 0.8	[-]

5.6.2 GFC dispatch problem results

Table 5.3 presents the main GFC system design and cost parameters applied in the dispatch problems ($\mathcal{O}1$) and ($\mathcal{O}2$). The GFC heater length (L^{GFC}) and number of stacks per well (n^{stacks}) are calculated by the GFC design problem $\mathcal{D}$. The scaling parameters for the component cost equations (c_k, s_k, m_k $\forall k \in \mathcal{K} \mid k = 1, ..., 5$), drilling and fuel costs are taken from the literature [27, 87, 101, 116, 120, 121]. The molar composition of the reformed natural gas (X_m) is assumed constant.

Figure 5.3a shows dispatch results for GFC heat flux to the geology as a function of time. The heating demand data has been included in the figure for comparison. The objective function that only considered the system cost ($\mathcal{O}1$) results in an operating strategy that meets the heating demands exactly until day 1,800 when it slightly deviates due to system

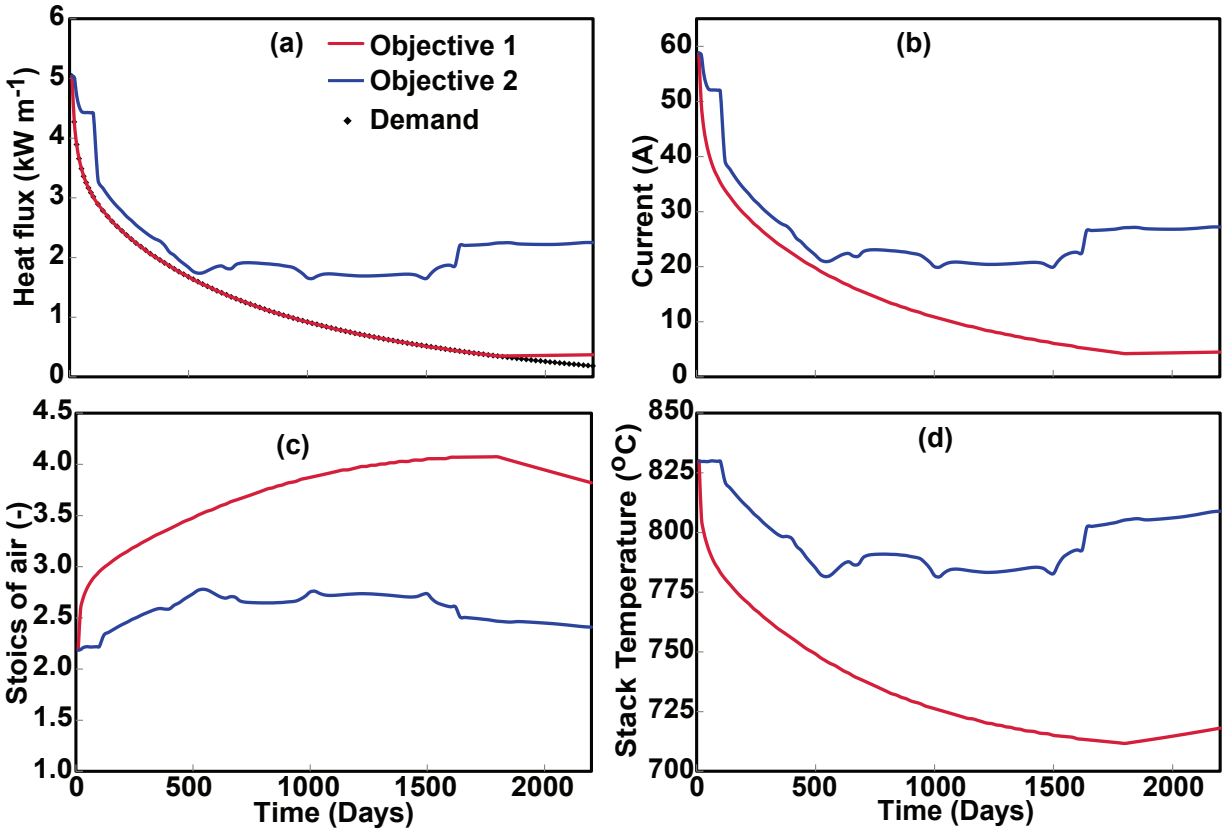

Figure 5.3: The time variation of dispatch decision variables for each objective function; (a) GFC heat flux to the geology; (b) SOFC operating current; (c) Stoics of air; (d) SOFC stack operating temperature.

Table 5.3: Geothermic Fuel Cell system design and cost parameters applied in the dispatch problem case study.

Parameter	Value	Units
L^{GFC}	80	[m]
n^{stacks}	131	[-]
d^{stack}	0.012	[% per day]
A^{cell}	106	[cm^{-2}]
c_1, c_2, c_3	8520, 91562, 91562	[$]
c_4, c_5	204, 130	[$]
s_1, s_2, s_3	100, 445, 445	[kW]
s_4	1125	[kg]
s_5	0.093	[m^2]
m_1, m_2, m_3, m_4, m_5	0.58, 0.67, 0.67, 0.7, 0.78	[-]
c_6	2300	[$ m^{-2}]
c_7	240	[$ kW^{-1}]
c^{drill}	89	[$ m^{-1}]
c^{NG}	8.15	[$ 1000ft^{-3}]
X_1, X_2, X_3	0.0022, 0.047, 0.099	[-]
X_4, X_5, X_6	0.20, 0.30, 0.35	[-]

minimum power constraints. Adding system performance terms to the objective function ($\mathcal{O}2$) results in operating strategies that ensure the GFCs are operating at high electrical and heating efficiencies. For these reasons, dispatch results for the SOFC operating current as a function of time shown in Figure 5.3b varies between 59–4 Amps for Objective ($\mathcal{O}1$), and stays above 21 Amps for Objective ($\mathcal{O}2$), to ensure maximum SOFC electrical efficiency.

Figure 5.3c shows dispatch results for stoics of air as a function of time. Stoics of air varies between 2.1–4.1 for Objective ($\mathcal{O}1$) in an effort to reduce heat flux to the geology by flowing excess cooling air at later time periods when the heating demand is greatly reduced. By contrast, a small increase in stoics of air, 2.2–2.4, is observed for Objective ($\mathcal{O}2$). This is due to the fact that higher GFC heating efficiency values are recorded when the flow rate of excess air is low. As stated in Anyenya et al. [79], SOFC stack temperature is controlled by varying the flow rate of excess cooling air. Consequently, the stoics of air values in Figure 5.3c result in the stack temperatures shown in Figure 5.3d. The high stack temperature values for Objective ($\mathcal{O}2$) due to the low cooling air flow rates over the entire time horizon may not be a sustainable operating strategy for SOFC systems, due to the accelerated stack

performance degradation at high temperatures. As such, an additional constraint on the stack temperature should be implemented in Problem ($\mathcal{O}2$).

The optimal solutions to the GFC dispatch problems using either objective function results in a net-zero surplus electric power required from an outside source to meet compressor and pump electric power needs. The stack fuel utilization factor showed a modest 7% variation over the entire 2,200-day operating time horizon for both objective functions. This means that adjusting the fuel utilization values did not have as much influence on the objective as varying the other decision variables.

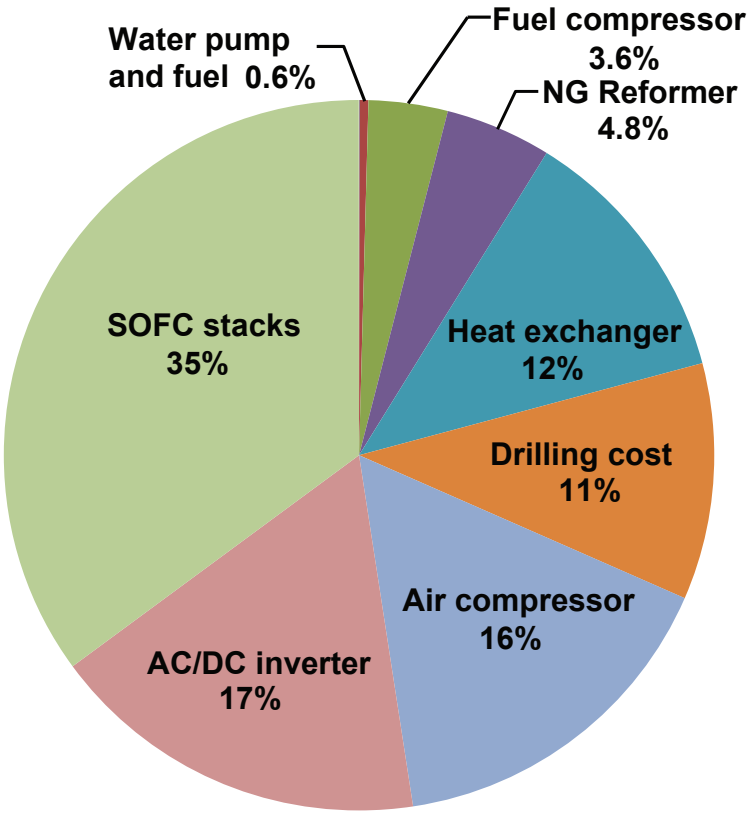

Figure 5.4: Fraction of capital, installation and operating costs associated with each component in the GFC system.

Figure 5.4 shows the fraction of capital, installation and operating costs associated with each component. The bulk of the system cost is applied towards procurement of the SOFC stacks and the AC/DC inverter while modest contributions are made by the pump, fuel

reformer and fuel compressor components. The cost of the solid-oxide fuel cells, the AC/DC inverter and drilling cost are pre-determined by the design problem as they are scaled by the length of the heater well (see Section 5.4.24). The size of the air compressor and heat exchanger are based on the maximum reactant flow rates determined by the optimal procurement strategy from the dispatch problem. As such, alternative ways to decrease the mass flow rate of air can be explored to try and reduce the air-compressor and heat-exchanger costs. A feasible option would be replacing air as the SOFC oxidant with an oxygen-enriched mixture. This would lower the oxidant mass flow rates and pressure requirements, thereby greatly reducing the size and cost of the compressor and heat exchanger units. Additionally, decreased pressure requirements would allow for an increase in the maximum GFC heater section, causing an uptake in the volume of oil shale upgraded per well. However, this approach would necessitate the addition of a cryogenic separation or pressure swing adsorption component to the GFC system to produce the oxygen-enriched mixture. A comprehensive study of the economic trade-offs resulting from this proposed change in system configuration would have to be carried out to determine whether the net change in system cost is positive or negative.

The optimum GFC system capital, installation and operating costs computed for dispatch Objectives ($\mathcal{O}1$) and ($\mathcal{O}2$) differ by 2%. The optimal well-head cost of oil and gas produced using the GFC technology of \$37/bbl is comparable to other crude oil extraction methods in Table 5.4.

Table 5.4: Comparison of the \$/bbl well-head cost of oil and gas production for different crude oil extraction methods. [References]

Technology	\$/bbl cost
Onshore Middle East	27
Canada Oil Sands	22
Volumetric Heating	43 [125]
Shell ICP	25 [126]
Steam-Assisted Gravity Drainage (SAGD)	22 [126]
Geothermic Fuel Cell	36

5.7 Conclusions

This paper presents a multi-objective design and dispatch optimization model of a solid-oxide fuel cell (SOFC) assembly for unconventional oil and gas production. The GFC well design problem optimizes the length and number of stacks in the assembly such that the volume of oil shale upgraded using a single well is maximized. The length of the GFC is constrained by the electric power required by the compressors and pump components to sufficiently pressurize the fuel and air reactants. The results of the design model case study show that:

1. The GFC reactant and exhaust piping diameters should be maximized to reduce the pressure drop across the system.

2. The variation in pressure within the reactant inlet pipes results in differences in the amount of air and fuel flow into each individual stack (14% difference between air inlet to the top and bottom stacks).

3. A 80 m long GFC heater well is ideal for SOFC stacks designed to operate at nominal fuel and air utilization factors of 63% and 33%, respectively. This optimum length value can be increased if the maximum reactant flow rates are reduced by increasing the nominal utilization factors.

The GFC dispatch model is solved for an optimal dispatch strategy that minimizes the cost of a single GFC heater well and maximizes the operating efficiency, while ensuring that the geology heating demands and the electric power demands from the auxiliary components are met. The design model case study reveals that:

1. The optimal well-head cost of $37 /bbl for the oil and gas produced using the GFC technology is comparable to conventional crude oil extraction.

2. The optimal dispatch strategy resulted in a maximum combined-heat-and-power efficiency of 79%.

3. The objective function that only considered the system cost resulted in an operating strategy that meets the heating demands exactly except at low heat flux values.

4. Adding heating and electric efficiency maximization to the objective function resulted in an operating strategy whereby the GFC supplied more heat to the geology than was required.

In addition to applying the GFC design and dispatch models to other case studies with different parameters and additional economic considerations, future efforts will also be directed towards:

1. Employing linear relaxation techniques like the McCormick relaxation on the bi-linear and tri-linear terms and the exponential transformation and piecewise linear approximation on power function terms in order to solve a linear approximation of the problem for an upper bound on the objective.

2. Using the linearized dispatch model with reduced solve times to evaluate GFC dispatch with higher time fidelities by increasing the number of time periods.

3. Implementing a feedback loop between the design and dispatch problems to iteratively solve for the optimum GFC design.

CHAPTER 6
CONCLUSIONS AND FUTURE WORK

A novel application of the combined-heat-and-power capabilities of solid-oxide fuel cells in unconventional oil and gas production is introduced. The Geothermic Fuel Cell concept offers a cost-effective and environmentally friendly alternative technology for in situ oil shale upgrading. The critical improvements to state-of-the-art oil-shale processing and SOFC-CHP technologies presented by the GFC technology include:

- The adverse environmental impacts and high costs of ex situ processing are alleviated by placing the GFC modules directly within the geology and utilizing heat from the SOFCs to upgrade the kerogen in situ;
- The high efficiency and lower CO_2-emissions of SOFC-CHP systems provide a potentially efficient and environmentally sustainable alternative to current in situ shale processing methods that rely on centrally generated power to operate buried resistive heater elements;
- Unlike most SOFC-CHP applications, the GFC application places higher value on high-grade thermal-energy generation at the expense of electricity generation;
- The GFC system is continuously operated over a four-year period, with the SOFCs held at a single steady-state condition for months at a time. In this application, there are no load-following or transient-demand constraints that necessitate dynamic-power and thermal-cycling conditions. This extends stack lifetime and consequently reduces system costs.

Geothermic Fuel Cell prototypes designed and built by Delphi Powertrain Systems (Fenton, MI, USA) were tested within a laboratory setting and operated underground within

the geology to characterize GFC operation and provide insight on the potential design improvements. The experimental data was used in the development of a steady-state system model in Aspen Plus^{TM} to predict the GFC-stacks electrochemical performance and the heat-rejection from the module. The novel contributions of this modeling work include:

- Develop the first detailed thermo-electrochemical model of a novel SOFC system architecture that is designed to reject high-temperature / high-quality process heat;
- Model and simulate the thermally integrated design as a means to characterize the stack-combustor units' performance in this application;
- Explore operating conditions that favor thermal energy output to electricity production, contrary to other SOFC-CHP applications.

Continuous, non-convex nonlinear multi-objective optimization models developed in AMPL for the design and dispatch of a single GFC heater well are solved using KNITRO 12.2.0. The optimal design and dispatch strategy yielded a well-head cost of \$37 /bbl for the oil and gas produced using the GFC technology. A maximum combined-heat-and-power-efficiency of 79% is proposed. In addition to applying the GFC design and dispatch models to other case studies with different parameters and additional economic considerations, future efforts can also be directed towards:

- Employing linear relaxation techniques such as the McCormick relaxation on the bi-linear and tri-linear terms in order to solve a linear approximation of the problem for an upper bound on the objective;
- Transforming the non-convex power functions into convex form using an exponential transformation and piecewise linear approximations to guarantee global optimality;
- Using the linearized dispatch model with reduced solve times to evaluate GFC dispatch with higher time fidelities by increasing the number of time periods;

- Implementing a feedback loop between the design and dispatch problems to iteratively solve for the optimum GFC system design and dispatch;
- Evaluating a nest of GFC heater wells and collector wells dispersed over a field, rather than a single well.

Implementation of the kerogen-pyrolysis kinetics model developed by Lee et al. [43–45] into the GFC system optimization problem would enable the evaluation of: (i) heater well spacing; (ii) heater well geometry; (iii) variations in heat flux; and (iv) duration of heater operation, on the oil and gas yield. Complementary studies regarding environmental impacts of the GFC concept to the geology, such as: (i) the impact on the water table; (ii) the consequences of geology porosity, pressure and phase changes; and (iii) how the land can be reclaimed once extraction is complete.

REFERENCES CITED

[1] Marshall T. Savage. Linearly scalable geothermic fuel cells. *US Patent and Trademark Office*, US6684948, 02 2007.

[2] Samuel J.G. Cooper, Geoffrey P. Hammond, Marcelle C. McManus, Alfonso Ramallo-Gonzlez, and John G. Rogers. Effect of operating conditions on performance of domestic heating systems with heat pumps and fuel cell micro-cogeneration. *Energy and Buildings*, 70:52–60, 2014.

[3] Siamak Farhad, Feridun Hamdullahpur, and Yeong Yoo. Performance evaluation of different configurations of biogas-fuelled SOFC micro-CHP systems for residential applications. *International Journal of Hydrogen Energy*, 35:3758–3768, 2010.

[4] Ronald C. Johnson, Tracey J. Mercier, Michael E. Brownfield, and Jesse G. Self. Assessment of in-place oil shale resources in the Eocene Green River Formation, Uinta Basin, Utah and Colorado. *U.S. Geological Survey Digital Data Series DDS-69-BB*, page 153, 2010.

[5] J.E. Birdwell, T.J. Mercier, R.C. Johnson, and M.E. Brownfield. In-place oil shale resources examined by grade in the major basins of the Green River formation, Colorado, Utah, and Wyoming. *U.S. Geological Survey Fact Sheet*, 2012–3145, 2013.

[6] John R. Dyni. Geology and resources of some world oil-shale deposits. *U.S Geological Survey Scientific Investigations Report 2005–5294*, pages 1–42, 2006.

[7] World Energy Council. World energy resources 2013 survey. *World Energy Council for Sustainable Energy*, page 468, 2013.

[8] J.E. Birdwell, T.J. Mercier, R.C. Johnson, and M.E. Brownfield. In-place oil shale resources of the Mahogany Zone, Green River formation, sorted by grade, overburden thickness, and stripping ratio, Piceance Basin, Colorado, and Uinta Basin, Utah. *U.S. Geological Survey Fact Sheet*, 2015–3005, 2015.

[9] Qingyou Li, Xiangxin, Qingqing Liu, and Xiumin Jiang. Thermal decomposition of Huadian oil shale. Part 1. Critical organic intermediates. *Fuel*, 121:109–116, 2014.

[10] A. Brandt. Converting oil shale to liquid fuels: Energy inputs and greenhouse gas emissions of the shell in situ conversion process. *Enviromental Science and Technology*, 42:7489–7495, 2008.

[11] J. Bauman, C. Huang, M. Gani, and M. Deo. *Oil Shale: A Solution to the Liquid Fuel Dilemma*, chapter 7, pages 135–146. American Chemical Society, Washington DC, USA, 2010.

[12] Melvyn C. Branch. In-situ combustion retorting of oil shale. *Progress in Energy and Combustion Science*, 5:193–206, 1979.

[13] Gregg Marland, Alfred M. Perry, and David B. Reister. Net energy analysis of in situ oil shale processing. *Energy*, 3:31–41, 1978.

[14] Alexander Bolonkin, Joseph Friedlander, Shmuel Neumann, and Strategic Solutions Technology Group. Innovative unconventional oil extraction technologies. *Fuel Processing Technology*, 124:228–242, 2014.

[15] R.L. Coates, K.E. Hatfield, and L.D. Smoot. A method of reducing CO_2 emissions from oil shale retorting. In *Proceedings of the 27th Oil Shale Symposium, Colorado School of Mines, Golden, Colorado*, pages 10–17, CO, USA, 2007. Colorado School of Mines.

[16] K. Biglarbigi, H. Mohan, P. Crawford, and M. Carolus. Economics, barriers, and risks of oil shale development in the united states. In *28th United States Association for Energy Economics/International Association for Energy Economics North America Conference*, LA, USA, 2008.

[17] M. Koel, S. Ljovin, K. Hollis, and J. Rubin. Using neoteric solvents in oil shale studies. *Pure and Applied Chemistry*, 73:153–159, 2001.

[18] R.D. Carlson, E.F. Blase, and T.R. McLendon. Development of the IIT research institute RF heating process for in situ oil shale/tar sand fuel extraction – an overview. In *Proceedings of the 14th Oil Shale Symposium, Colorado School of Mines, Golden, Colorado*, pages 04–22, CO, USA, 1981. Colorado School of Mines.

[19] Jack W. Plunkett. *Plunkett's Energy Industry Almanac 2009: The Only Comprehensive Guide to the Energy and Utilities Industry*, page 71. Plunkett Research, Ltd., Houston TX, USA, 2008.

[20] William A. Symington, David L. Olgaard, Glenn A. Otten, Tom C. Phillips, Michele M. Thomas, and Jesse D. Yeakel. ExxonMobil's electrofrac process for in situ oil shale conversion. In *Proceedings of the AAPG Annual Convention, San Antonio, USA, April 20-23 2008*, pages 04–33, TX, USA, 2008. American Association of Petroleum Geologists.

[21] L. Carrette, K. A. Friedrich, and U. Stimming. Fuel cells– fundamentals and applications. *Fuel Cells*, 1:5–39, 2001.

[22] P. W. Li and M. K. Chyu. Simulation of the chemical/electrochemical reactions and heat/mass transfer for a tubular SOFC in a stack. *Journal of Power Sources*, 124: 487–498, 2003.

[23] Paola Costamagna, Azra Selimovic, Marco Del Borghi, and Gerry Agnew. Electrochemical model of the integrated planar solid oxide fuel cell (IP-SOFC). *Chemical Engineering Journal*, 102:61–69, 2004.

[24] Yuzhang Wang, Fumihiko Yoshiba, Takao Watanabe, and Shilie Weng. Numerical analysis of electrochemical characteristics and heat/species transport in planar porous-electrode-supported SOFC. *Journal of Power Sources*, 170:101–110, 2007.

[25] N.P. Brandon P. Aguiar, C.S. Adjiman. Anode–supported intermediate temperature direct internal reforming solid oxide fuel cell. I: Model-based steady-state performance. *Journal of Power Sources*, 138:120–136, 2004.

[26] R. J. Kee, A. M. Colclasure, and H. Zhu. Fuel Cells – Solid Oxide Fuel Cells – cells and stacks. *Encyclopedia of Electrochemical Power Sources*, 3:51–62, 2009.

[27] A. A. Trendewicz and R. J. Braun. Techno-economic analysis of solid oxide fuel cell-based combined heat and power systems for biogas utilization at wastewater treatment facilities. *Journal of Power Sources*, 233:380–393, 2013.

[28] E. Fontell, T. Kivisaari, N. Christiansen, J.-B. Hansen, and J. Palsson. Conceptual study of a 250 kW planar SOFC system for CHP application. *Journal of Power Sources*, 131:49–56, 2004.

[29] Pilar Lisbona, Alessandro Corradetti, Roberto Bove, and Piero Lunghi. Analysis of a solid oxide fuel cell system for combined heat and power applications under non-nominal conditions. *Electrochimica Acta*, 53:1920–1930, 2007.

[30] S. Voss, O. Posdziech, J. Valldorf, and D. Trimis. Preliminary operational results of a domestic SOFC based micro-CHP system. *International Journal of Energy for a Clean Environment*, 12(1):1 – 13, 2013.

[31] Ghasem Arab, Hossein Ghadamian, and Saeed Abbasi. Thermo-economic modeling of an atmospheric SOFC/CHP cycle: An exergy based approach. *Mechanics and Industry*, 15(2):113 – 121, 2014.

[32] S. Velumani, C.E. Guzman, R. Peniche, and R. Vega. Proposal of a hybrid CHP system: SOFC/microturbine/absorption chiller. *International Journal of Energy Research*, 34 (12):1088 – 95, 2010.

[33] E.J. Naimaster and A.K. Sleiti. Potential of SOFC CHP systems for energy-efficient commercial buildings. *Energy and Buildings*, 61:153 – 160, 2013.

[34] Wenyuan Yang, Yingru Zhao, V. Liso, and N. Brandon. Optimal design and operation of a syngas–fuelled SOFC micro–CHP system for residential applications in different climate zones in China. *Energy and Buildings*, 80:613 – 622, 2014.

[35] L. Barelli, G. Bidini, F. Gallorini, and P.A. Ottaviano. Design optimization of a SOFC-based CHP system through dynamic analysis. *International Journal of Hydrogen Energy*, 38(1):354 – 69, 2013.

[36] C. Boigues-Munoz, G. Santori, S. McPhail, and F. Polonara. Thermochemical model and experimental validation of a tubular SOFC cell comprised in a 1 kW_{el} stack designed for CHP applications. *International Journal of Hydrogen Energy*, 39(36):21714 – 23, 2014.

[37] S. Wongchanapai, H. Iwai, M. Saito, and H. Yoshida. Performance evaluation of a direct-biogas solid oxide fuel cell-micro gas turbine (SOFC-MGT) hybrid combined heat and power (CHP) system. *Journal of Power Sources*, 223:9–17, 2013.

[38] S.E. Veyo, L.A. Shockling, J.T. Dederer, J.E. Gillett, and W.L. Lundberg. Tubular solid oxide fuel cell/gas turbine hybrid cycle power systems: Status. *Journal of Engineering for Gas Turbines and Power*, 124:845–849, 2002.

[39] M.L. Ferrari, M. Pascenti, R. Bertone, and L. Magistri. Hybrid simulation facility based on commercial 100 kWe micro gas turbine. *Journal of Fuel Cell Science and Technology*, 6:031008–1–031008–8, 2009.

[40] J. Kupecki and K. Badyda. SOFC-based micro-CHP system as an example of efficient power generation unit. *Archives of Thermodynamics*, 32(3):33–43, 2011.

[41] A.V. Akkaya, B. Sahin, and H.H. Erdem. An analysis of SOFC/GT CHP system based on exergetic performance criteria. *International Journal of Hydrogen Energy*, 33(10): 2566 – 77, 2008.

[42] L. Fryda, K.D. Panopoulos, and E. Kakaras. Integrated CHP with autothermal biomass gasification and SOFC-MGT. *Energy Conversion and Management*, 49(2):281 – 90, 2008.

[43] Kyung Jae Lee, George J Moridis, Christine A Ehlig-Economides, et al. A comprehensive simulation model of kerogen pyrolysis for the in-situ upgrading of oil shales. *SPE Journal*, 2016.

[44] Kyung Jae Lee, George J Moridis, and Christine A Ehlig-Economides. In situ upgrading of oil shale by steamfrac in multistage transverse fractured horizontal well system. *Energy Sources, Part A: Recovery, Utilization, and Environmental Effects*, 38 (20):3034–3041, 2016.

[45] Kyung Jae Lee, George J Moridis, and Christine A Ehlig-Economides. Compositional simulation of hydrocarbon recovery from oil shale reservoirs with diverse initial saturations of fluid phases by various thermal processes. *Energy Exploration & Exploitation*, page 0144598716684307, 2016.

[46] Kyung Jae Lee, George J Moridis, and Christine A Ehlig-Economides. Numerical simulation of diverse thermal in situ upgrading processes for the hydrocarbon production from kerogen in oil shale reservoirs. *Energy Exploration & Exploitation*, page 0144598716689354, 2016.

[47] Gladys Anyenya, Buddy Haun, Mark Daubenspeck, Robert Braun, and Neal P Sullivan. Experimental testing of a novel kilowatt-scale multistack solid-oxide fuel cell assembly for combined heat and power. *Journal of Electrochemical Energy Conversion and Storage*, 13(4), 2016.

[48] B. Fischer, K. Haltiner, and C. Badura. Heater and method of operating. *US Patent and Trademark Office*, US20150064592A1, 2015.

[49] K. Haltiner, B. Fischer, and C. Badura. Heater. *US Patent and Trademark Office*, US20150064593A1, 2015.

[50] J. Schneider, K. Haltiner, B. Fischer, and C. Badura. Heater and supporting structure thereof. *US Patent and Trademark Office*, US20150064594A1, 2015.

[51] B. Fischer and J. Richards. Method of operating a heater. *US Patent and Trademark Office*, US20150140461A1, 2015.

[52] B. Fischer and J. Richards. Heater with a fuel cell stack assembly and a combustor and method of operating. *US Patent and Trademark Office*, US20150140463A1, 2015.

[53] G. Ricci-Ottati, B. Fischer, T. Silvis, and K. Weess. Heater and method of operating. *US Patent and Trademark Office*, US20150162637A1, 2015.

[54] B. Fischer, J. Richards, and A. Venkiteswaran. Heater and method of operating. *US Patent and Trademark Office*, US20150204172A1, 2015.

[55] B. Fischer and J. Richards. Heater with a fuel cell stack assembly and a combustor and method of operating. *US Patent and Trademark Office*, US20150280257A1, 2015.

[56] B. Fischer, C. Badura, G. Ricci-Ottati, and J. Richards. Geothermic heater system. *US Patent and Trademark Office*, US20150292298A1, 2015.

[57] K. Haltiner. Heater and method of operating. *World Intellectual Property Organization*, WO2015030777A1, 2015.

[58] B. Fischer and K. Haltiner. Heater and method of operating. *US Patent and Trademark Office*, US20150060061A1, 2015.

[59] K. Haltiner and M. Wirth. Heater and method of operating. *US Patent and Trademark Office*, US20150064591A1, 2015.

[60] Neal Sullivan, Gladys Anyenya, Buddy Haun, Mark Daubenspeck, Joseph Bonadies, Rick Kerr, Bernhard Fischer, Adam Wright, Gerald Jones, Robert Li, et al. In-ground operation of geothermic fuel cells for unconventional oil and gas recovery. *Journal of Power Sources*, 302:402–409, 2016.

[61] S. Mukerjee, K. Haltiner, R. Kerr, J. Kim, and V. Sprenkle. Latest update on delphi's solid oxide fuel cell stack for transportation and stationary applications. *Solid Oxide Fuel Cells XII: Electrochemical Society Transactions*, 35(1):139–146, 2011.

[62] S. Mukerjee, K. Haltiner, D. Klotzbach, J. Vordonis, A. Iyer, and R. Kerr. Solid oxide fuel cell stack for transportation and stationary applications. *Solid Oxide Fuel Cells XI: Electrochemical Society Transactions*, 25(2):59–63, 2009.

[63] Christian Junaedi, Saurabh A. Vilekar, Dennis Walsh, Richard Mastanduno, Curtis Morgan, and Subir Roychoudhury. Development of integrated reformer systems for syngas production. *International Journal of Hydrogen Energy*, 37:10435–10443, 2012.

[64] Tae Won Song, Jeong Lak Sohn, Jae Hwan Kim, Tong Seop Kim, Sung Tack Ro, and Kenjiro Suzuki. Performance analysis of a tubular solid oxide fuel cell/micro gas turbine hybrid power system based on a quasi-two dimensional model. *Journal of Power Sources*, 142:30–42, 2005.

[65] S.H. Chan, H.K. Ho, and Y. Tian. Modelling of simple hybrid solid oxide fuel cell and gas turbine power plant. *Journal of Power Sources*, 109:111–120, 2002.

[66] Jens Palsson, Azra Selimovic, and Lars Sjunnesson. Combined solid oxide fuel cell and gas turbine systems for efficient power and heat generation. *Journal of Power Sources*, 86:442–448, 2000.

[67] S.H. Chan, H.K. Ho, and Y. Tian. Multi-level modeling of SOFC–gas turbine hybrid system. *Journal of Power Sources*, 28:889–900, 2003.

[68] A.O Omosun, A Bauen, N.P Brandon, C.S Adjiman, and D Hart. Modelling system efficiencies and costs of two biomass-fuelled SOFC systems. *Journal of Power Sources*, 131:96–106, 2004.

[69] K. Nanaeda, F. Mueller, J. Brouwer, and S. Samuelsen. Dynamic modeling and evaluation of solid oxide fuel cell – combined heat and power system operating strategies. *Journal of Power Sources*, 195:3176–3185, 2010.

[70] K. Lee, G. j. Moridis, and C. A. Ehlig-Economides. A comprehensive simulation model of kerogen pyrolysis for in-situ upgrading of oil shales. *SPE Journal*, 2016.

[71] S. Ahmed and M. Krumpelt. Hydrogen from hydrocarbon fuels for fuel cells. *International Journal of Hydrogen Energy*, 26:291–301, 2001.

[72] A. Heinzel, B. Vogel, and P. H*ü*bner. Reforming of natural gas-hydrogen generation for small scale stationary fuel cell systems. *Journal of Power Sources*, 105:202–207, 2002.

[73] Ralph-Uwe Dietrich, Jana Oelze, Andreas Lindermeir, Christian Spitta, Michael Steffen, Torben Kuster, Shaofei Chen, Christian Schlitzberger, and Reinhard Leithner. Efficiency gain of solid oxide fuel cell systems by using anode offgas recycle - results for a small scale propane driven unit. *Journal of Power Sources*, 196:7152–7160, 2011.

[74] Junxi Jia, Qiang Li, Ming Luo, Liming Wei, and Abuliti Abudula. Effects of gas recycle on performance of solid oxide fuel cell power systems. *Energy*, 36:1068–1075, 2011.

[75] Stefanie Wahl, Ana Gallet Segarra, Peter Horstmann, Maxime Carre, Wolfgang G. Bessler, Francois Lapicque, and K. Andreas Friedrich. Modeling of a thermally integrated 10 kW_e planar solid oxide fuel cell system with anode offgas recycling and internal reforming by discretization in flow direction. *Journal of Power Sources*, 279: 656–666, 2015.

[76] Roland Peters, Robert Deja, Ludger Blum, Jari Pennanen, Jari Kiviaho, and Tuomas Hakala. Analysis of solid oxide fuel cell system concepts with anode recycling. *International Journal of Hydrogen Energy*, 38:16809–6820, 2013.

[77] Liso Vincenzo, Nielsen Mads Pagh, and Kær Søren Knudsen. Ejector design and performance evaluation for recirculation of anode gas in a micro combined heat and power systems based on solid oxide fuel cell. *Applied Thermal Engineering*, 54:26–34, 2013.

[78] J.F. Branco, C.T. Pinho, and R.A. Figueiredo. A dimensionless analysis of radial heat conduction with variable external convection boundary conditions. *International Communications in Heat and Mass Transfer*, 28:489–497, 2001.

[79] Gladys Anyenya, Neal Sullivan, and Robert Braun. Modeling and simulation of a novel 4.5 KW_e multi-stack solid-oxide fuel cell prototype assembly for combined heat and power. *Energy Conversion and Management*, 140:247–259, 2017.

[80] Paul E. Dodds, Iain Staffell, Adam D. Hawkes, Francis Li, Philipp Grunewald, Will McDowall, and Paul Ekins. Hydrogen and fuel cell technologies for heating: A review. *International Journal of Hydrogen Energy*, 40:2065–2083, 2015.

[81] Theo Elmer, Mark Worall, Shenyi Wu, and Saffa B. Riffat. Fuel cell technology for domestic built environment applications: State of-the-art review. *Renewable and Sustainable Energy Reviews*, 42:913–931, 2015.

[82] Arata Nakajo, Fabian Mueller, Jacob Brouwer, Jan Van-herle, and Daniel Favrat. Mechanical reliability and durability of SOFC stacks. Part II: Modelling of mechanical failures during ageing and cycling. *International Journal of Hydrogen Energy*, 37: 9269–9286, 2012.

[83] H. Mulchandani and A. Brandt. Oil shale as an energy resource in a CO_2 constrained world: The concept of electricity production with in situ carbon capture. *Energy and Fuels*, 25:1633–1641, 2011.

[84] Cutler J. Cleveland and Peter A. O'Connor. Energy return on investment (EROI) of oil shale. *Sustainability*, 3:2307–2322, 2011.

[85] R.T. Leah, N.P. Brandon, and P. Aguiar. Modelling of cells, stacks and systems based around metal-supported planar IT-SOFC cells with CGO electrolytes operating at 500600 °C. *Journal of Power Sources*, 145:336–352, 2005.

[86] K. Keegan, M. Khaleel, L. Chick, K. Recknagle, S. Simner, and J. Deibler. Analysis of a planar solid oxide fuel cell based automotive auxiliary power unit. Technical Report 2002-01-0413, 01 2002.

[87] W. L. Becker, R.J. Braun, M. Penev, and M. Melaina. Design and techno-economic performance analysis of a 1 MW solid oxide fuel cell polygeneration system for combined production of heat, hydrogen, and power. *Journal of Power Sources*, 200:34–44, 2012.

[88] R. Bove and S. Ubertini. Modeling solid oxide fuel cell operation: Approaches, techniques and results. *Journal of Power Sources*, 159:543–559, 2006.

[89] L.A. Chick, R.E. Williford, J.W. Stevenson, Jr C.F. Windisch, and S.P. Simner. Experimentally-calibrated, spreadsheet-based sofc unit-cell performance model. *2002 Fuel Cell Seminar*, pages 383–386, 2002.

[90] Mogens Mogensen and Peter Vang Hendriksen. *High Temperature Solid Oxide Fuel Cells: Fundamentals, Design and Applications*, chapter 10, pages 262–286. Elsevier B.V., 2003.

[91] G. Nellis and S. Klein. *Heat Transfer*, chapter 10, pages 1056–1058. Cambridge University Press, New York NY, USA, 2009.

[92] K. Lai, B. Koeppel, K. Choi, K. Recknagle, X. Sun, L. Chick, V. Korolev, and M. Khaleel. A quasi-two-dimensional electrochemistry modeling tool for planar solid oxide fuel cell stacks. *Journal of Power Sources*, 196:3204–3222, 2011.

[93] T. Bergman, A. Lavine, F. Incropera, and D. Dewitt. *Fundamentals of Heat and Mass Transfer*, chapter 8, pages 554–555. John Wiley & Sons, Hoboken NJ, USA, 2011.

[94] R. Braun and K. Kattke. Evaluation of SOFC-based power generator concepts for application in unmanned undersea vehicles. *Journal of The Electrochemical Society*, 158:B1260–B1269, 2011.

[95] G. Greene, C. Finfrock, and T. Irvine Jr. Total hemispherical emissivity of oxidized inconel 718 in the temperature range 300-1000 °C. *Experimental Thermal and Fluid Science*, 22:145–153, 2000.

[96] T. G. Kollie, K. R. Carr, M. B. Herskovitz, J. L. Horton, and C. A. Mossman. Temperature measurement errors with Type K (Chromel vs Alumel) thermocouples due to short–ranged ordering in Chromel. *Oak Ridge National Laboratory Central Research Library*, TM, 1975.

[97] Gilles Aouizerate, Louis J. Durlofsky, and Pierre Samier. New models for heater wells in subsurface simulations, with application to in situ upgrading of oil shale. *Computational Geoscience*, 16:519–533, 2012.

[98] Babatunde A. Ogunnaike and W. Harmon Ray. *Process Dynamics, Modeling, and Control*. Oxford University Press, New York NY, USA, 1994.

[99] R. J. Braun, S. A. Klein, and D. T. Reindl. Evaluation of system configurations for solid oxide fuel cell-based micro-combined heat and power generators in residential applications. *Journal of Power Sources*, 158:1290–1305, 2006.

[100] H. Apfel, M. Rzepka, H. Tu, and U. Stimming. Thermal start–up and thermal management of SOFC's. *Journal of Power Sources*, 154:370–378, 2006.

[101] F. Calise, M. Dentice-d'Accadia, L. Vanoli, and M.R von Spakovsky. Single-level optimization of a hybrid SOFC—GT power plant. *Journal of Power Sources*, 159: 1169–1185, 2006.

[102] Hongbo Ren, Weisheng Zhou, Kenichi Nakagami, Weijun Gao, and Qiong Wu. Multi-objective optimization for the operation of distributed energy systems considering economic and environmental aspects. *Applied Energy*, 87(12):3642–3651, 2010.

[103] Hongwei Li, Razi Nalim, and P-A Haldi. Thermal-economic optimization of a distributed multi-generation energy systema case study of beijing. *Applied Thermal Engineering*, 26(7):709–719, 2006.

[104] Javier Contreras, Arturo Losi, Mario Russo, and Felix F Wu. Simulation and evaluation of optimization problem solutions in distributed energy management systems. *IEEE Transactions on Power Systems*, 17(1):57–62, 2002.

[105] SL Douvartzides, FA Coutelieris, and PE Tsiakaras. On the systematic optimization of ethanol fed sofc-based electricity generating systems in terms of energy and exergy. *Journal of Power Sources*, 114(2):203–212, 2003.

[106] Francesca Palazzi, Nordahl Autissier, François MA Marechal, and Daniel Favrat. A methodology for thermo-economic modeling and optimization of solid oxide fuel cell systems. *Applied Thermal Engineering*, 27(16):2703–2712, 2007.

[107] Ernst Riensche, Ulrich Stimming, and Guido Unverzagt. Optimization of a 200 kw sofc cogeneration power plant: Part I: Variation of process parameters. *Journal of Power Sources*, 73(2):251–256, 1998.

[108] Behzad Najafi, Ali Shirazi, Mehdi Aminyavari, Fabio Rinaldi, and Robert A Taylor. Exergetic, economic and environmental analyses and multi-objective optimization of an sofc-gas turbine hybrid cycle coupled with an msf desalination system. *Desalination*, 334(1):46–59, 2014.

[109] F Calise, M Dentice dAccadia, L Vanoli, and Michael R von Spakovsky. Full load synthesis/design optimization of a hybrid sofc–gt power plant. *Energy*, 32(4):446–458, 2007.

[110] Mark Kuchta, Alexandra Newman, and Erkan Topal. Implementing a production schedule at LKAB's Kiruna Mine. *Interfaces*, 34(2):124–134, 2004.

[111] Mohsen Sadeghi, Ata Chitsaz, S. M. S. Mahmoudi, and Marc A. Rosen. Thermoeconomic optimization using an evolutionary algorithm of a trigeneration system driven by a solid oxide fuel cell. *Energy*, 89:191–204, 2015. ISSN 0360-5442. doi: 10.1016/j.energy.2015.07.067.

[112] S. Sadeghi and M. Ameri. Multiobjective optimization of pv-bat-sofc hybrid system: Effect of different fuels used in solid oxide fuel cell. *Journal of Energy Engineering*, 140(2), 2014. ISSN 0733-9402. doi: 10.1061/(asce)ey.1943-7897.0000170.

[113] Stoian Petrescu, Camelia Petre, Monica Costea, Octavian Malancioiu, Nicolae Boriaru, Alexandru Dobrovicescu, Michel Feidt, and Charles Harman. A methodology of computation, design and optimization of solar stirling power plant using hydrogen/oxygen fuel cells. *Energy*, 35(2):729–739, 2010. ISSN 0360-5442. doi: 10.1016/j.energy.2009.10.036.

[114] Kristopher A Pruitt, Sven Leyffer, Alexandra M Newman, and Robert J Braun. A mixed-integer nonlinear program for the optimal design and dispatch of distributed generation systems. *Optimization and Engineering*, 15(1):167–197, 2014.

[115] Kristopher A Pruitt, Robert J Braun, and Alexandra M Newman. Evaluating shortfalls in mixed-integer programming approaches for the optimal design and dispatch of distributed generation systems. *Applied Energy*, 102:386–398, 2013.

[116] Sepehr Sanaye and Arash Katebi. 4E analysis and multi objective optimization of a micro gas turbine and solid oxide fuel cell hybrid combined heat and power system. *Journal of Power Sources*, 247:294–306, 2014.

[117] Frank M. White. *Fluid Mechanics*. McGraw–Hill, New York NY, USA, 2009.

[118] Claus Borgnakke and Richard E. Sonntag. *Fundamentals of Thermodynamics*. John Wiley & Sons, Hoboken NJ, USA, 2009.

[119] Masoud Rokni. Thermodynamic and thermoeconomic analysis of a system with biomass gasification, solid oxide fuel cell (SOFC) and stirling engine. *Energy*, 76: 19–31, 2014.

[120] R. F. Boehm. *Design Analysis of Thermal Systems*. John Wiley & Sons, New York NY, USA, 1987.

[121] Richard Fullenbaum, Curtis Smith, Min Rao, Jing Xiao, Stephen Adams, and Russ Fontaine. Oil and gas upstream cost study. Technical Report DT007965, 10 2015.

[122] Christopher Cullenbine, R Kevin Wood, and Alexandra Newman. A sliding time window heuristic for open pit mine block sequencing. *Optimization Letters*, 5(3):365–377, 2011.

[123] Richard H Byrd, Jorge Nocedal, and Richard A Waltz. *KNITRO: An integrated package for nonlinear optimization*, pages 35–59. Springer, 2006.

[124] Richard H Byrd, Mary E Hribar, and Jorge Nocedal. An interior point algorithm for large-scale nonlinear programming. *SIAM Journal on Optimization*, 9(4):877–900, 1999.

[125] Alan K Burnham and James R McConaghy. *Comparison of the acceptability of various oil shale processes*. United States. Department of Energy, 2006.

[126] Amjad Shah, Robert Fishwick, Joseph Wood, Gary Leeke, Sean Rigby, and Malcolm Greaves. A review of novel techniques for heavy oil and bitumen extraction and upgrading. *Energy & Environmental Science*, 3(6):700–714, 2010.